Nanoscale Spatial Inhomogeneity in Photovoltaic Devices

A Dissertation Presented

by

Ahsan Ashraf

to

The Graduate School

in Partial Fulfillment of the Requirements

for the Degree of

Doctor of Philosophy

in

Physics

Stony Brook University

May 2016

Stony Brook University

The Graduate School

Ahsan Ashraf

We, the dissertation committee for the above candidate for the Doctor of Philosophy degree, hereby recommend acceptance of this dissertation.

Matthew D. Eisaman – Dissertation Advisor
Adjunct Professor, Department of Physics and Astronomy
Assistant Professor, Department of Electrical and Computer Engineering
Physicist, Brookhaven National Laboratory

Thomas C. Weinacht – Chairperson of Defense
Professor, Department of Physics and Astronomy

Philip B. Allen
Professor, Department of Physics and Astronomy

Benjamin M. Ocko
Adjunct Professor, Department of Physics and Astronomy
Senior Scientist, Brookhaven National Laboratory

T. Venkatesh
Associate Professor
Department of Materials Science and Engineering

This dissertation is accepted by the Graduate School.

Charles Taber
Dean of the Graduate School

Abstract of the Dissertation

Nanoscale Spatial Inhomogeneity in Photovoltaic Devices

by

Ahsan Ashraf

Doctor of Philosophy

in

Physics

Stony Brook University

2016

A substantial challenge in the development of optoelectronic devices such as photovoltaics and photodetectors is the inherent non-uniformity in semi-crystalline and polycrystalline photoactive materials. The focus of this work is to understand and evaluate the impact of specific non-uniformities in organic and inorganic materials, and present strategies for the development of novel architectures where instead of being detrimental they can be beneficial to device performance.

We focus on materials in two regimes: a) materials with small dielectric constants, where the Coulomb interaction between an electron and a hole is strong therefore forming Frenkel excitons, with radii of the same order as the size of the unit cell; b) materials with larger dielectric constants, where electric field screening tends to reduce the Coulomb interaction forming Wannier excitons with radii larger than lattice spacing.

In the first regime, we focus on organic electronic materials specifically poly-(3 hexylthiophene), a conjugated semiconducting poly-

mer and electron donor, and [6,6]-phenyl-C-61-butyric acid methyl ester, an electron accepting fullerene derivative. We measure the donor-acceptor volume fraction and the interchain disorder in thin-films as the film thickness approaches the confinement limit (less than 20nm), using variable angle spectroscopic ellipsometry and near-edge X-ray absorption fine structure spectroscopy. Furthermore, we also investigate the effect of confinement on the coherence length and the crystalline microstructure of the polymer component using grazing incidence wide angle X-ray scattering. As the film thickness is decreased to the confinement regime, the films became less phase segregated and the polymer component formed less disordered (more aligned along the surface normal) and smaller crystallites.

In the second regime of materials with larger dielectric constants, we focus on understanding the recombination mechanism in polycrystalline $Cu(In_{1-x}Ga_x)Se_2$ due to material compositional inhomogeneity. We measure the charge transport behavior as a function of temperature of few-grain regions using lithographically defined electrical contacts. We correlate these measurements with energy dispersive X-ray spectroscopy and aberration corrected transmission electron microscopy with selected area electron diffraction. We find that local regions with higher fraction of copper-rich grains show enhanced interfacial recombination whereas regions with a higher fraction of copper-poor grains show standard bulk recombination behavior.

Finally, we present novel architectures where material non-uniformities localized at surfaces are used beneficially: a) we demonstrate strong ($2.11x10^{13}$ e/cm^2), robust, and spontaneous graphene n-doping on polycrystalline $Cu(In_{1-x}Ga_x)Se_2$ due to surface-transfer doping from Na atoms that diffuse to the surface from the soda-lime-glass substrate. b) we demonstrate broadband tunable antireflection using densely packed silicon nanotextures, comprising a surface layer whose optical properties differ substantially from those of the bulk, providing the key to improved performance.

Contents

List of Figures

List of Tables

List of Publications

1. **A. Ashraf**, D. M. N. M. Dissanayake, D. S. Germack, C. Weiland, and M. D. Eisaman, *Confinement-Induced Reduction in Phase Segregation and Interchain Disorder in Bulk Hetereojunction Films*, ACS Nano, 8, 323-331 (2014)
2. **A. Ashraf**, D. M. N. M. Dissanayake, M. D. Eisaman, *The effect of confinement on the crystalline microstructure of polymer:fullerene bulk heterojunctions*, Phys. Chem. Chem. Phys., The Royal Society of Chemistry, 17, 23326-23331 (2015)
3. **A. Ashraf**, D. M. N. M. Dissanayake, M. D. Eisaman, *Measuring charge carrier mobility in photovoltaic devices with micron-scale resolution*, Appl. Phys. Lett., 106, 113504 (2015)
4. **A. Ashraf**, D. M. N. M. Dissanayake, W. Zhang, D. Dwyer, K. Kisslinger, F. Wang, H. Efstathiadis, M. D. Eisaman, *Effect of single-grain composition on local recombination in* $Cu(In_{1-x}Ga_x)Se_2$ *Photovoltaics*, Phys. Rev. Lett. (in preparation) (2016)
5. **A. Ashraf**, K. O. Davis, K. Ogutman, W. V. Schoenfeld, M. D. Eisaman, *Hyperspectral laser beam induced current system for solar cell characterization*, Photovoltaic Specialist Conference (PVSC), IEEE 42nd, 1-4, (2015)
6. D. M. N. M. Dissanayake, **A. Ashraf**, D. Dwyer, K. Kisslinger, L. Zhang, Y. Pang, H. Efstathiadis and M. D. Eisaman, *Spontaneous and strong multi-layer graphene n-doping on soda-lime glass and its application in graphene-semiconductor junctions*, Scientific Reports, 6, 21070 (2016)
7. D. M. N. M. Dissanayake, **A. Ashraf**, Y. Pang, and M. D. Eisaman, *Mapping Spatially Resolved Charge Collection Probability within Bulk Heterojunction Photovoltaics*, Advanced Energy Materials, 4, 1300525 (2014)

8. D. M. N. M. Dissanayake, **A. Ashraf**, Y. Pang, and M. D. Eisaman, *Guided-mode quantum efficiency: A novel optoelectronic characterization technique*, Rev. Sci. Instrum. 83, 114704 (2012)

9. D. M. N. M. Dissanayake, **A. Ashraf**, Y. Pang, M. D. Eisaman, *Hyperspectral guided-mode quantum efficiency: A novel characterization technique for thin-film photovoltaics*, Photovoltaic Specialists Conference (PVSC), IEEE 39th, 1406-1411 (2013)

10. A. Rahman, **A. Ashraf**, H. Xin, X. Tong, P. Sutter, M. D. Eisaman and C. T. Black, *Sub-50-nm self-assembled nanotextures for enhanced broadband antireflection in silicon solar cells*, Nature Communications, 6, 5963 (2015).

11. S. Hoang, **A. Ashraf**, M. D. Eisaman, D. Nykypanchuk and C.Y. Nam, *Enhanced Photovoltaic Performance of Ultrathin Si Solar Cells via Semiconductor Nanocrystal Sensitization: Energy Transfer vs. Optical Coupling Effects*, Nanoscale, 8, 5873-5883 (2016)

Chapter 1

Introduction

1.1 Motivation and Overview

Photovoltaic energy conversion is one of the most promising renewable energy technologies in the international effort to transition from more primitive sources of energy such as fossil fuels as the backbone of the global economy. As the need for this transition becomes more urgent, due to the adverse effects of these fuels on the environment, the demand for research driving improved photovoltaic energy conversion and a fundamental understanding of the materials and mechanisms within becomes more compelling and immediate [1]. Although renewable energy refers to a whole host of energy sources including wind, biomass, and hydroelectric, it is energy directly harvested from the sun that has the greatest potential for meeting a significant fraction of the increasing demand in the imminent energy crisis [2]. According to a Basic Energy Sciences report, the technical generation potential for solar energy is $\sim$ 400,000TWh compared to wind $\sim$ 50,000TWh, geothermal $\sim$ 31,000TWh, biopower $\sim$ 500 TWh, and hydrothermal power systems $\sim$ 300TWh[3]. For context, the primary energy consumption of the world in 2013 was $\sim$150,000 TWh ($\sim$20% of which was electricity). This is expected to increase to 256,000 TWh by 2050 [4].

1.2 Photovoltaic Effect

The photovoltaic effect was first observed by Becquerel in 1839 [5] followed by the discovery of the photoconductive effect in selenium by Adams and Day in 1876 [6]. The first large area photovoltaic (PV) device was also made using selenium by Charles Fritts in 1894 [7]. The first silicon p-n junctions were not fabricated until the 1950s when significant improvements in the processing of crystalline silicon (c-Si) were made. In 1954 the first p-n junction based silicon PV devices were reported by Chapin, Fuller and Pearson with a power conversion efficiency (η) from light to electricity of 6% [8]. Research into PV devices gained momentum due to the space race in the 1960s and the world oil crisis in the 1970s with several new candidates as photoactive materials such as gallium arsenide (GaAs), indium phosphide (InP), and cadmium telluride (CdTe) [9]. The first thin film PVs, which being researched as a low cost alternative to c-Si, were fabricated in 1976 [10] using hydrogenated amorphous silicon dicovered by Chittick et al. in 1969 [11]. Due to the poor power conversion efficiency (2.4%) of these devices, new absorber materials for thin-film PVs were heavily being researched. In 1976, Kazmerski et al. reported p-$CuInSe_2$/n-CdS heterojunction solar cells with power conversion efficiencies in the range of 4-5% [12].

Driven by low cost fabrication methods, lightweight and flexible material properties, and strong light absorption in the visible region, the discovery of conductive organic materials in 1977 opened up a new direction in the field of optoelectronic devices [13, 14]. The first organic PV (OPV) devices were fabricated using merocyanine dye as the photoactive material sandwiched between two dissimilar metal electrodes [15]. The first bilayer heterojunctions were made using copper phthalocyanine (CuPc) and a perylene tetracarboxylic derivative in 1986 with a power conversion efficiency of 1% [16]. Due to the parallel development of high quality semiconducting polymers and the discovery of ultrafast charge transfer between polymers and buckminsterfullerene (C_{60}), polymers quickly became the preferred absorber materials over small molecules [17, 18]. In 1995, Yu et al. demonstrated an interpenetrated bulk heterojunction (BHJ) OPV device fabricated using a derivative of C_{60}, [6,6]-phenyl-C61 butyric acid methyl ester (PCBM), and a polymer composite [19]. Due to the increased interfacial area between the donor and acceptor materials facilitating carrier separation, the power conversion efficiency for these devices improved to 1.5%. However the BHJ devices as opposed to the standard bilayers are a more complex system and have raised several interesting questions about morphology and carrier extraction.

1.3 Aims and Outline of the thesis

In the effort towards low cost and scalable energy technologies, thin-film polycrystalline and organic PVs are playing an increasingly important role. However due to the complex morphology of BHJ OPVs and the granular structure of polycrystalline PVs, these devices are inherently non-uniform. Therefore the focus of this work is to understand and evaluate the impact of specific non-uniformities - at the nanoscale: spatial scales on the order of or less than one micron - including those due to compositional inhomogeneities and confinement/interfacial effects, and investigate novel materials and device architectures.

The fundamental properties of materials and relevant device physics will be given in Chapter 2. Chapter 3 will focus on organic photovoltaics, specifically the effect of confinement and interfacial interactions on donor acceptor segregation, and donor microstructure and disorder. In Chapter 4, local recombination mechanisms due to grain-to-grain compositional variation in $\mathrm{CuIn}_{1-x}\mathrm{Ga}_x\mathrm{Se}_2$ are investigated. Novel techniques for the measurement of mobility and doping density with micron scale resolution are introduced in Chapter 5 followed by investigation into novel device architectures and materials in Chapter 6. Chapter 7 will provide a conclusion highlighting key findings, open questions, future research directions, and application areas of the research presented in this thesis.

Chapter 2

Device Physics

2.1 Physics of Semiconductors

2.1.1 Semiconductors and Photovoltaic Principle

A material with an electrical resistivity of 10^{-2} - 10^{9} Ω-cm (unilluminated) and an energy bandgap for electronic excitations of 0.5 - 3eV is defined as a semiconductor [20]. The bandgap of a given material is defined as the difference in energy from the valence band to the conduction band in k-space. As the bandgap in semiconductors is comparable to an order of magnitude with the thermal energy at room temperature ($\sim$ 298 K), the intrinsic conductivity of semiconductors is largely governed by E_g/k_BT, where E_g is the bandgap, k_B is the Boltzmann constant, and T is the temperature. For a low concentration of intrinsic charge carriers, the electrical conductivity is low and this ratio is large, whereas for a high concentration of intrinsic charge carriers, the electrical conductivity is high and this ratios becomes small.

When a photon is absorbed by a semiconductor, an electron is excited from the valence band into the conduction band forming an exciton. This is a bound state of an electron and a hole (the lack of an electron from a full valence band) and is electrically neutral. The bound state is hydrogenic with a smaller binding energy due to the screening of the Coulomb force by other electrons in the semiconductor. The decay of this exciton occurs when the electron drops back into the valence band in a process called recombination. The binding energy of the exciton depends on the dielectric constant of the material. This is given by $E_{ex} = E_H \dfrac{m^*_{eff}}{m_0}\left(\dfrac{\epsilon_0}{\epsilon}\right)^2$ where $E_H = 13.6eV$.

For small dielectric materials, the Coulomb interaction is stronger and the exciton radius tends to be smaller. The typical binding energy of such excitons, also called Frenkel excitons, are $\sim$1 eV. In this work, this is often the case for organic semiconducting materials. For example, a material used in this work, P3HT has $\epsilon \sim 3.5\epsilon_0$ and $m^*_{eff} \sim 0.5m_0$, therefore $E_{ex} \sim 0.5eV$.

In inorganic semiconductors, the dielectric constant is generally larger therefore the Coulomb interaction is reduced. Such excitons are known as Wannier excitons and can have a radius larger than the lattice spacing. The binding energy of such excitons is smaller ∼10meV and therefore they are easy separable by thermal energy at room temperature (∼25meV). For silicon, $\epsilon = 11.7\epsilon_0$ and $m^*_{eff} = 0.1m_0$, therefore $E_{ex} \sim 10meV$.

2.1.2 Formation of a $p - n$ Junction

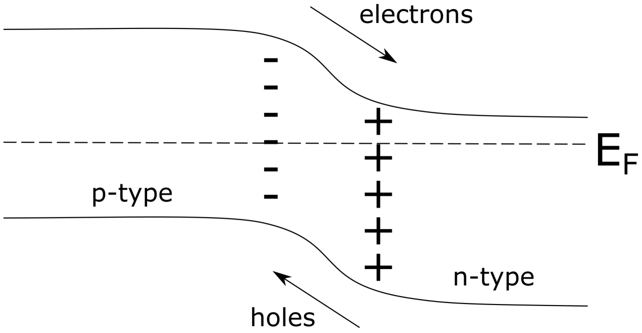

Figure 2.1: A schematic of the formation of a p-n junction.

Once the electron is excited, the generation of electricity requires the separation of the charges before they recombine and extraction to an external circuit. In order for the charges to be separated and extracted, a built-in electric field is used created by forming a p-n junction. A p-n junction is formed when p- and n-type materials are brought into intimate contact, where a p-type material has an excess of holes, and an n-type material has an excess of electrons. The large differences in electron and hole concentrations cause diffusion across the junction, resulting in the formation of a charge depletion region. An electric field is created within the depletion region which promotes the drift of minority carriers between the p- and n-type materials. When the drift current equals the diffusion current, thermal equilibrium is reached. At thermal equilibrium the Fermi level is constant across the junction, causing the energy bands to bend (Figure 2.1). The drift and diffusion current densities are given by

$$J_{diffusion} = qD_e\frac{dn}{dx} - qD_h\frac{dp}{dx} \tag{2.1}$$

$$J_{drift} = nq\mu_e\epsilon + pq\mu_h\epsilon \tag{2.2}$$

where $J_{diffusion}$ and J_{drift} are the diffusion and drift currents respectively, D_e and D_h are the diffusion coefficients for electrons and holes respectively, μ_e and μ_h are the electron and hole mobilities respectively, n and p are the electron and hole concetrations, ϵ is the applied electric field, and q is the electronic charge.

2.1.3 Equivalent Circuit Model

In order to create an equivalent circuit model, we can represent a photovoltaic device as a current source.

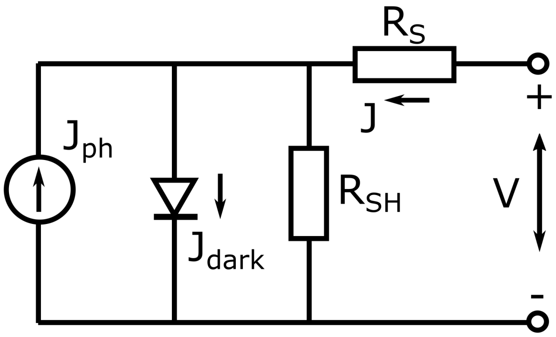

Figure 2.2: Equivalent circuit of a photovoltaic device. J$_{ph}$ is the photogenerated current, J$_{dark}$ is the leakage current, J is the load current, V is the voltage across the load, R$_S$ is the series resistance, and R$_{SH}$ is the shunt resistance.

Figure 2.2 shows an equivalent circuit model for a device. As photogenerated current flows through the external circuit, a potential difference is created generating dark current through the diode.

$$J_{dark} = J_0(e^{qV/k_BT} - 1) \tag{2.3}$$

$$J = J_{dark} - J_{ph} = J_0(e^{qV/k_BT} - 1) - J_{ph} \tag{2.4}$$

J_0 is the reverse saturation current, k_B is the Boltzmann constant, T is the temperature, and q is the electronic charge. When the net current flowing through the circuit is zero, we are at the open circuit condition which defines the open circuit voltage (V_{oc})

$$V_{oc} = \frac{k_BT}{q} ln\big(\frac{J_{ph}}{J_0} + 1\big) \tag{2.5}$$

When the $V_{oc} = 0$, we are at short circuit conditions, which defines the short circuit current (J_{sc}).

$$J_{sc} = -J_{ph} \tag{2.6}$$

This is assuming an ideal diode where the series and shunt resistances are not accounted for. In a real photovoltaic device, the effects due to the series and shunt resistances are not trivial. The series resistance (R_S) is the aggregated resistance of the active material, the interfaces between the active material and the contacts, and the contacts themselves. The shunt resistance (R_{SH}) is the resistance against the leakage current. In an ideal device, $R_S \sim 0$ and $R_{SH} \sim \inf$. In an equivalent circuit model accounting for these resistances,

$$J = J_0\big(e^{\dfrac{q(V - JR_S)}{k_BT}} - 1\big) + \big(\frac{V - JR_S}{R_{SH}}\big) - J_{ph} \tag{2.7}$$

2.1.4 Performance Metrics

Figure 2.3 shows a characteristic current-voltage curve for a photovoltaic device when in the dark (dotted) and under illumination (solid). The three main metrics used to characterize a device are the J_{sc}, the V_{oc}, and the fill factor (FF). In the fourth quadrant of the curve (between V = 0 - V_{oc}), power is delivered to the external circuit. In the optimal condition, the device operates at maximum power at J_m and V_m shown in Figure 2.3.

$$P = JV = J_0 * V(e^{qV/k_BT} - 1) - J_{ph} * V \tag{2.8}$$

The condition for maximum power is when $dP/dV = 0$. Therefore,

$$V_m = k_BT/qln\big[\frac{1 + J_{ph}/J_0}{1 + qV_m/k_BT}\big] \tag{2.9}$$

$$\approx V_{oc} - \frac{k_BT}{q}ln\big(1 + \frac{qV_m}{k_BT}\big) \tag{2.10}$$

and

$$J_m = J_0\big(\frac{qV_m}{k_BT}e^{qV_m/k_BT}\big) \tag{2.11}$$

$$\approx J_{ph}\big(1 - \frac{1}{qV_m/k_BT}\big). \tag{2.12}$$

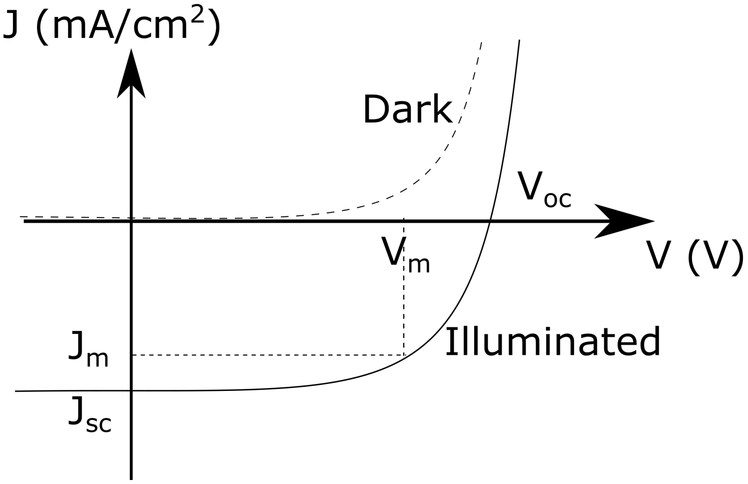

Figure 2.3: A characteristic current-voltage (JV) curve for a photovoltaic device.

The maximum power output then is

$$P_m = V_m I_m \tag{2.13}$$

$$\approx J_{ph}\big[V_{oc} - \frac{k_B T}{q} ln\big(1 + \frac{qV_m}{k_B T}\big) - \frac{k_B T}{q}\big]. \tag{2.14}$$

The ideal power conversion efficiency or η is then given by

$$\eta = \frac{P_m}{P_{in}} = \frac{FF * J_{sc} V_{oc}}{P_{in}} \tag{2.15}$$

where P_{in} is the incident power. The fill factor (FF) can then be defined as

$$FF = \frac{J_m V_m}{J_{sc} V_{oc}}. \tag{2.16}$$

In order to maximize η, we need to maximize all three parameters, J_{sc}, V_{oc}, and the FF.

2.1.5 Solar Radiation and Efficiency Limits

Solar radiation incident upon the earth is primarily in the energy range of 0.5 - 4.0eV. If we approximate the sun as a black body at T $\sim$ 5760 K, the power density incident on the earth is 1353 Wm^{-2}. Part of this radiation is absorbed

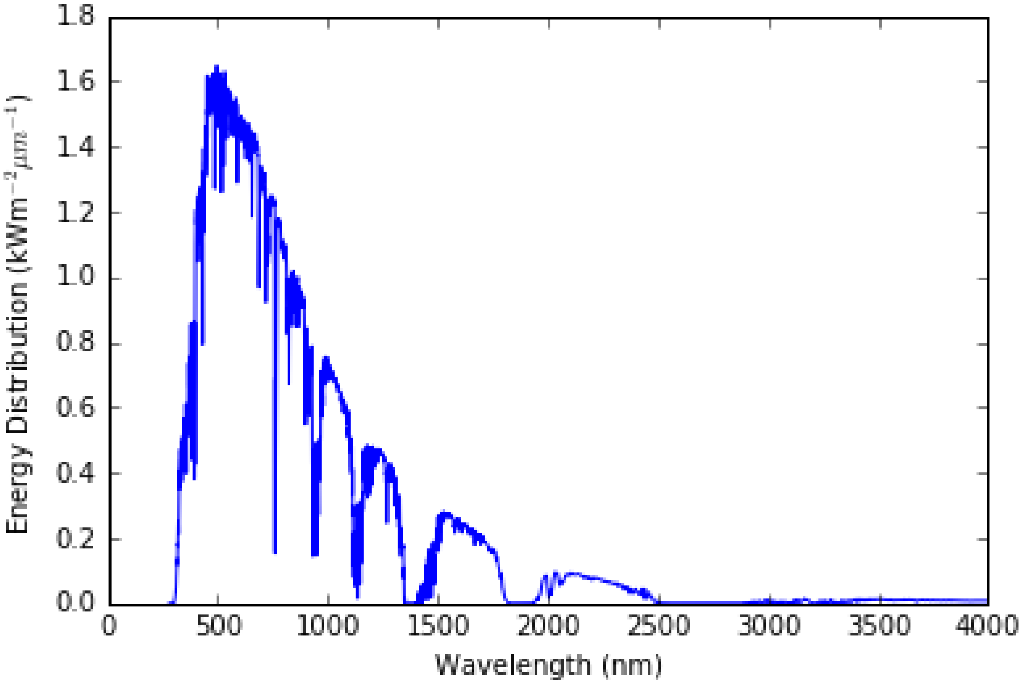

Figure 2.4: Solar radiation spectrum AM1.5.

by the atmosphere, therefore the power density on the surface of the earth is $\sim$ 1000 Wm^{-2}. The degree of attenuation depends on a parameter defined as 'air mass' or the ratio between the optical path length to the sun and the optical path length if the sun is directly above. As a standard, photovoltaic performance is specified at air mass 1.5 (AM1.5G) spectrum (shown in Figure 2.4 [21].

2.2 Organic Photovoltaics

Although the mechanical and chemical properties of polymers and small molecule organic materials have been studied extensively, their optoelectronic properties have been of increasing interest since the awarding of the Nobel prize in chemistry in 2000 to Shirakawa, Heeger, and MacDiarmid for their work on trans-polyacetylene [14].

2.2.1 Conjugated Organic Materials and Band Structure

A polymer is a macromolecule consisting of many repeating subunits. Each subunit is called a monomer. Conjugated polymers can be conductive or semiconductive due to the sp^2 hybridization of carbon atoms in the subunit. Insulating polymers, on the other hand, have a backbone of sp^3 hybridized carbon atoms in the subunit. In sp^3 hybridization, a 2s orbital and 3 2p orbitals ($2p_x$, $2p_y$, $2p_z$) combine to form 4 sp^3 orbitals (Figure 2.5a).

In sp^2 hybridization, a 2s orbital and two 2p orbitals ($2p_x$, $2p_y$) combine (or hybridize) to form 3 sp^2 orbitals. These can form three σ bonds with other atoms. However there is a remaining $2p_z$ orbital which can overlap with other subunits when in a polymer to form π bonds. The orientation of the $2p_z$ bonds overlap is perpendicular to the 3 σ bonds. When the overlap of the $2p_z$ orbitals is in-phase, we get bonding (π) and when it is out-of-phase, we get anti-bonding (π^*) molecular orbitals. The π-bonding energy level is known as the highest occupied molecular orbital (HOMO), and the π^*-bonding energy level is known as the lowest unoccupied molecular orbital (LUMO). The energy gap between the HOMO and LUMO levels is then referred to as the bandgap (E_g) in such organic materials. At sufficient conjugation of the polymer, organic semiconductors begin to behave similarly to inorganic semiconductors with a conduction and valence band.

2.2.2 Transport Mechanism

When a photon is absorbed by an organic semiconductor, an electron is excited from the HOMO to the LUMO level. The electron, and the absence of an electron in the HOMO level or the hole, are localized and can be on the same molecular chain. As mentioned earlier, this quasi-particle is known as an exciton. Although in inorganic semiconductors the excitons can be approximated by a free electron and hole (due to a large dielectric constant), organic materials generate electron-hole pairs owing to their lower dielectric constants. The wave functions of the electron and hole in an organic material are also more spatially restricted therefore the excitons are short ranged.

The transfer of excitation states between molecules is understood using Förster resonance energy transfer or a Dexter process [22]. In either case, typical distances of energy transfer are $\sim$ 10nm. Therefore the range of exciton diffusion before they must be separated into free electrons and holes is also $\sim$ 10nm. Once the exciton is dissociated, the carrier mobility becomes an important parameter. This is given by $\mu = v/E$ where v is the carrier velocity and E is the applied electric field. Mobility affects both drift and diffusion processes and

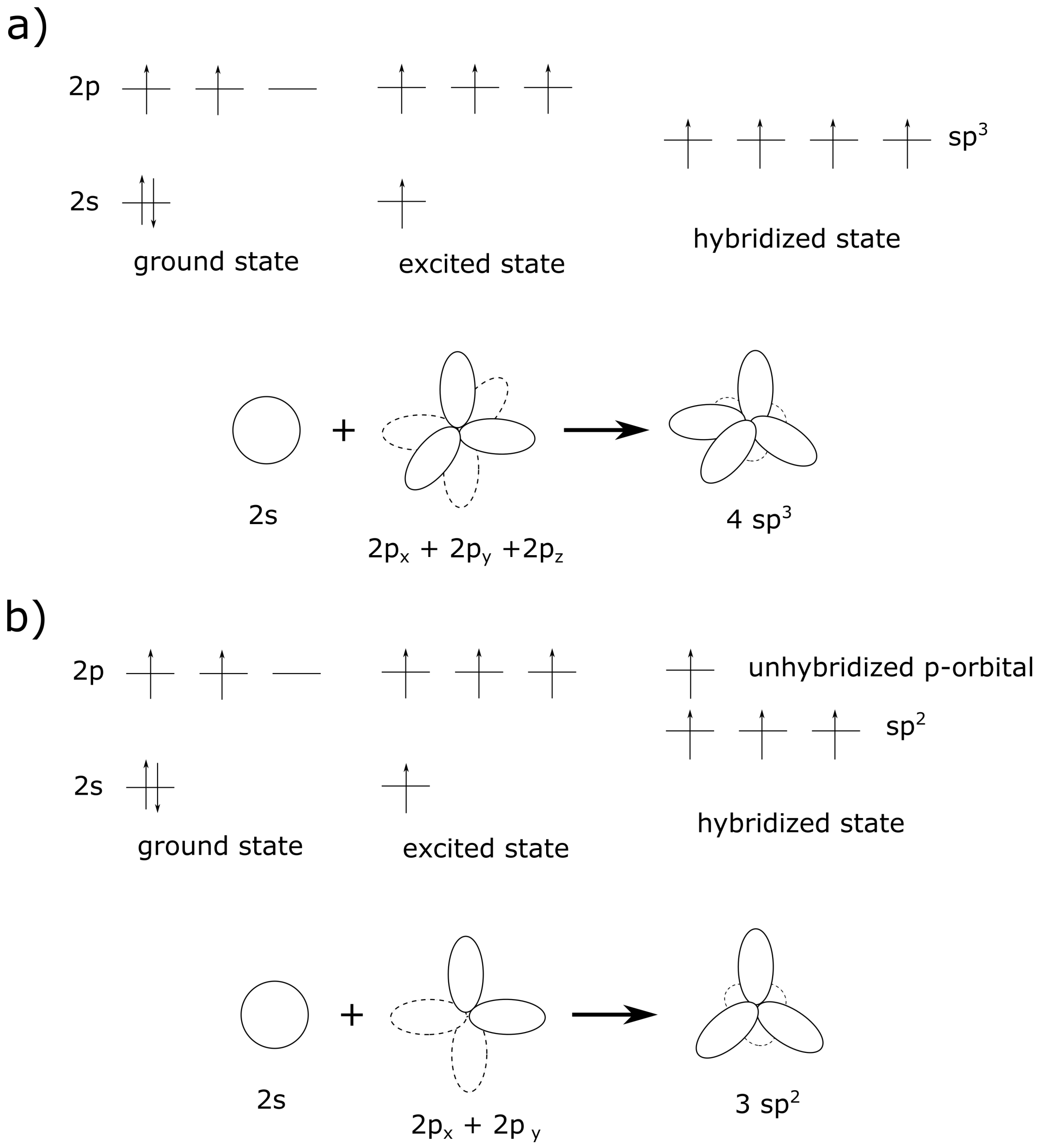

Figure 2.5: Formation of a) sp^3 and b) sp^2 hybridization.

is typically measured using Time-Of-Flight (ToF), Field Effect (FE), charge extraction by linearly increasing current (CELIV) or electroluminescence measurements.

2.2.3 Device Architecture

A basic device architecture for an organic photovoltaic (OPV) device is shown in Figure 2.6. This is a donor-acceptor type of OPV, where a donor material (a polymer) and an acceptor material (fullerene) are combined to form an active layer. First generation OPVs were single layer devices where an organic polymer was sandwiched between two metals of different work functions. In a single layer architecture (Figure 2.7), the excitons are separated at the interface between the active layer and the metal electrodes restricting the thickness of the active layer to be of the same order as the exciton dissociation length ($\sim$ 10nm). In a donor acceptor OPV, the exciton dissociation process is more efficient as it happens at the interface between the donor and acceptor materials.

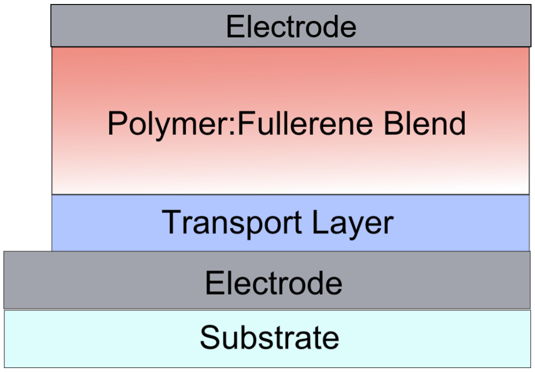

Figure 2.6: A schematic of a standard device architecture for an organic photovoltaic device.

Initially such donor acceptor devices were created as bilayer devices, which stacked the two donor and acceptor layers (Figure 2.7 middle). Although this solved the problem of tightly bound excitons being dissociated and reducing recombination, the efficiency was still limited by the exciton diffusion length. Given the absorption coefficients of these materials, at least 100nm of the material was required in order to absorb most incident light at AM1.5.

The two limiting length scales (exciton diffusion length and thickness required for light absorption), required a new architecture where the donor and acceptor materials were finely intermixed together (Figure 2.7 bottom). This maximized the interface between the donor and acceptor materials, providing ample surface area for the excitons to dissociate before recombining which allowed the films to be thicker without suffering from heavy recombination losses. This architecture is known as the bulk heterojunction (BHJ). BHJ device structure requires interpenetrating pathways of donor and acceptor ma-

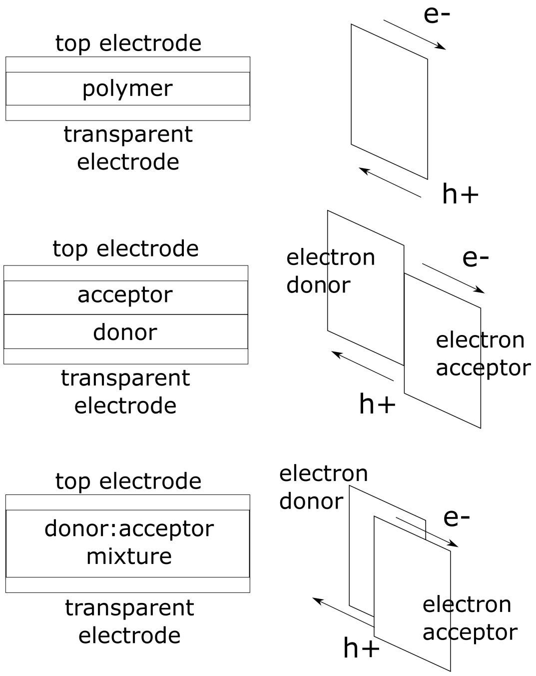

Figure 2.7: A schematic of a single-layer(top)/bilayer(middle)/bulk heterojunction(bottom) device structure and schematic energy band diagram of each device.

terials to the respective electrodes for the electrons and holes to be extracted. This causes BHJ devices to be very sensitive to processing conditions due to the morphology of the blend. The morphology is affected by surface/interface effects causing separation of the two materials. The separation of constituent materials in a thin film due to surface/interface effects is known as phase segregation. In this work, we will be focusing on a conjugated semiconducting polymer as a donor, poly-(3 hexylthiophene) - P3HT, and an electron accepting fullerene derivative [6,6]-phenyl-C-61-butyric acid methyl ester - PCBM.

Chapter 3

Understanding Inhomogeneity in Organic Photovoltaics

Key Findings:

- As the film thickness is decreased to the confinement regime, the film becomes less phase segregated
- The polymer component in the BHJ becomes less disordered or more aligned in the substrate normal direction
- The crystallite size of the polymer component in the BHJ tends to decrease as the film thickness is decreased

3.1 Experimental Techniques

3.1.1 Organic Semiconducting Layer Preparation

Poly(3-hexylthiophene) (P3HT) was obtained from Rieke Metal Inc. (4002-EE, Lot # BS21-21) with a molecular weight, M_w of 40,000 - 60,000 Daltons and regioregularity, RR of 90-94%. [6,6]-Phenyl-C-61-butyric acid methyl ester (PCBM) of purity greater than 99.5% was obtained from American Dye Source Inc. (ADS61BFA, Lot # 12E011E). The substrates used were microscope slide glass obtained from Thermo Fisher Scientific, and silicon wafers with a native silicon dioxide layer ($\sim$ 1nm) and also 300nm silicon dioxide on silicon wafers obtained from Ted Pella Inc. The substrates were cleaned by sonication for 15 minutes in acetone, then 15 minutes in isopropanol, and finally 15 minutes in deionized water. The cleaned substrates were dried using N_2 gas and further cleaned using the ultraviolet/ozone procedure for 300s. P3HT and PCBM solutions were prepared in a 1:1, 2:1, and 1:2 ratio using 1,2-dichlorobenzene (anhydrous, 99%), Sigma Aldrich, St. Louis, MO. The solutions were prepared inside a glove box (O_2 <0.1 ppm, H_2O <0.1 ppm) and stirred for >2 hours at 50°C using a Teflon coated magnetic stirrer. After stirring they were filtered through a polytetrafluoroethylene(PTFE) syringe filter with a pore size of 0.45m and transferred into a fresh vial. Solid solutions were prepared with concentrations of 2mg/ml, 5mg/ml, 10mg/ml, 20mg/ml and 50mg/ml. These were pipetted onto the substrate and spun at 700rpm for 40s inside the glove box. After the films were dry (judging by the drastic visual change in coloration of the film), they were thermally treated at 150°C for 10 minutes inside the glovebox. Additionally, pristine P3HT films from concentrations of 2mg/ml, 5mg/ml and 10mg/ml were prepared using the same process. Pure PCBM films were prepared using a 10mg/ml solution in anhydrous chloroform (Sigma Aldrich, St. Louis, MO). The PCBM films were spun at 700 rpm for 40s inside the glovebox and thermally treated on a hotplate at 150°C for 10 minutes inside the glovebox.

3.1.2 Variable Angle Spectroscopic Ellipsometry

Variable Angle Spectroscopic Ellipsometry (VASE) is an optical technique used to measure the dielectric properties or the complex refractive index of thin films. In this work, we use spectroscopic ellipsometry to measure the dielectric properties of the active layers and model the variation in volume fraction of materials within the films. By understanding the optical properties we also infer information about the crystalline order of the molecules within the material.

All measurements were made using a J.A. Woollam V.A.S.E. M-2000 based on the diode array rotating compensator ellipsometer technology. A multiple sample approach was employed where the active material (P3HT:PCBM) was spun on three different substrates using the same processing conditions,[23] including: (1) microscope slide glass, (2) silicon with a native oxide, and (3) silicon with a thermal oxide (300nm) layer. It was assumed that the optical properties of the active layers on all three substrates were identical and that any changes in the spectra were due to the substrate. This method results in multiple sets of unique data for the same system allowing for greater confidence of the fits to a parameterized model. Ellipsometric measurements were first made on the cleaned bare substrates. All data was taken in the wavelength range of 210 to 1700nm at angles of 45 to 75° in divisions of 7.5°. The built-in auto alignment function of the M-2000 was used to align the sample before the measurement. For each sample, a second measurement was taken at a different spot on the film to reduce random error. The data collected from the three substrates was analyzed simultaneously to yield solutions for the complex refractive index and the film thickness. The ellipsometric data was analyzed by simultaneously fitting identical models for the active layer on each substrate that were defined with coupled complex refractive indices of the active layers using the WVASE32 software (version 3.770, J. A. Woollam Co.). The best fit for the optical constants was found by minimizing the mean square error (MSE) between the measured and the modeled curves using the Levenberg-Marquardt multivariate regressions algorithm. The complex refractive indices from the VASE modeling were confirmed by making UV-Vis-IR transmission/reflection measurements using a Perkin Elmer Lamda 950 UV/Vis/NIR Spectrophotometer and modeling the data (using finite-difference time-domain (FDTD) method from Lumerical Solutions, Inc.) with the SE-measured complex refractive indices as input. Thickness results from ellipsometry were confirmed using stylus profilometry (Tencor Instruments, AlphaStep 200) and atomic force microscopy in tapping mode using the film scratch method [24] (AFM, Asylum Research Model MFP-3D).

SE data consists of direct measurement of the complex ratio of the reflection amplitudes of polarized light with electric field within (r_p) and perpendicular (r_s) to the plane of incidence as a function of the angle of incidence. [25, 26] From this data, plots of ψ and Δ versus angle of incidence are determined from the definition of ψ and Δ as follows.

$$r_p/r_s = tan(\psi)e^{i\Delta} \tag{3.1}$$

The angle of incidence in the measurement is varied between 45° and 75° in increments of 7.5°. This range includes the Brewster angle at which the sensitivity of the measurement is highest. The large range is used so that parameter correlation can be reduced in the fitting process and sensitivity to morphology, anisotropy and composition changes can be enhanced. The measurement was done at room temperature (~25°C) and in air.

3.1.3 Near Edge X-ray Absorption Spectroscopy (NEXAFS)

NEXAFS is a form of X-ray absorption spectroscopy where the absorption of an X-ray photon creates a core hole in a selected atomic core level which is subsequently filled by the capture of an electron from another shell and the emission of a fluorescent photon or an Auger process, and each of these processes can be measured.

NEXAFS spectroscopy was performed at the National Institute of Standards and Technology facility (beamline U7A) at the National Synchrotron Light Source (NSLS) of Brookhaven National Laboratory for soft X-ray materials characterization. Data was collected in the energy range of 270eV to 320eV around the carbon K-edge (at 285eV) in partial electron yield (PEY) mode with a grid bias of 50 V.

3.1.4 Grazing Incident Wide Angle X-ray Scattering (GIWAXS)

GIWAXS is a X-ray scattering technique which can be used for the understanding of nanostructured thin films. In this work, we use GIWAXS to understand the variation of crystalline microstructure in thin films due to confinement.
GIWAXS measurements were performed at the undulator-based X9 endstation at the National Synchrotron Light Source (NSLS), Brookhaven National Laboratory. Two-dimensional scattering images were acquired using a flat area detector, positioned 280mm from the sample, and using an X-ray wavelength of 0.918nm (photon energy of 13.5keV). Raw data conversion to q-space was accomplished by measuring a standard sample with known scattering features (Silver Behenate), and accounting for detector position and tilt angle in the grazing incidence geometry. The incident beam was collimated using slits and focused onto the sample position using a KB mirror system; the beam size at the sample position was approximately 200m horizontal width and 50μm vertical width. Measurements were performed at a variety of incident angles (0.07°, 0.10°, 0.12°, 0.15°, and 0.20°); all measurements above the critical angle (0.1° degrees for P3HT) had similar features. The results presented in this thesis representing the bulk of the film use the data at 0.20°, which is well above the critical angle for any of the films studied, and is thus representative of the entire film.

3.2 Phase Segregation and Disorder in Bulk Heterojunction Films

Phase segregation in materials is defined as the enrichment or dilution of a given material constituent at or near a surface/interface. When a mixture of materials (polymer:fullerene) is deposited on a substrate, depending on the surface energy of the substrate, an inhomogeneous distribution of the polymer:fullerene volume fraction in the direction normal to the substrate has been reported [27, 28]. This phase segregation phenomenon directly impacts the optical and electronic properties of the organic active layer critical for device applications [29].

The effects of thin-film confinement on the material properties of ultrathin polymer (electron donor):fullerene (electron acceptor) bulk heterojunction films can be important for both fundamental understanding and device applications such as thin-film photovoltaics. In this section we use variable angle spectroscopic ellipsometry and near edge X-ray absorption fine structure spectroscopy to measure the optical constants, donor-acceptor volume fraction profile, and the degree of interchain order as a function of the thickness of a poly(3-hexythiophene-2,5-diyl) and phenyl-C61-butyric acid methyl ester bulk heterojunction film. We find that as the thickness of the bulk heterojunction film is decreased from 200 nm to the thickness confinement regime (where the film thickness is on the order of a typical crystallite size $\sim$ 20nm), the vertical phase segregation gradient of the donor and acceptor phases becomes less pronounced. In addition, observing the change in exciton bandwidth and the shift of absorption resonances (0-0 and 0-1) relative to neat donor and acceptor films, we find that the conjugation length and disorder in ultrathin films (20 nm) are less affected than thicker (200 nm) films by the addition of fullerene into the polymer. We believe that these findings could be important for discovering methods of precisely controlling the properties of bulk heterojunction films with crucial implications for designing more efficient organic based photovoltaics.

3.2.1 Reduction in Phase Segregation due to Confinement

Restriction of the film thickness below the radius of gyration in macromolecules leads to thin-film confinement effects, in which a significant transition of the materials properties occurs compared to bulk films [30–33]. Even though thin-film confinement is well studied for both amorphous and crystalline pure polymers [34], its effects on the morphology and the interfacial interactions of ultrathin (<20 nm, the length scales comparable to the polymers radius of gyration)[35] polymer (electron donor):fullerene (electron acceptor) interpenetrating composites - bulk heterojunction (BHJ) films - have not been well investigated [36]. BHJs are a more complex and functionally more advanced class of composite materials and a fundamental understanding of the effect of thin-film confinement on BHJ films could be crucial for applications such as novel organic photovoltaics. In BHJ films, even within a bulk thickness regime of $\sim$ 200 nm, its morphology is reported to be affected by various processing conditions such as choice of solvent, drying time, thermal treatments [29], and the use of solvent additives [37, 38]. Furthermore, depending on the surface energy of the substrate on which such BHJs are coated, an inhomogeneous distribution of the polymer:fullerene volume fraction phase segregation - in the direction normal to the substrate has been reported [27, 28]. These morphological and interfacial phenomena directly impact the optical and electronic properties of the BHJ layer critical for device applications [29]. In particular, the high- and low-bandgap polymer regions within the bulk of the BHJ layer believed to be formed by phase segregation, are directly linked to the reduction in bimolecular recombination (relating to both an electron and a hole) of BHJ based organic photovoltaics and this is perceived to be one crucial reason for its outstanding performance among solution processed thin-film photovoltaics [39, 40]. Therefore, a thorough understanding of these properties (i.e morphology, phase-segregation) and their possible variation within the thin-film confinement regime are important for both a fundamental understanding of the material system, as well as for novel device applications. In particular, an ultrathin active layer could improve the limitation of charge collection in BHJ films which, together with improved light-trapping to compensate the concomitant loss in optical density in ultrathin regime, would boost the overall performance in organic photovoltaics. Pang et al. [41] have demonstrated a novel organic photovoltaic design where the absorption fraction of a guided mode in a 20 nm thick bulk heterojunction active layer can be equal to the absorption fraction for light that is normally incident on a standard 100 nm active layer. In addition, many other groups have recently demonstrated strong optical absorption in similarly thin photoactive layers [41–47].

In this work, we use spectroscopic ellipsometry and near edge X-ray absorption fine structure (NEXAFS) spectroscopy to measure the optical constants, vertical composition profile (donor-acceptor ratio), and morphology of poly[3-hexylthiophene-2,5-diyl] (P3HT) and [6,6]-phenyl C61 butyric acid methyl ester (PCBM) BHJ layer as a function of thickness. We find that as the thickness of the BHJ is decreased from the range of 100nm - 200nm to the ultrathin regime of <20 nm, surface-energy effects at the interfaces play an increasingly important role in determining the BHJ morphology and phase segregation [28]. In addition, as a function of BHJ thickness we measure the change of refractive index and shift of the dipole-transition resonance frequencies relative to neat donor and acceptor films to gain insight into the domain structure and degree of order in the interpenetrating donor-acceptor phases. The data is interpreted via a rigorous optical model that divides the BHJ into multiple sections in the substrate-normal direction, allowing a reconstruction of the vertical phase segregation profile (variation of P3HT/PCBM volume fraction ratio in the substrate normal direction) from spectroscopic ellipsometry (SE) data. Additionally, we validate the SE measurements by directly measuring the P3HT/PCBM ratio at the top (film-air) surface of the BHJ using NEXAFS.

Using spin-cast BHJ films (100 nm - 15 nm) onto poly(3,4-ethylenedioxythiophene) poly(styrenesulfonate) (PEDOT-PSS) on multiple substrates (silicon, quartz, and glass), we find that the PCBM volume fraction at the PEDOT-PSS/BHJ interface increases as a function of film thickness and the PCBM percentage at the BHJ/air interface decreases as the film thickness is increased. Using this data we believe that BHJ blend films become less phase separated as the film thickness is reduced, primarily due to thin-film confinement effects that out-compete the mechanisms of surface-energy directed interfacial enrichment. Crucially, we observe that ultra-thin (<20 nm) BHJ films have nearly a single-phase (i.e., very little vertical gradient in donor or acceptor volume fraction), which could affect its applicability as a high-performance photoactive layer with reference to lower bimolecular recombination and charge transport benefits seen in phase-segregated BHJ films [48, 49].

The optical modeling of these BHJ systems requires accurate measurements of the optical properties, particularly the complex refractive index, $\widetilde{n} = n + ik$. The change in BHJ nanomorphology and phase segregation that occurs with varying BHJ thickness also causes changes in the complex refractive index of the BHJ layer with varying thickness, including vertical gradients in the refractive index within the BHJ film. While there have been optical studies among different polymer-fullerene blends, to date there have been no detailed studies of the change in complex refractive indices as a function of the thickness, and throughout the thickness, of a BHJ film [28, 50, 51]. Assuming that the phase segregation of a standard thickness (100-200 nm) active layer holds for any thickness will lead to inaccurate calculations and suboptimal designs when exploring new device architectures with varying thickness active layers. We present an analysis of SE data for P3HT:PCBM BHJ films with thicknesses ranging from 15nm to 100nm. Data was collected from films on multiple substrates to account for different surface roughnesses and to increase the number of data sets. An effective medium approximation was used for the film-substrate interface and for the film-air interface. In general, out-of-plane to in-plane optical anisotropy has been seen in P3HT:PCBM films due to the orientation of the P3HT polymer chains [28]. Any preferential molecular orientation changes in these thin films will result in a change in the complex refractive index data [23]. The data is interpreted in terms of a model that divides the BHJ into multiple sections in the substrate-normal direction, allowing a reconstruction of the vertical phase segregation profile (variation of P3HT/PCBM volume fraction ratio in the substrate-normal direction) from the SE data. We corroborate these results from SE via direct measurement of

the P3HT/PCBM volume-fraction using NEXAFS measurements.
The analysis of the ellipsometric data was done using the J. A. Woollam software, WVASE32 (version 3.770). First, the optical constants for the pristine P3HT and PCBM films were obtained. Earlier studies have shown that P3HT films are anisotropic and PCBM films are isotropic [52]. The optical constants for the P3HT films were obtained using a uniaxial model ($\widetilde{n}_x = \widetilde{n}_y \neq \widetilde{n}_z$, where z is the substrate-normal direction). In constructing this model, the first step is to estimate thickness of the film with a Cauchy parameterization [25] in the wavelength region where the film is transparent (>1000 nm),

$$n(\lambda) = A + \frac{B}{\lambda^2} + \frac{C}{\lambda^4} \tag{3.2}$$

$$k(\lambda) = \alpha e^{\beta 12400\left(\frac{11}{\lambda\gamma}\right)} \tag{3.3}$$

where n and k are the real and imaginary parts of the refractive index, and λ is the wavelength. This is a six parameter model where α is the extinction coefficient amplitude, β is the exponent factor, and γ is the band edge. The parameters were determined by a best-fit algorithm.
The thickness obtained via the Cauchy parameterization was verified using alternative methods such as profilometry and Atomic Force Microscopy in tapping mode, and was then used as a fixed parameter in the model. A point-by-point fit - i.e. a direct extraction of n and k calculated from the directly measured SE data (typically referred to as ψ and Δ)[25] on a wavelength-by-wavelength basis - was performed over the entire wavelength range to give a preliminary estimate of the optical constants. These values for n and k were used as a reference to the parameterized model. A generalized oscillator model was used to parameterize the complex refractive index of the film. For the polymer films, we used a uniaxial layer (in order to accurately model anisotropy), with a 4 peak Lorentz oscillator in the in-plane direction and 1-peak in the out-of-plane direction. Two peaks for vibronic exciton transitions (0-0 and 0-1) at $\sim$ 2.05 eV and $\sim$ 2.22 eV, a peak at $\sim$ 2.43 eV for the $\pi - \pi^*$ transition and a peak at $\sim$ 1.5 eV for the delocalized polarons were used [28, 51, 53]. For the fullerene films, we used an isotropic model, a 3-peak Lorentz oscillator with peaks at 3.64 eV, 4.53 eV, and 5.74 eV which can be asigned to PCBM electronic transitions [54]. The Lorentz oscillator was written in the form given in the following equations,

$$\epsilon = \epsilon_1 + \iota\epsilon_2 = (n + \iota k)^2 \tag{3.4}$$

$$\epsilon = \epsilon_1 + \sum_j \frac{A_j}{E_j^2 - (h\nu)^2 - \iota B_j hv} \tag{3.5}$$

where ϵ is the dielectric constant, with real and imaginary parts ϵ_1 and ϵ_2, and Eq. (3.4) relates the dielectric constant to the real and imaginary parts of the refractive index. In Eq. (3.5), h is Planck's constant, ν is the optical frequency, and for a 5-peak oscillator, j = 5 where A_j is the amplitude,E_j is the center energy,B_j is the broadening of each oscillator, and ϵ_1 is an additional offset term varied by the model. The software uses a complete analytical solution to the Kramers-Kronig integral [55].

The optical constants for these films were found without any a priori assumptions. As opposed to PCBM, P3HT films have an absorption spectrum that is highly dependent on the processing conditions of the films [28]. However, control films ($\sim$ 100 nm) were made using similar conditions to the BHJ films and the optical constants we measured were similar to those found in literature [28]. The pure PCBM optical constants were also found be to be close to previously measured values quoted in the literature[28, 56, 57].

Once the optical constants of the pristine P3HT and PCBM films were determined, we modeled the optical data from the blend films using an effective medium approximation (EMA). This was a simple linear combination of the pristine optical constants using the Bruggeman approach [25, 26, 58]. The resulting dielectric function ϵ for the mixture of two materials a and b is given by,

$$\epsilon = \frac{\epsilon_a\epsilon_b + \kappa\epsilon_h(f_a\epsilon_a + f_b\epsilon_b)}{\kappa\epsilon_h + (f_a\epsilon_a + f_b\epsilon_b)} \tag{3.6}$$

where ϵ_a and ϵ_b were the complex dielectric constants of materials a and b repectively, and f_a and f_b were the volume fractions of the two materials. In the Bruggeman approach, $\kappa = 2$ and $\epsilon_h = \epsilon$ [25]. We constructed a model where the optical constants of the pristine P3HT and PCBM were fixed and only the volume fraction of the materials was allowed to vary.

For comparison, a different model for the BHJ blend was also constructed where the blend was considered as an independent material rather than using an EMA. In this approach, the BHJ material was modeled using a uniaxial layer (to account for anisotropy) with a 7-peak Lorentz oscillator in the inplane direction (4 Lorentz oscillators for P3HT and 3 oscillators for PCBM) and a 1-peak Lorentz oscillator in the out-of-plane direction. A linear concentration gradient of the fullerene in polymer/fullerene blend films in the substrate-normal direction was first shown in 2002 by Arias et al. using atomic force microscopy, and in 2008 by Campoy Quiles et al. using SE [27, 50]. The linear nature of the gradient was shown to be over-simplified by Germack et al.[28] by using a three-layer EMA model to show that in the blend films, P3HT enriched regions form at the air/film interface and PCBM enriched regions at the substrate/film interface for high surface-energy substrates. Using neutron reflectivity, Kiel et al. have also shown a similar trend due to surface-energy effects of the substrate [59].

Our ellipsometric modeling uses a three layer EMA approach for films greater than 20 nm thicknesses and a two layer EMA for thinner films. For each of the thicknesses studied, the PCBM volume fraction of the top EMA layer (with thickness of 5 nm) is constrained to be equal to the value measured using NEXAFS. The volume fraction of the other EMA layers was found by minimizing the mean squared error (MSE). For the thicker films ($\sim$ 100 nm - 200), our findings agree with the results of the previous studies [28].

We tested the accuracy and reliability of the ellipsometric model in several ways as shown in the details of SE below. The model was then used to derive optical constants for 90 nm, 45 nm, and 15 nm thick BHJ films. We quantify the optical anisotropy using the anisotropy parameter $A(\lambda)$ in the equation below [60],

$$A(\lambda) = k(\lambda)_{in-plane} - k(\lambda)_{out-of-plane} \tag{3.7}$$

where λ is wavelength, $k(\lambda)_{xy}$ and $k(\lambda)_z$ are the imaginary parts of the refractive index within and perpendicular to the plane of the film, and the variation in the difference between $k(\lambda)_{xy}$ and $k(\lambda)_z$ gives a measure of the anisotropy of the films. Using the multilayer EMA model described earlier, we can also quantify the phase segregation of P3HT and PCBM as a function of depth in the substrate-normal direction of the film. The optical constants and the optical anisotropy in the three regions along with the phase segregation for films of different thickness are shown in Figures 3.1 through 3.3.

In all cases, the optical constants changed as a function of the thickness of the film. Closer to the substrate, the films are PCBM-rich and show values of optical anisotropy in the range of 0 - 0.25. In the top 5 nm of the film, closer to the air interface, the films are P3HT-rich and show values of optical anisotropy in the range of 0 - 0.5. Films of all three thicknesses show a similar trend as a function of depth throughout the film, and the direction of phase

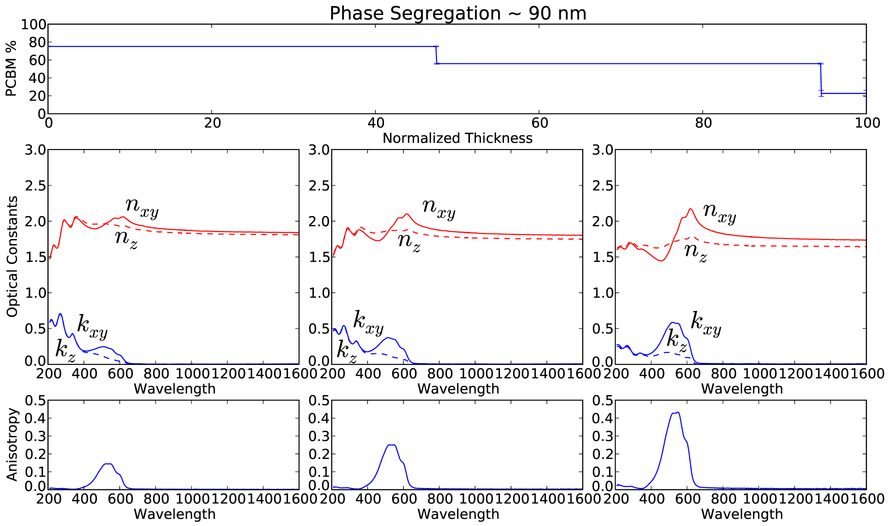

Figure 3.1: Phase segregation, refractive index, and optical anisotropy in different regions of the film for a BHJ film with thickness of 90 nm.

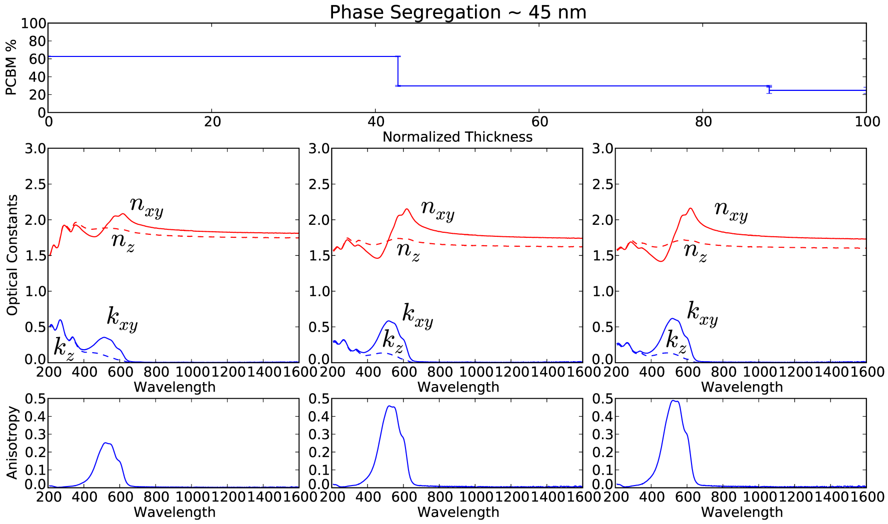

Figure 3.2: Phase segregation, refractive index, and optical anisotropy in different regions of the film for a BHJ film with thickness of 45 nm.

segregation agrees with previous studies for the standard thickness [28].

The introduction of PCBM into P3HT changes the position of the maxi-

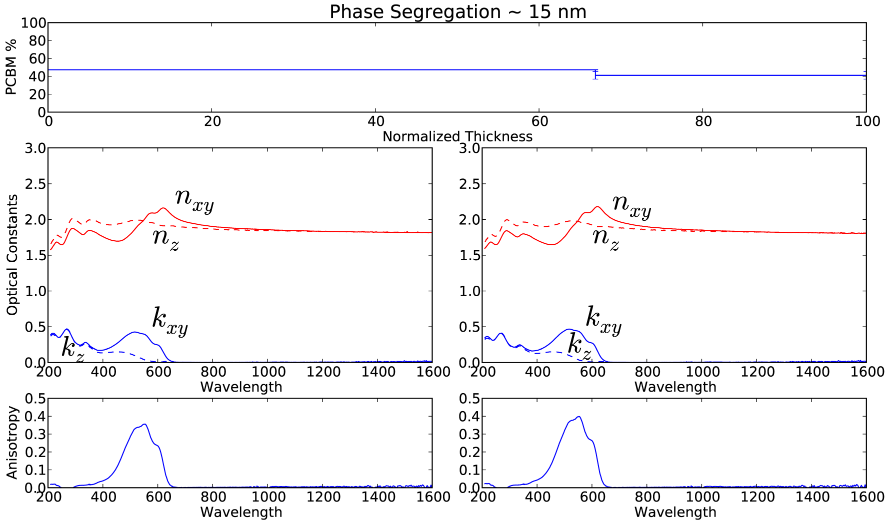

Figure 3.3: Phase segregation, refractive index, and optical anisotropy in different regions of the film for a BHJ film with thickness of 15 nm.

mum of $\epsilon_{2,xy}$ thereby decreasing the anisotropy of the films. This is generally believed to be caused due to torsion and the formation of kinks in the polymer chain [61]. An anisotropy constant of ~ 0 suggests the presence of amorphous P3HT whereas an anisotropy constant of >0 suggests crystalline domains.

While the vertical composition profile of the thicker film agrees reasonably well with previous studies [28, 51, 62], as the film thickness is decreased, the BHJ blends in our study become more homogeneous (phase segregation is reduced). As shown in Fig. 3.5, the PCBM (P3HT) percentage found using NEXAFS in the top 5nm of the films, near the air interface, is found to be 22.9% (77.1%), 24.9% (75.1%), and 41.1% (58.9%) for the 90nm, 45nm, and the 15nm films respectively. Films of greater thicknesses, ∼200 nm and ∼920 nm were also tested further to confirm the trend of vertical separation as a function of the thickness. The phase segregation for 200nm-thick films is very similar to that observed in 100nm-thick films, suggesting an asymptotic limit for film thicknesses $\geq$ 100 nm. As the film thicknesses approach the confinement limit (∼20 nm), as described by the radius of gyration of the polymer, the polymer crystallites and fullerene aggregates are restricted in their movement and cannot produce a vertical gradient in the P3HT/PCBM volume fraction since the domains completely span the film thickness. A depiction of this mechanism can be seen in Figure 3.4.

Using SE, we find that the PCBM percentage close to the substrate is 75.1

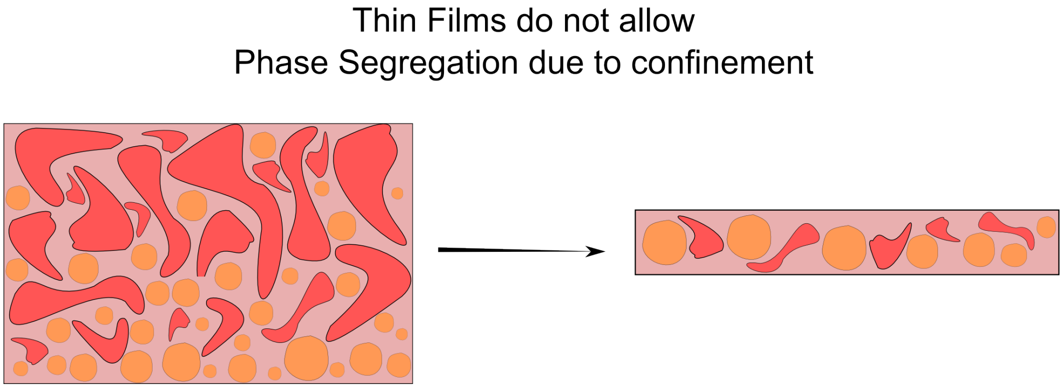

Figure 3.4: As the thickness of BHJ films is reduced to the confinement limit, the movement of P3HT and PCBM domains is restricted due to their size, and since the domains completely span the film thickness in this limit, no vertical gradient in the P3HT/PCBM volume fraction is observed.

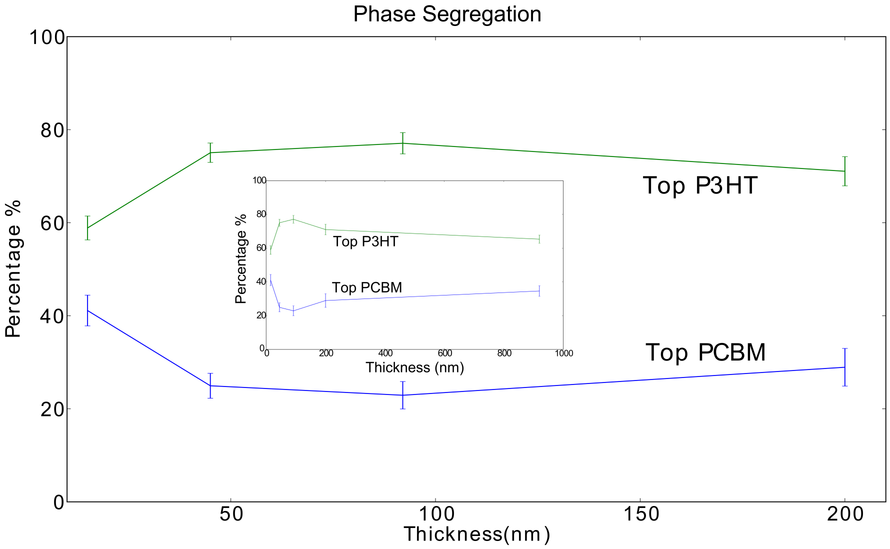

Figure 3.5: P3HT and PCBM percentages in the top 5 nm section of a film as a function of thickness determined using NEXAFS. Errorbars are calculated using the standard deviation of 1000 datasets generated from a bootstrapping technique with replacement. Inset shows P3HT/PCBM percentages as a function of thickness where the thickness varies from 15 nm to 920 nm.

%, 62.7 %, and 47.4 % in films with thickness 90nm, 45nm and 15nm respectively. As shown in Figs. 3.1 through 3.3, these measurements demonstrate a decrease in the vertical separation of the P3HT and PCBM as the thickness of the film decreases. This can be due to a combination of a kinetically limited phenomenon and reduced polymer diffusion due to thin-film confinement [32].

3.2.2 Details of Spectroscopic Ellipsometry Modeling

Maximum Likelihood Estimator

Physical optical models are then used to relate values of ψ and Δ to the complex index of refraction (or dielectric function). The fitting is carried out by representing the quality of the match between the measured data and the modeled data as a maximum likelihood estimator. The mean-squared error (MSE) is used in the software and calculated using the following equation.

$$MSE = \sqrt{\frac{1}{2N-M}\sum_{i=1}^{N}\left[\left(\frac{\psi_i^{mod}-\psi_i^{exp}}{\sigma_{\psi,i}^{exp}}\right)^2+\left(\frac{\Delta_i^{mod}-\Delta_i^{exp}}{\sigma_{\Delta,i}^{exp}}\right)^2\right]} \tag{3.8}$$

The number of ψ and Δ values is given by N, the number of independent parameters is given by M, and σ are the standard deviations in the experimental data points.

Accuracy of the VASE model

In order to get a better estimate of the thickness of the samples, measurements were made using three different techniques. Profilometry and Atomic Force Microscopy were used as supporting techniques to the thicknesses calculated using ellipsometry. Table 3.1 shows the thicknesses from each of the three techniques.

Thickness	10mg/ml	5mg/ml	2mg/ml
Ellipsometry(nm)	103	41	16
Profilometry(nm)	94	40	15
AFM(nm)	98	47	18
Mean(nm)	98.3	42.7	16.3
Standard Deviation (nm)	4.5	3.8	1.5

Table 3.1: Thickness of films at spin cast at 700 rpm from solvents with different concentrations (10 mg/ml, 5 mg/ml, and 2 mg/ml) as measured using different techniques (ellipsometry, profilometry, and AFM).

When interpreting VASE data, care and caution must be taken as too many parameters without physical significance can result in over-fitting of the data or a false conclusion can be derived based on the best fit. An MSE analysis is done to make sure that adding more complexity to the model lowers the MSE, showing that each additional parameter is adding physical significance.

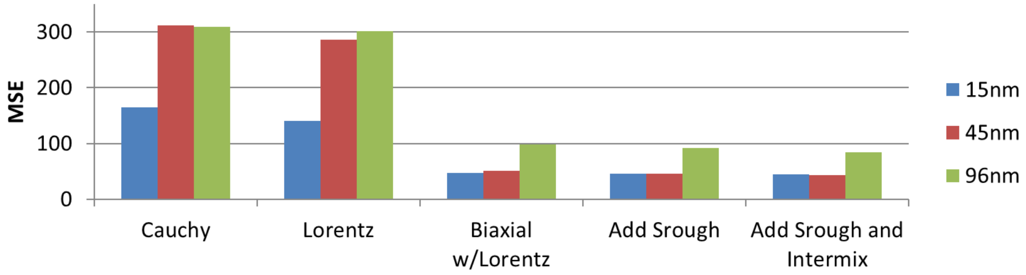

Figure 3.6: Change in Mean Squared Error (MSE) as more complexity is added to the SE model moving from left to right on the horizontal axis.

Initially the films are modeled as a Cauchy oscillator (Cauchy in Fig. 3.6), however the MSE values that result from the fit are very large, as are the MSE values from isotropic Lorentz oscillators (Lorentz in Fig. 3.6. Adding anisotropy to the model seems to be the most important addition (Biaxial w/Lorentz in Fig. 3.6). A roughness layer (Add Srough in Fig. 3.6) can be added into the model using an EMA. Further, an interfacial roughness layer between the film and the substrate (Add Srough and Intermix in Fig.3.6) can also be added using an EMA. These additions also result in lowering the MSE, although by a much smaller amount.

Monte Carlo Analysis

The complex indices of refraction for each of the samples are calculated using a three layer EMA model. Each EMA layer is assumed to be composed of a mixture of pristine P3HT and PCBM. Pure P3HT optical constants for various film thicknesses are derived from films spun from three different concentrations, 10mg/ml (yielding a film thickness of 90nm at spin speed of 700 rpm), 5mg/ml (45nm thick film), and 2mg/ml (15nm thick film) on three different substrates, glass, silicon, silicon with thermal oxide. For a given concentration (film thickness), the optical constants are constrained to be the same on all three substrates. Pure PCBM optical constants are derived from a 10mg/ml solution on three different substrates. To gain more confidence in our model, a Monte Carlo study was performed for each of the model fits. The data was resampled on a per spectrum basis and 100 SE data sets were generated. The spread in the n and k values derived for P3HT from these data sets can be seen in Figures 3.7 (a) - (c).

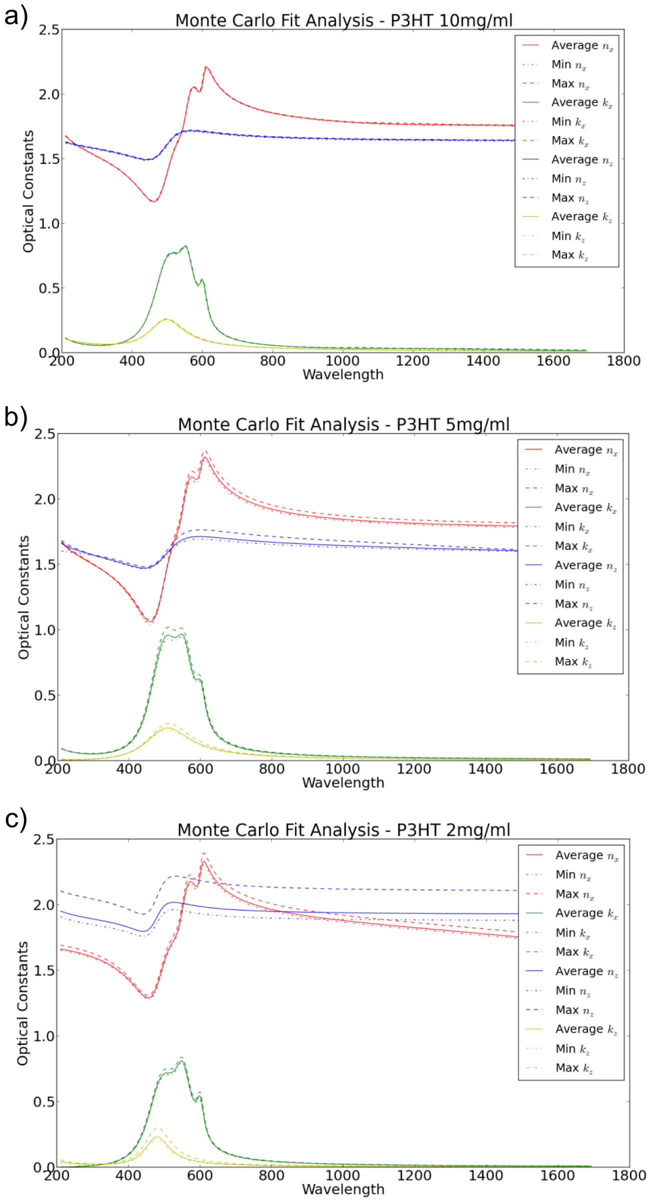

Figure 3.7: Spread in optical constants for P3HT films from concentrations, (a) 10mg/ml, (b) 5mg/ml, and (c) 2mg/ml found using a Monte Carlo Analysis.

P3HT data is anisotropic, and therefore in-plane (denoted as n_x) and out-of-plane (denoted as n_z) can be seen independently on the figures. The complex indices of refraction for each of the samples are calculated using a three layer EMA model. Each EMA layer is assumed to be composed of a mixture of pristine P3HT and PCBM. Pure P3HT optical constants for various film thicknesses are derived from films spun from three different concentrations, 10mg/ml (yielding a film thickness of 90nm at spin speed of 700 rpm), 5mg/ml (45nm thick film), and 2mg/ml (15nm thick film) on three different substrates, glass, silicon, silicon with thermal oxide. For a given concentration (film thickness), the optical constants are constrained to be the same on all three substrates. Pure PCBM optical constants are derived from a 10mg/ml solution on three different substrates. To gain more confidence in our model, a Monte Carlo study was performed for each of the model fits. The data was resampled on a per spectrum basis and 100 SE data sets were generated. The spread in the n and k values derived for P3HT from these data sets can be seen in Figures 3.7 (a) - (c). P3HT data is anisotropic, and therefore in-plane (denoted as n_x) and out-of-plane (denoted as n_z) can be seen independently on the figures.

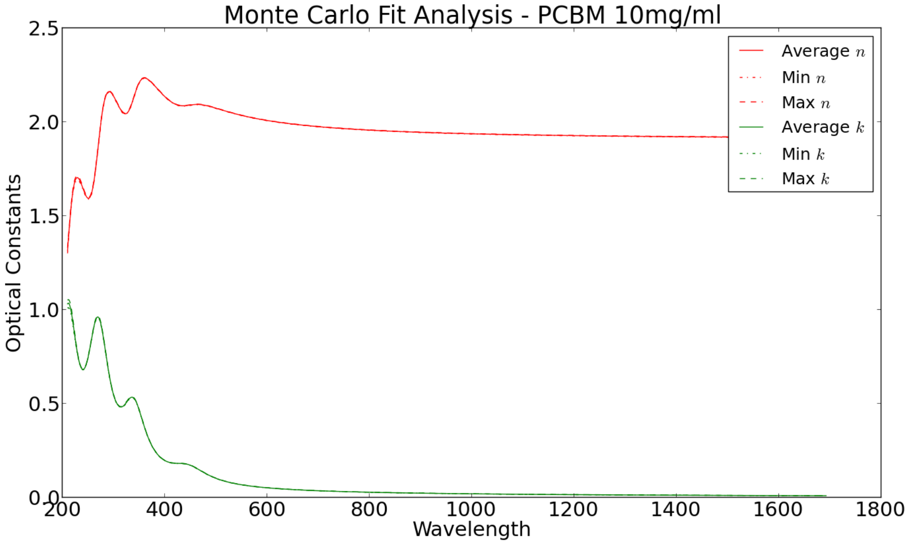

Figure 3.8: Spread in PCBM optical constants using a Monte Carlo Analysis.

The spread calculated using this analysis across the different films is <0.15 for n and <0.03 for k values. A similar Monte Carlo analysis on a pure PCBM film of 10mg/ml yields very minimal deviations from the reference fit. The average, minimum and the maximum n and k values are shown in Figure 3.8 however they appear to lie on the same graph.

A correlation matrix for the parameters is also calculated, and for each of the films the correlation between parameters does not exceed 0.5 for the majority of the parameters, where 0 refers to no correlation and 1 refers to absolute correlation. This reduces the possibility of unphysical results due to parameter correlation. A visual representation of the correlation matrices for a 10mg/ml P3HT film and a 10mg/ml PCBM film can be seen in Figure 3.9 where the parameters are labeled by number on the x and y axes.

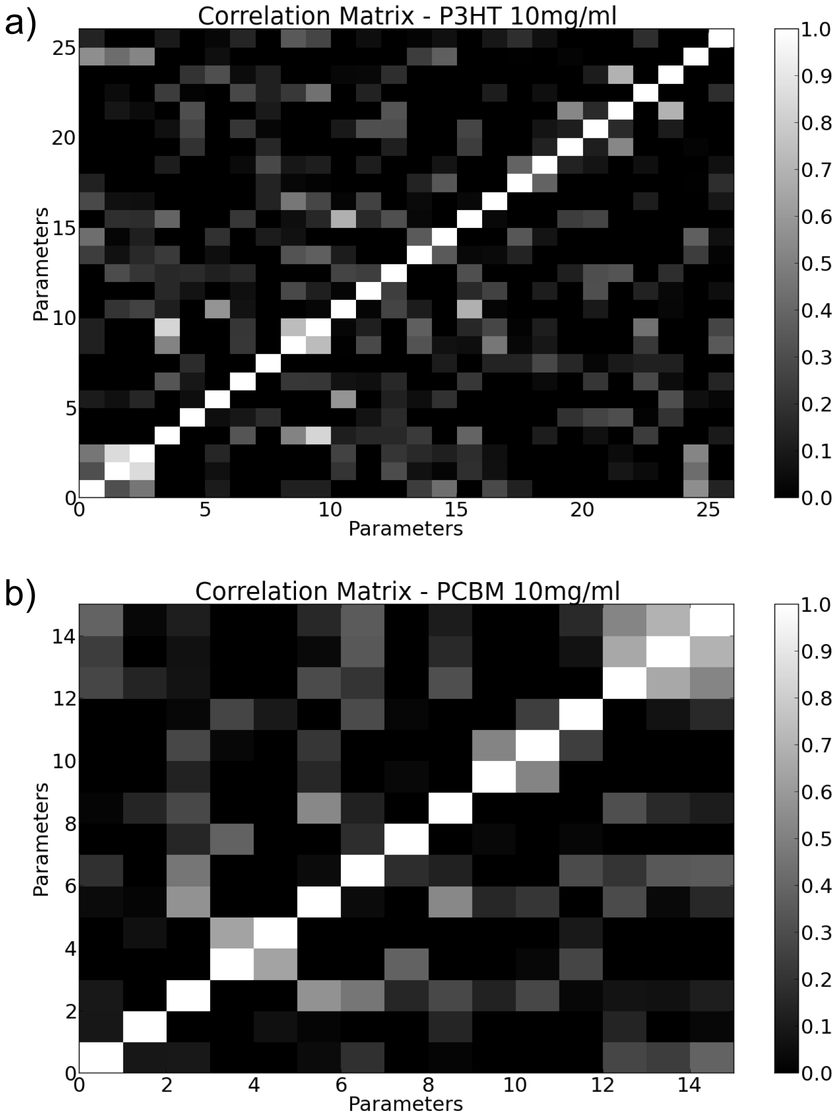

Figure 3.9: Visual representation of correlation matrices for films of pure (a) P3HT and (b) PCBM from a 10mg/ml solution.

In the three layer EMA model used to determine the PCBM volume fraction, the optical constants from above are used in the EMA layers. The top

EMA layer volume fraction is fixed to the PCBM percentage calculated from NEXAFS data and the middle and bottom EMA layers are allowed to vary. We can get an MSE surface by changing the PCBM volume fraction individually for each of these layers and observing the change in MSE. A relative MSE color plot can be seen in Figure 3.10 for the three layer EMA model used for film thicknesses >30nm.

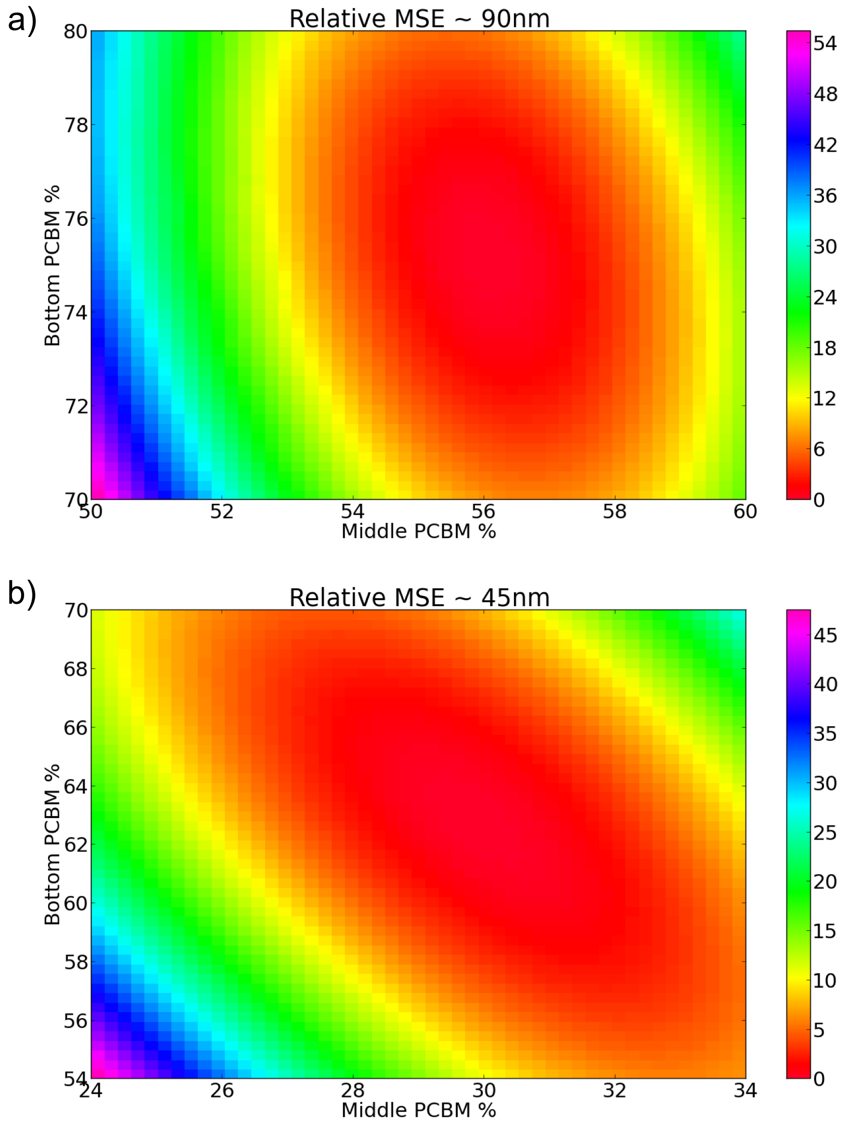

Figure 3.10: Relative MSE (difference between MSE for given parameters and MSE for optimal parameters),while individually changing middle and bottom PCBM volume fractions for (a) 90nm and (b) 45nm films.

For the film with thickness $\sim$ 15nm, a two layer EMA was used where the top EMA layer of 5nm had a fixed PCBM volume fraction from NEXAFS data. The bottom PCBM percentage was allowed to vary. An MSE analysis where the parameter was indivudally varied is represented in Figure 3.11.

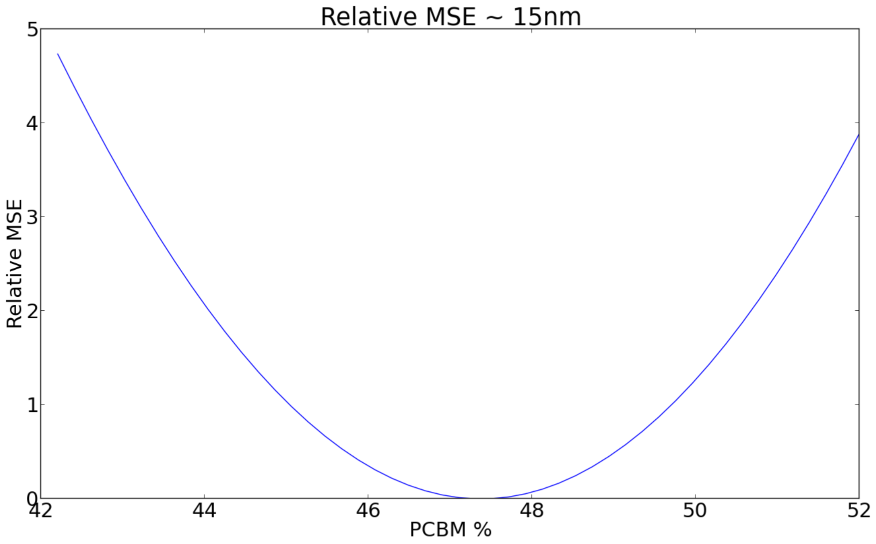

Figure 3.11: Realtive MSE from a 15nm film where the bottom PCBM fraction is varied.

NEXAFS spectra from pure P3HT and PCBM films were extracted individually. A linear combination of these spectra were then used to fit the spectra obtained from the blend films, thus yielding the P3HT and PCBM volume fractions in the top 5nm of the film.

An example is shown in Figure 3.12, where a blend film of 90nm thickness is compared to pure P3HT and PCBM spectra. The error bars for the volume fraction are calculated using a bootstrapping routine where 1000 data sets are generated with replacement using the standard deviation in the weighted average of the residuals from the raw data and the fitted data. All generated data sets are fitted and the standard deviation in each of the parameters gives the error.

NEXAFS is only sensitive to the volume fraction in the top 5 nm therefore in each model the top layer is fixed at 5 nm. This is the escape depth of the electrons from the sample and therefore cannot be varied. The electron escape depth is determined by the electron kinetic energy, and 5nm is the upper limit of what you can reach for the given beam energy. The volume fraction in the top 5nm of the film as determined by NEXAFS is then fixed in the top layer

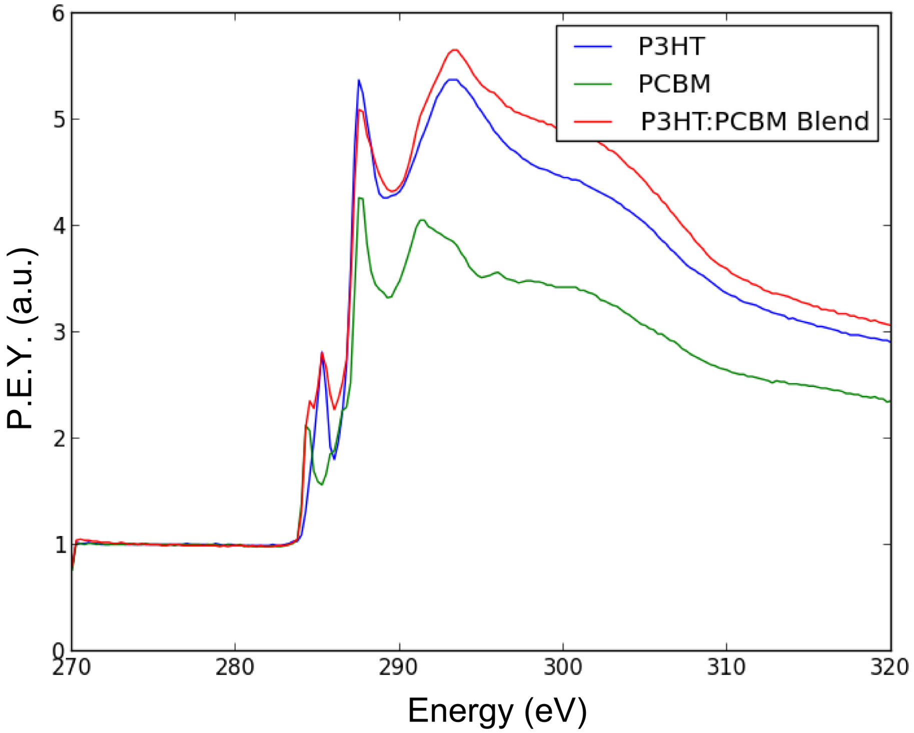

Figure 3.12: NEXAFS Spectra from pure P3HT, pure PCBM, and a blend film.

in the SE model.
The major distinguishing feature in the three spectra is the peak close to the carbon K edge at $\sim$ 285eV. We can focus into the carbon K edge peak by looking at the energy range of 284 - 286eV. This is shown in Figure 3.13.

3.2.3 Decreased Disorder in Thin Films

As previously mentioned, in addition to the EMA model used above, a different model for the BHJ blend was also developed where, the electronic transitions are allowed to shift in energy, amplitude, and width compared to the optical constants of pristine P3HT and PCBM films. This model is physically justified by previous studies where the addition of PCBM into P3HT was shown to reduce the degree of order of P3HT within the films [63]. This is believed to be caused by the formation of smaller P3HT domains and the increase in breaks and kinks in the polymer chain caused by the addition of PCBM. Regioregular P3HT can be modeled as a weakly interacting H-aggregate for

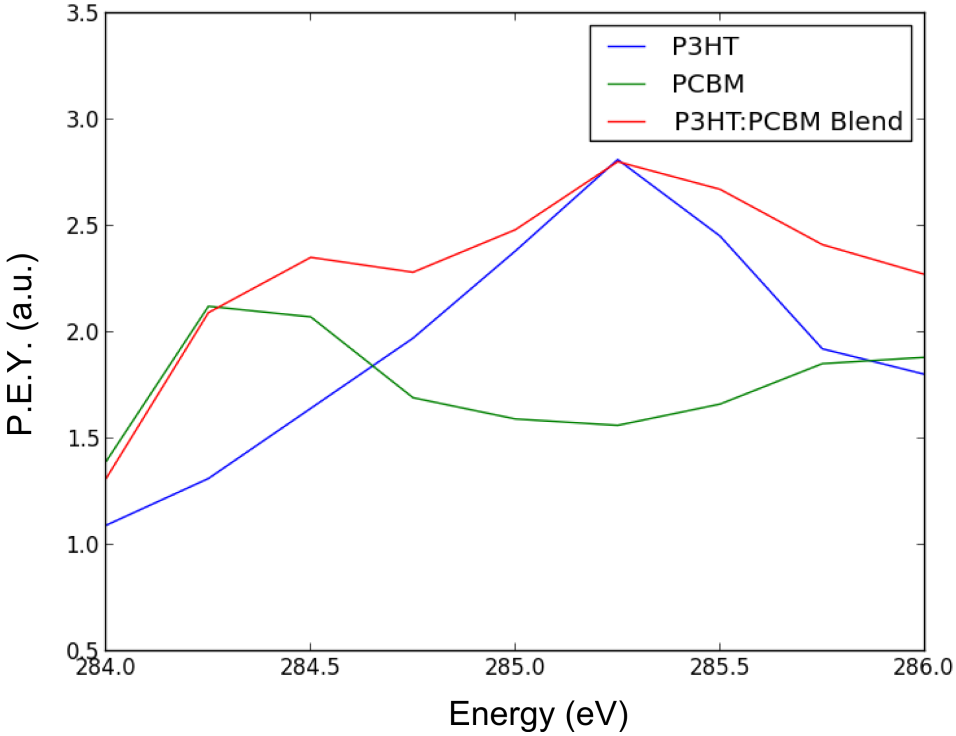

Figure 3.13: Spectra for P3HT, PCBM, and a blend shown in a smaller energy range.

herringbone and lamellar morphologies [64]. The in-plane imaginary part of the dielectric constant as reconstructed using this model for pure P3HT and the BHJ blend is shown in Fig. 3.14 (a), along with a schematic of the weakly interacting H-aggregate transitions in Fig. 3.14 (b).

In order to understand the effect of changing the thickness of the BHJ blend layer on the conjugation length and the optical order of the film, we compare the degree of excitonic coupling within the aggregates. The ratio of the peak heights of the first (0-0) and second (0-1) single exciton state in P3HT is related to W, the free exciton bandwidth, and E_p, the energy of the intra-molecular vibrational mode [64, 65]. Assuming a Huang-Rhys factor of 1, this relationship is given by

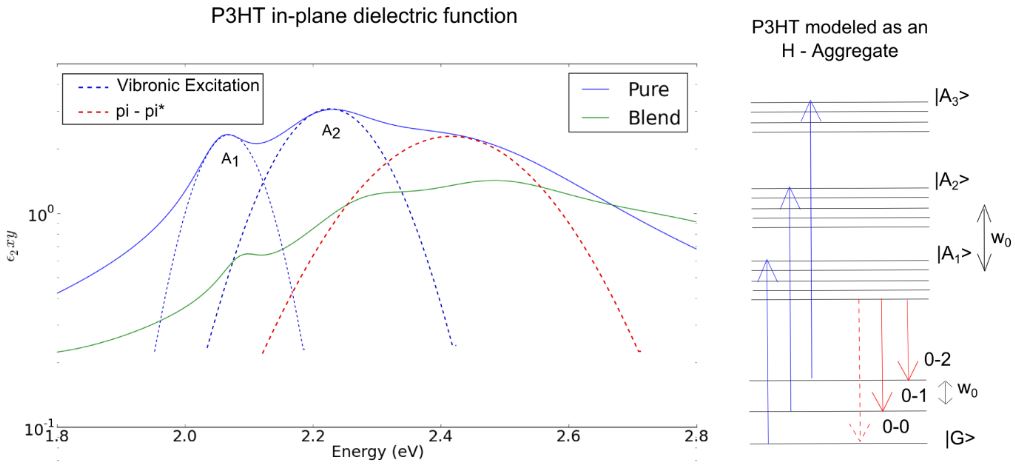

Figure 3.14: Imaginary part of the dielectric function showing transitions in P3HT and an energy level diagram for a weakly interacting H-aggregate.

$$\frac{A_{0-0}}{A_{0-1}} \approx \left(\frac{1 - \dfrac{0.24W}{E_p}}{1 + \dfrac{0.073W}{E_p}} \right)^2 \tag{3.9}$$

If we assume that a symmetric stretch at 0.18 eV dominates the coupling to the electronic transition [66], the exciton bandwidth, W can be determined. At a given thickness, we determine W_{EMA} from an EMA model where electronic transitions are not allowed to vary and are fixed to pristine P3HT values and W_{Blend} where the electronic transitions are assumed to be of an independent material and are allowed to vary from the starting values of pristine P3HT. Values for WEMA agree well with literature values for pristine P3HT of $\sim$ 120 meV, depending on the solvent and concentration [67]. We find W_{EMA} to be 108.6 meV, 146.0 meV and 121.0 meV for pristine P3HT films spun from solutions of 10 mg/ml, 5 mg/ml, and 2 mg/ml respectively. As expected, there is no significant change of the exciton bandwidth when the BHJ P3HT transitions are assumed to be the same as that in pristine P3HT. However, we find W_{Blend} to be 255.0 meV, 258.4 meV, and 136.2 meV for 90 nm, 45 nm and 15 nm respectively. The exciton bandwidth significantly increases for a standard-thickness films (>20 nm) after we allow the parameters in the fit to vary. As W increases, the A_1 diminishes with respect to A_2 and the vibronic peaks become irregularly spaced. An increase in W suggests a decrease in the conjugation length and order [68, 69]. This decrease can be caused by the addition of PCBM which causes an increase in breaks and kinks in the P3HT film. The degree of the decrease in conjugation length can be studied by looking at the change in the exciton bandwidth ($\Delta W = W_{Blend} - W_{EMA}$) as a function of the thickness. The shift in the 0-0 and 0-1 energy peaks ($\Delta E_{0-0} = E_{0-0Blend} - E_{0-0EMA}, \Delta E_{0-1} = E_{0-1Blend} - E_{0-1EMA}$) also give a sense of the disorder caused by the addition of PCBM. The shifts in energy and in the exciton bandwidth are shown in Figure 3.15. The error bars represent a 90% confidence interval.

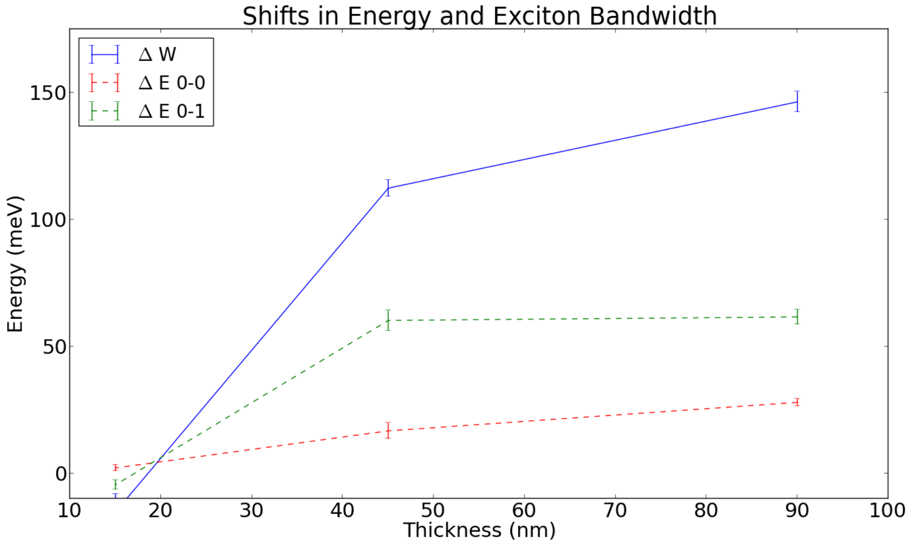

Figure 3.15: Change in exciton bandwidth (ΔW) and shifts in energy (ΔE_{0-0} and ΔE_{0-1}) shown as a function of thickness.

For film thicknesses 45nm and 90 nm, the addition of PCBM appears to cause an increase in disorder and a decrease in conjugation length for P3HT, as demonstrated by the large and positive values of ΔW, ΔE_{0-0}, and ΔE_{0-1} for these thicknesses. For the 15nm thick film, ΔW, ΔE_{0-0}, and ΔE_{0-1} are all near zero, suggesting that the degree of order and conjugation length of P3HT is unaffected by the addition of PCBM in these ultrathin films. This may be due to kinetics of film formation (time of drying etc.) or thin-film confinement effects for these ultrathin films.

This section outlined the study of the change in optical anisotropy and the vertical polymer-fullerene composition profile in BHJ blend films at different thicknesses using spectroscopic ellipsometry and NEXAFS. Using a multiple-sample analysis and thickness measurements from different instruments, the anisotropic complex refractive index of blend films was determined. Using this model and NEXAFS studies to find the polymer/fullerene ratio at the interfaces of BHJ films, we determine the vertical polymer-fullerene concentration profile as a function of the thickness of the film. As the film thickness is decreased toward the thin-film confinement regime, the films are found to become less phase segregated. Further it is seen that the degree of disorder and conjugation length of P3HT increase significantly for 45nm- and 90nm-thick films, but are unaffected for 15nm-thick films. This study demonstrates that due to morphological changes, compared to standard-thickness (∼100nm) films, ultrathin BHJ films (<20 nm) show drastically different optical behavior that must be considered when designing thin-film photovoltaics.

3.3 Crystalline Microstructure

In addition to the VASE analysis on disorder outlined in the previous section, we also investigated the effect of confinement on the coherence length and the crystalline microstructure of the polymer component of polymer:fullerene bulk heterojunction thin films using grazing incidence wide angle x-ray scattering. The details of the technique can be found in Section 3.1. We find that the polymer crystallite size decreases and the alignment of the molecules along the surface normal increases, as the thin-film thickness is reduced from 920nm to <20nm and approaches the thin-film confinement regime. Furthermore, we find that the polymer crystallite size near the surface (air interface) is lower than the crystallite size in the bulk or the bottom (substrate interface) of bulk heterojunction films thicker than the confinement regime. Variation in polymer crystallite size can cause changes in charge carrier mobility and recombination rates, which in turn affect the performance of bulk heterojunction thin film devices such as photovoltaics and photodetectors.

3.3.1 Decreasing Polymer Crystallite Size due to Confinement

The vertical confinement (film thicknesses below the typical coherence length) of a polymer:fullerene bulk heterojunction (BHJ) thin film causes a significant change in fundamental material properties compared to bulk systems as seen in the previous sections [32–34, 70]. Thin-film confinement of semi-crystalline polymers has been of great interest recently [70–74], however the effect of confinement on the structure of the polymer within polymer:fullerene BHJ films has not been given as much attention. The addition of fullerene may have significant implications on the process of aggregation and crystallization of the polymer. Furthermore due to the vertical phase segregation of the polymer and the fullerene within a BHJ, there can be depth dependent variation of polymer crystallization which has remained unexplored in earlier studies on pure polymer systems [53, 62, 75, 76]. Here we investigate the variation of the polymer crystallite size within a BHJ as a function of film thickness and as a function of depth within the film. This is fundamental to the understanding of the BHJ system and its application to various optoelectronic devices such as organic photovoltaics and photodetectors [77, 78]. In BHJ films, within a thickness regime of 100-200 nm, the morphology has been shown to be affected by various processing conditions such as choice of solvent, drying time, thermal treatments, and the use of solvent additives [37, 38, 49]. These morphological variations directly impact the optical and electronic properties of the BHJ layer critical for device applications [75, 79]. In order to direct efforts to design new polymers and thin film architectures, an in-depth understanding of BHJ microstructure and its variation due to additional complexities such as phase segregation is critical.

This section will focus on using grazing incidence wide angle X-ray scattering (GIWAXS) to probe the structure of a poly[3-hexylthiophene-2,5-diyl] (P3HT) and [6,6]-phenyl C61 butyric acid methyl ester (PCBM) BHJ layer. We find that as the thickness of the BHJ is decreased to the ultrathin regime of <20nm, surface-energy effects at the interfaces and kinetics of film formation play an increasingly important role in determining the BHJ microstructure. Additionally, we probe variation with depth within a film by employing surface-sensitive GIWAXS (angle of incidence = 0.07° <the critical angle of 0.1°, yielding a depth sensitivity of $\sim$ 11nm) on as-cast BHJ films as well as BHJ films that have been inverted onto a new substrate exposing the buried interface of the film. These results allow us to directly measure the variation in microstructure at the interfaces (air/film, film/substrate) and compare them to the bulk.

The polymer in BHJ films crystallizes with a lamellar alignment parallel to the substrate with the side-chain groups perpendicular to the substrate. In the conventional crystallographic notation this lamellar direction is defined as $\langle 100 \rangle$ [78]. We use the term crystallite to refer to a set of π-stacked conjugated polymer segments that participate in lamellar stacking and result in diffraction peaks in the grazing incidence geometry. The coherence length as determined using the FWHM of the $\langle 100 \rangle$ scattering peak is identified as the average crystallite size in this direction. Although several studies have tried to quantify the extent of disorder in polymers in various ways [63, 73, 80, 81], in this thesis we use the FWHM of the normalized scattering intensity as a function of the polar angle χ with respect to the surface normal at the q-vector of the $\langle 100 \rangle$ peak, as a measure of the extent of alignment of the polymer molecules (molecular packing order) along the surface normal. As the FWHM decreases, the molecular packing order increases.

Using spin-cast BHJ films (thicknesses ranging from 15nm - 920nm) on poly(3,4-ethylenedioxythiophene) poly(styrenesulfonate) (PEDOT-PSS), we find that the polymer crystallite size in the bulk of the film increases from 6.86 (+/- 0.04) nm to 21.49 (+/- 0.19) nm as the film thickness increases from 15nm to 920nm, with the asymptotic crystallite size of $\sim$ 21nm occurring for film thicknesses $\geq$ 200nm. The molecular packing order, as defined above, decreases as the film thickness is increased. Additionally, we find that the crystallite size on the surface of a BHJ film thicknesses >100nm is reduced compared to the crystallite size at the buried interface between the BHJ and the PEDOT-PSS.

The polymer in BHJ films crystallizes with a strong degree of lamellar alignment parallel to the substrate with the side groups perpendicular to the substrate ("edge on", as shown in Fig. 3.16). We define q_z as the component of the scattering vector, q, perpendicular to the sample surface, while $q_{x,y}$ is defined along the sample surface. The 2D GIWAXS pattern in Fig. 3.16 shows three peaks $\langle h00 \rangle$ in the substrate-normal (q_z) direction. Extracting a line cut in this direction allows us to calculate the spacing between the P3HT lamellae in the substrate-normal direction. For a film with a thickness of 92nm we measure a layer spacing of $\sim$ 1.7nm, which is consistent with previous reports [37, 76–78]. We have computed the P3HT crystallite size from the $\langle h00 \rangle$ scattering peak-width using a Scherrer analysis, accounting for instrumental broadening of the peak and intersection of the scattering with the detector geometry [82]. Instrument details can be found in Section 3.1. For a film with a thickness of 92nm we obtain a polymer crystallite size of 19.8nm, which agrees with polymer crystallite size in BHJ films from previous reports [37, 76–78].

BHJ films of different thicknesses (ranging from 15nm - 920nm) were spun on PEDOT-PSS/Glass substrates. The thicknesses were determined using variable angle spectroscopic ellipsometry, profilometry, and AFM as outlined the previous section. Fig. 3.17 shows the P3HT crystallite size as well as the layer spacing in the substrate-normal direction between the P3HT lamellae. We find that as the thickness of the active layer is reduced, the crystallite size of the polymer decreases. In the ultrathin film of 15nm, we find that the crystallite size decreases to 6.9nm as a combination of confinement and enhanced solvent evaporation frustrate the crystallization process and produce smaller P3HT crystallites. For films of thickness >100nm, the crystallite size

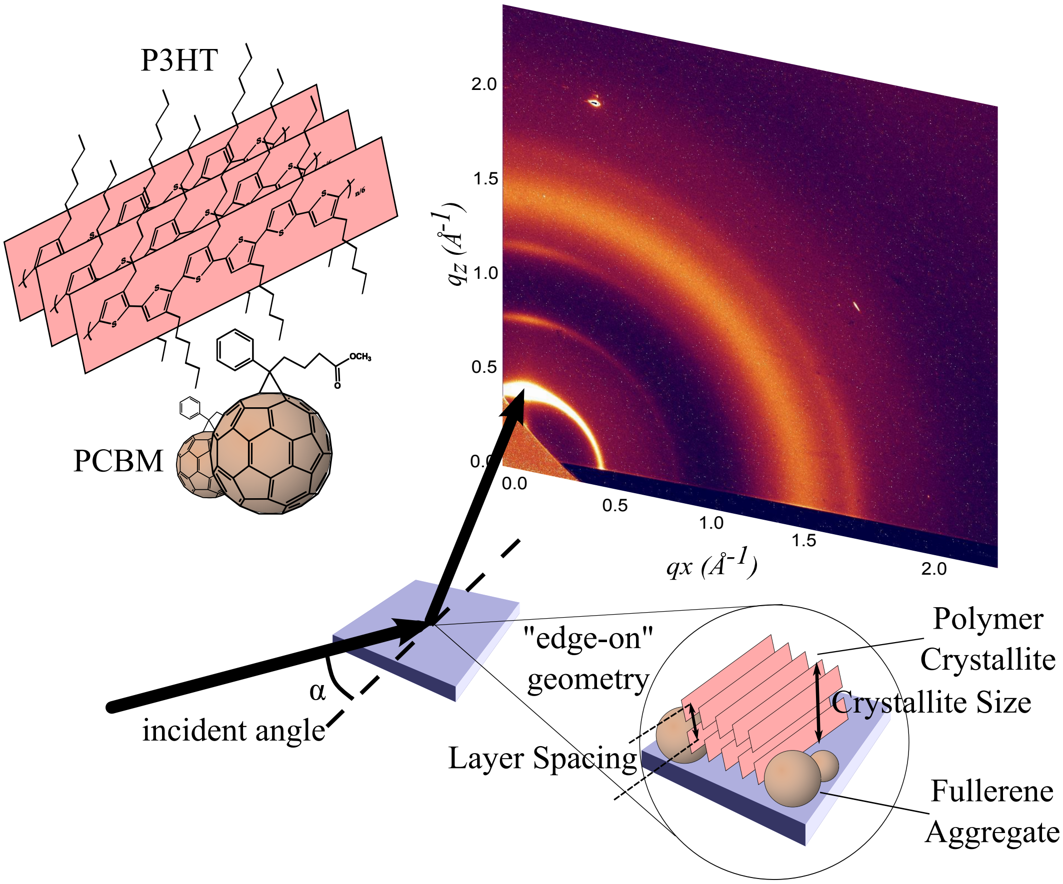

Figure 3.16: Schematic of the GIWAXS measurement geometry. The polymer chains are shown to form a crystallite in the edge-on orientation. In this alignment the P3HT back-bone is oriented parallel to the substrate, and the side chains pointing in the substrate-normal direction.

approaches ∼ 21nm as an asymptotic limit. In order to confirm crystallite size saturation, a thick film of 920nm is also measured for which the polymer crystallite size does not change significantly. Furthermore, using a line cut along $q_{x,y}$ to calculate the isotropic crystallite size for films thicker than 200nm, we have verified that no significant variation can be seen in the crystallite size due to P3HT orientation. The molecular layer spacing within the polymer in the substrate-normal direction was also measured and is shown in Fig. 3.17. Although there are small variations (<1 Å) as the thickness of the BHJ is increased, the molecular layer spacing remains at ∼ 1.7nm.
Additionally a peak at $\langle 010 \rangle$ is also visible representing the $\pi - \pi$ stacking direction. Crystallite sizes in this direction are calculated to be ∼ 4nm and the $\pi - \pi$ stacking distance ∼ 0.4nm consistent with previous reports [37].

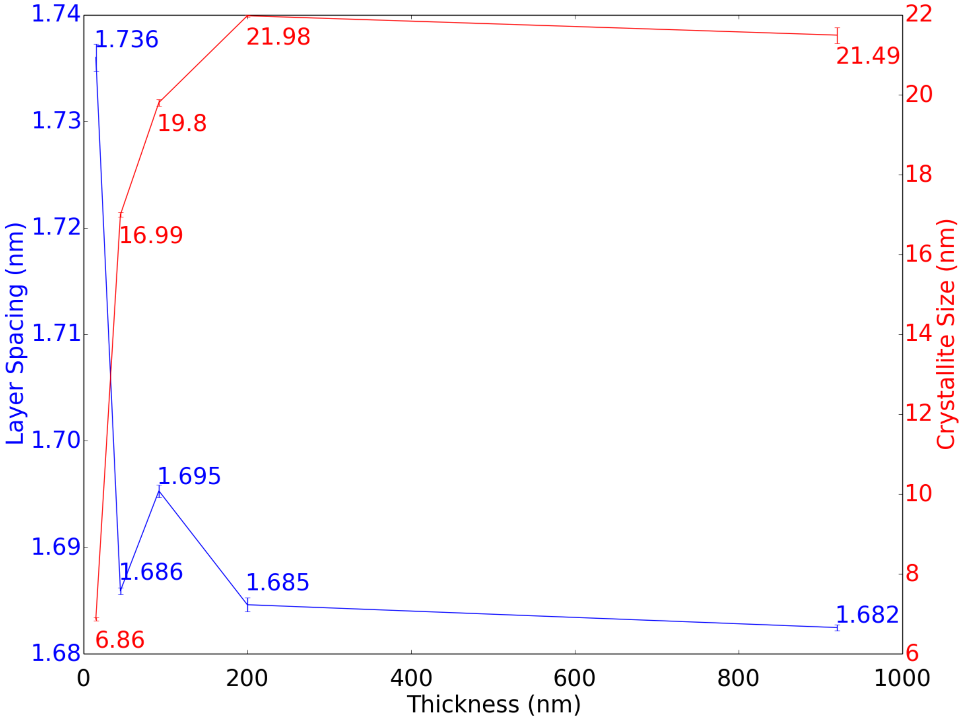

Figure 3.17: Polymer crystallite size (red, right) extracted using the Scherrer analysis as discussed in the text and layer spacing between polymer molecules in the surface normal direction (blue, left) for BHJ films of various thicknesses. The error bars represent the standard deviation from multiple spots on the film. Solid lines are to guide the eye.

The P3HT in BHJ thin films shows a strong preference for edge-on orientation. In this alignment the P3HT back-bone is oriented parallel to the substrate, with the backbones stacked in the substrate-normal direction and the P3HT side chains pointing in the substrate-normal direction [77, 83, 84]. This most likely arises from surface effects at the substrate/BHJ and the BHJ/air interface, where the P3HT side-chains preferentially interact with these interfaces to lower overall surface energy. This effect of interface alignment has been shown previously in liquid crystals and decays exponentially from the interface towards the bulk [85]. As the thickness of the BHJ film is reduced, the substrate/BHJ and the BHJ/air interfaces are brought closer together therefore further aligning the P3HT layers. The normalized scattering intensity as a function of the polar angle χ, with respect to the surface normal at the q-vector of the ⟨100⟩ peak, gives us a measure for the P3HT orientation. Fig. 3.18 (a) shows that the lamellar alignment is predominantly parallel to the substrate (i.e., edge-on alignment) at $\chi \sim 0$.

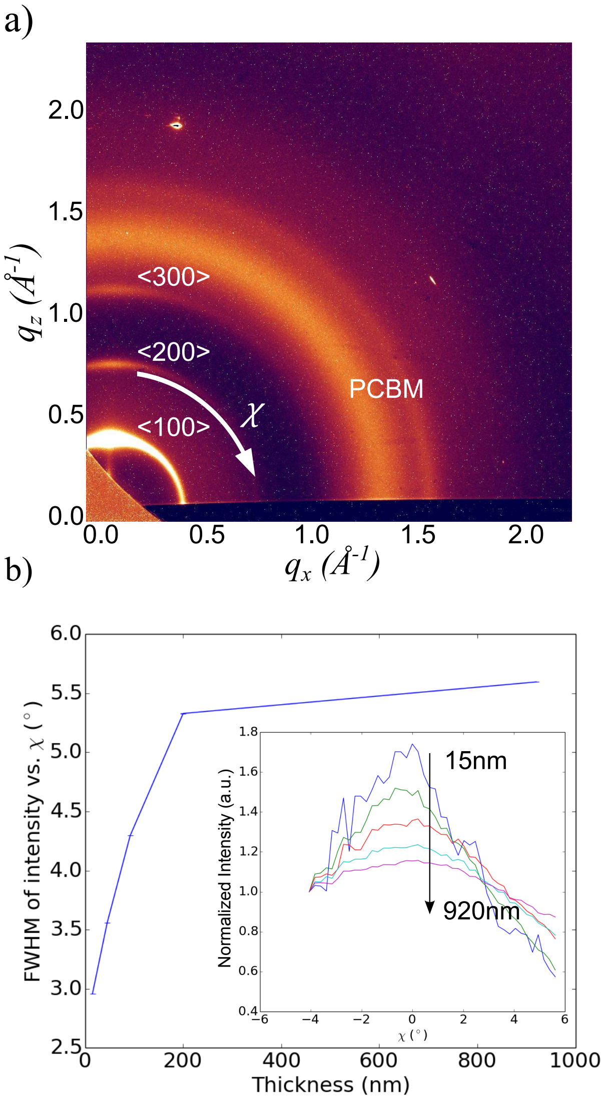

Figure 3.18: (a) Two-dimensional scattering image for polymer:fullerene BHJ thin film showing polymer lamellar alignment parallel to the substrate (edge on) as demonstrated by the $\langle h00 \rangle$ scattering peaks, and a characteristic diffuse PCBM scattering ring. Also shown is the direction of the polar angle χ. (b) The full width at half maximum (FWHM) of the normalized intensity vs. χ at the ⟨100⟩ peak position for films of different thicknesses. Inset shows the normalized intensity (a.u.) vs. χ for films of different thicknesses.

The inset in Fig. 3.18 (b) shows the normalized scattering intensities for different film thicknesses as function of χ around $\chi \sim 0$. Fitting the intensity to a Gaussian profile provides the FWHM, which is used as a measure of the extent of P3HT alignment. Fig. 3.18 (b) shows that as the film thickness is reduced from a BHJ film of >100nm to the thin-film confinement regime, the FWHM decreases indicating that the P3HT layers become further aligned along the edge-on direction. This agrees well with the results from the VASE measurements shown in the previous section where P3HT crystallites were seen to become more ordered as the thickness of a BHJ film is reduced.

3.3.2 Interfacial Reduction in Crystallite Size on the Surface

Surface energy effects at the interfaces of a BHJ film have been shown to cause a linear concentration gradient of the polymer in a polymer:fullerene blend film in the substrate-normal direction [28, 51, 62, 75]. An interfacial layer of high polymer concentration is formed at the BHJ/air interface and an interfacial layer of higher fullerene concentration is formed at the substrate/BHJ interface.

The inset in Fig. 3.19 shows the change in the crystallite size for films of different thicknesses in the top, bulk and the bottom of the film. The top of the film is probed using a surface sensitive GIWAXS angle of 0.07° (critical angle for this film $\sim 0.1°$). For a BHJ film, this gives a depth sensitivity of 11.6nm from the air interface. The sample is then immersed in a water bath to dissolve the PEDOT-PSS and float the BHJ film. A clean substrate is then used to recover the BHJ film but inverted from its initial state. This film is dried by flowing nitrogen and then left in vacuum overnight. Scattering data collected at a grazing incidence angle of 0.07° on this film then gives us information from the bottom 11.6nm of the original BHJ film, the part of the film that was previously adjacent to the PEDOT:PSS layer. It is important to point out that for a 15nm thick film, the regions to which we are sensitive in the original and inverted films overlap in the middle $\sim$ 9nm. Therefore scattering data on this film serves as a check to validate that the process of the inversion does not affect the GIWAXS measurement results. The inset in Fig. 3.19 also shows the bulk crystallite size calculated using a 0.2° incident angle as a reference.

We find that in the top 11.6nm of the BHJ film near the air interface, the crystallite sizes are smaller than at the PEDOT:PSS interface or in the bulk. This is true for films of thickness $\geq$ 92nm. For the ultrathin films, the crystallite size at the air interface $\approx$ crystallite size at the PEDOT:PSS interface. This confirms that the inversion process does not affect the results. Fig. 3.19 shows the change of crystallite size (Δ Crystallite size) from the bottom 11.6nm (PEDOT:PSS interface) to the top 11.6nm (air interface). For the ultrathin films the variation is ∼ 0nm as we are probing roughly the same volume in both cases. However for the films with thickness ≥100nm, we measure a decrease of about 5-7nm in the crystallite size between the bottom (PEDOT:PSS interface) and the top (air interface) of the film.

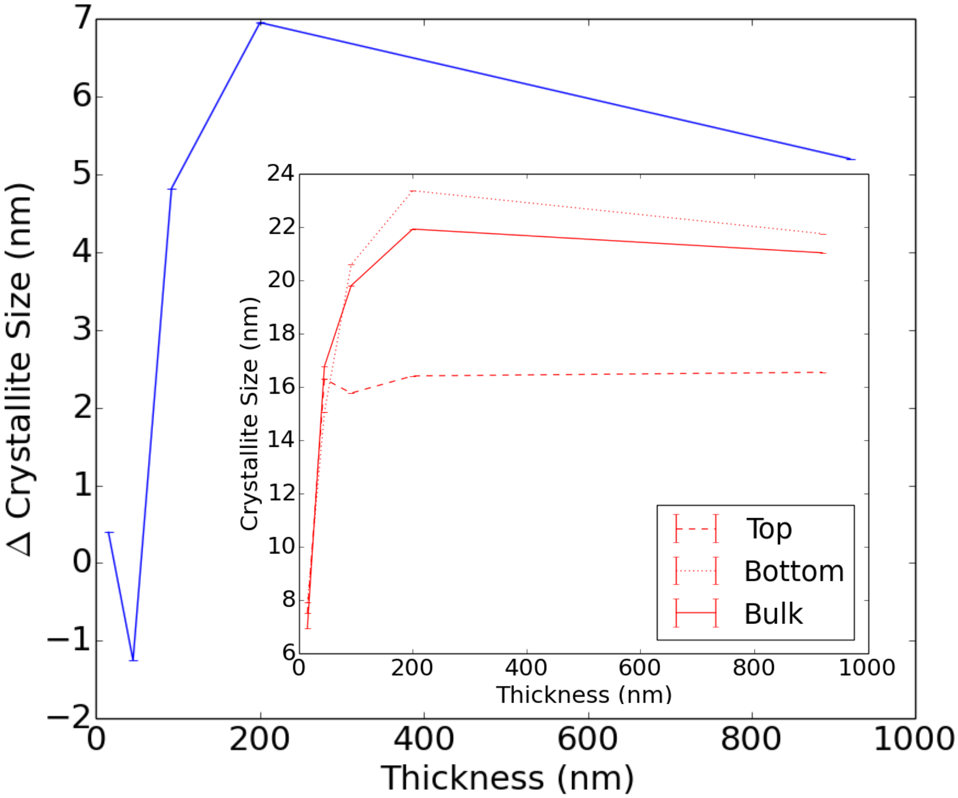

Figure 3.19: The difference in the polymer crystallite size (Δ Crystallite size (nm)) between the bottom (∼11nm) and the top (∼11nm) of the BHJ film as a function of film thickness. The inset shows the calculated polymer crystallite sizes in the top (surface sensitive GIWAXS on the as-cast film), bottom (surface sensitive GIWAXS on a film that was physically inverted from its original state), and the bulk (GIWAXS at an incidence angle well above the critical angle) of the BHJ film.

Although the variation in crystallite size with film depth could naively be attributed to differences in PCBM concentration due to phase segregation, in order to understand the effect of a PCBM concentration gradient on the polymer crystallite size we measure the bulk polymer crystallite size using GIWAXS from samples of different blend ratios (but of the same concentration). Blend ratios of these samples are chosen such that the polymer volume fraction in these is similar at the air interface, bulk, and the PEDOT:PSS interface in a phase segregated film of thickness >100nm [75]. For BHJ films with P3HT:PCBM ratios of 1:2, 1:1, and 2:1, we calculate a bulk crystallite size of 19.5nm, 21nm, 17.5nm respectively. The bulk crystallite size of the polymer in a BHJ film does not vary significantly with polymer fraction (in the range of polymer fraction variation that can be seen within a phase segregated film). Therefore, the observed variation of crystallite size within the film depth cannot be due to the change in the PCBM fraction, but can likely be attributed to the variation in the kinetics of film formation.

The Avrami equation can be adopted as a rough model to understand the kinetics of crystallization within BHJ films [86]. The Avrami expression has been used previously to model the extent of phase-volume development as a function of time [76]. In our case, the films are in a steady state after the process of crystallization has already been completed. However there is a variation of the extent of phase development as a function of the depth of the film due to the time it takes for the solvent to escape from different sections in the film. Therefore we develop an Avrami expression where the phase development of crystallization, α, is written as a function of the *distance* from the air interface, x (for $x \geq 0$), within a BHJ film:

$$\alpha(x) = 1 - e^{-Kx^n} \tag{3.10}$$

where K is the rate constant and n is the Avrami exponent. To quantify the extent of polymer crystallization, α, we use the integrated intensity of the $\langle 100 \rangle$ peak over q_z normalized by the maximum intensity value [76].

For each film, we calculate α for three points in the depth of the film: the top 11.6nm, the bulk that is used as the center value, and the bottom 11.6nm. The calculated Avrami exponent (n) and the rate constant (K) for BHJ films of different thicknesses are shown in Fig. 3.20. The error bars are calculated using the covariance matrix from the least squares fitting of the data to Eq. 3.10. The inset in Fig. 3.20 shows $\alpha(x)$ as a function of the normalized depth for BHJ films of three difference thicknesses (15nm, 45nm, and 92nm). The solid lines represent the normalized best fit curves to Eq. 3.10. The rate constant for films in the thin-film confinement regime is higher than films of larger thicknesses, suggesting that the crystallization in the thinner films is more rapid as a function of depth. In films of larger thicknesses,

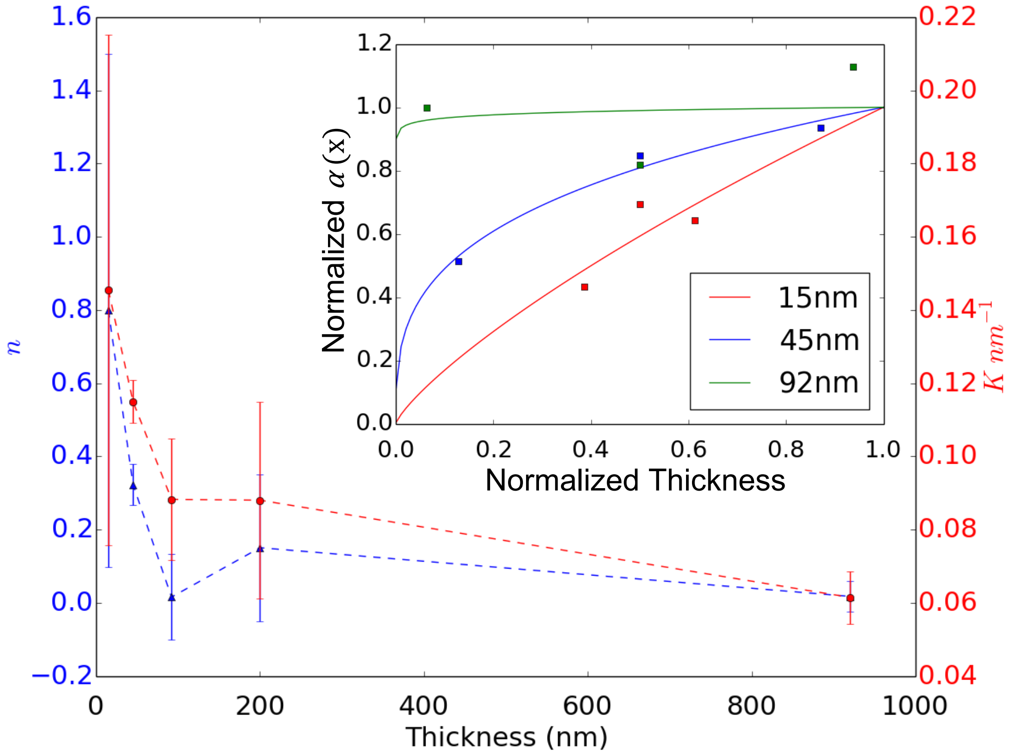

Figure 3.20: The Avrami exponent n (blue, left) and the rate constant K (nm^{-1}) (red, right) calculated for BHJ films of several different thicknesses. The dotted lines are guide to the eye. The error bars are calculated using the covariance matrix from the least squares fitting of the data to Eq.3.10. The inset shows normalized $\alpha(x)$ as a function of the normalized depth for BHJ films of three difference thicknesses (15nm, 45nm, and 92nm). The solid lines represent the best fit curves.

the rate of crystallization is lower as there is more volume further away from the air interface, from which the solvent has to escape. The Avrami exponent n has contributions from both nucleation and growth mechanism and can be written as $n = n_I + n_G$, where n_I relates to the nucleation and the n_G to the growth mechanism [86]. The nucleation factor, n_I, is expected to have values between 1, which refers to constant nucleation, and 0, which refers to quenched-in nuclei. Assuming that the growth-mechanism for films of all thicknesses is the same, we can then understand the change in the Avrami exponent as a function of thickness shown in Fig. 3.20 as change in the nucleation rate. For films in the thin-film confinement regime we get a value for the Avrami exponent to be close to 1 indicating constant nucleation. As the thickness of the BHJ film is increased, we approach a value of ~ 0.05 which can be explained by the quenching of the nucleation of polymer crystallization.

This rough model for polymer crystallization fits the data well and provides a likely explanation for the depth-dependence of polymer crystallization in a BHJ film. In an electronic device, the top of the film forms the interface to a metal contact that plays a crucial role in band alignment and recombination dynamics. The variation in crystallite size is particularly important as it changes the interfacial area between donor and acceptor materials. As excitons are dissociated at these interfaces, crystallite size variation significantly affects the charge transport and pathways for charge percolation. This in turn can cause changes in mobility and recombination, and therefore determine the performance of an electronic device [35, 52, 87–90].

These studies show that the confinement of polymer:fullerene BHJ films significantly alters the structural and crystallographic properties of the polymer. In this section we presented a crystallographic analysis of polymer:fullerene thin films of different thicknesses using GIWAXS, and determined that the crystallite size of the polymer in BHJs decreases and the molecular alignment of the polymer along the surface normal increases in the thin-film confinement regime. Furthermore, we studied the change in the crystallite size of the polymer within the depth of the film for different film thicknesses. We found that for thicknesses $\geq$100nm, the crystallite size on the top $\sim$ 11nm of the film is reduced compared to the crystallite size in the bottom and the bulk of the film. We provided a likely explanation for this by using the Avrami equation to model the kinetics of film formation. These results shed new light on the physics of bulk-heterojunction film formation, enabling material optimization and design for applications such as bulk heterojunction organic photovoltaics.

Chapter 4

Understanding Inhomogeneity in Inorganic Photovoltaics ($Cu(In_{1-x}Ga_x)Se_2$)

Key Findings:

- We find local compositional variation in CIGS with grain-to-grain copper fraction varying from 0.82-1.06
- Stoichiometric inhomgeneity between grains correlates with variation in structure where copper-rich grains tend to show chalcopyrite structure and copper-poor grains tend to show stannite-type structure
- Local (micron-scale) regions with a higher fraction of copper-rich grains shows enhanced interfacial recombination whereas local regions of copper-poor grains shows standard bulk limited recombination

4.1 Experimental Techniques

4.1.1 $Cu(In_{1-x}Ga_x)Se_2$ deposition

$Cu(In_{1-x}Ga_x)Se_2$ (CIGS) is a polycrystalline photovoltaic material composed of copper, indium, gallium, and selenium used in thin film devices. The value of x can vary from 1 - copper indium selenide - to 0 - copper gallium selenide. It has a chalcopyrite crystal structure and a bandgap varying from 1.0eV ($x = 0$) to 1.7 eV ($x = 1$). In this work, we will consistently use $x = 0.3$ which gives the highest recorded efficiencies. A standard CIGS device architecture is shown in Figure 4.1. The $Cu(In_{1-x}Ga_x)Se_2$ (CIGS) film was deposited using three-stage thermal co-evaporation from elemental sources of Cu, In, Ga, and Se onto a heated Mo-coated soda-lime glass substrate (SLG). The SLG used was purchased from Guardian (product name: Ecoguard Mo-1, 3.0mm thickness) consisting nominally ~15% Na_2O. The glass was coated with a Mo film by the glass manufacturer to a thickness of ~330nm (resistivity 15-22 $\mu\Omega$-cm). The CIGS/Mo film thickness typically measured to be 2.0μm, with Cu ratio (Cu/(In+Ga)) of 0.94, and Ga ratio (Ga/(Ga+In)) of 0.30 as measured by X-ray Fluorescence (XRF). XRF is used to measure copper and gallium ratios using a Ceres Technologies System SMX (Model # C06-01915-4002). The system was calibrated for CIGS films using the standard-adjusted FP (fundamental parameters) method. CIGS films of different compositions and thicknesses were measured using XRF. The film thickness was then measured using a stylus profilometer, and the film composition was measured using an inductively-coupled plasma (ICP) spectrophotometer with CIGS standard solutions. The XRF system was calibrated using these values. When these same CIGS layers are incorporated into standard (Mo/CIGS/CdS/iZnO/AZO) devices, the current-voltage curves yield power conversion efficiencies in the range of 15-18%.

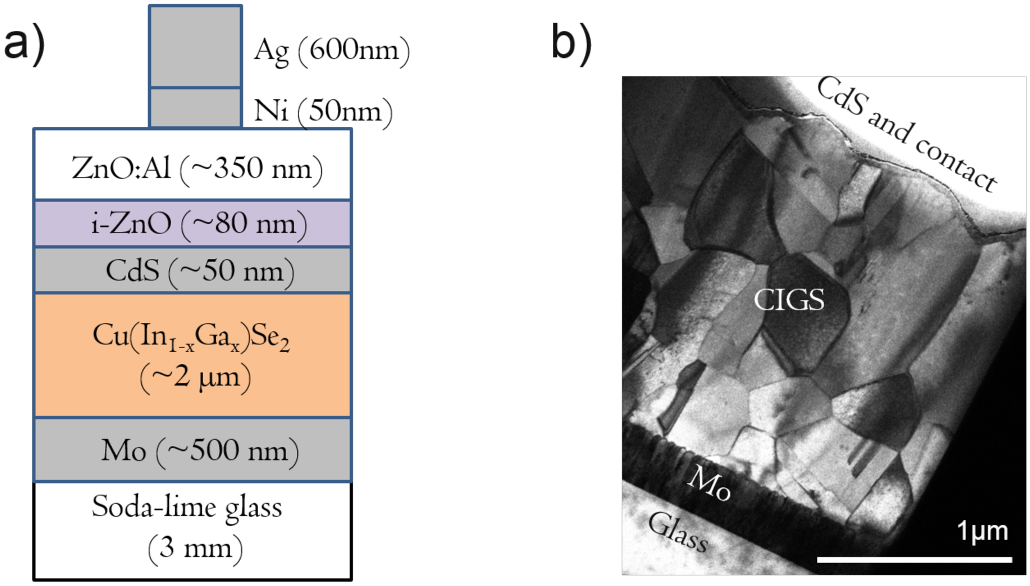

Figure 4.1: (a) Schematic of the CIGS device architecture. (b) A scanning electron microscopy image of a standard CIGS device.

4.1.2 Electron Microscopy/Energy Dispersive X-ray Spectroscopy /Focused Ion Beam

Scanning electron microscopy (SEM) is performed using the JEOL 7600F: Analytical High Resolution SEM. Energy dispersive x-ray spectroscopy (EDS) is performed at 20keV for 120s correcting for sample drift every 5s using site lock. All measurements were performed while the SEM was being cooled by liquid nitrogen.

Transmission electron microscopy (TEM) thin-film samples were made via a focused ion beam (FIB) using a FEI Helios Nanolab 600 Dualbeam (FIB/SEM) system employing a standard in-situ lift-out technique. Initial bulk milling was performed at 30 keV using a liquid metal gallium source. The specimen was subsequently cut free and transferred to a copper grid with a sharpened tungsten Omniprobe needle. Once attached to the TEM grid, the sample was thinned with progressively lower beam voltages down at to an approximate thickness of 50 nm with final milling performed at 2 keV. TEM images and diffraction patterns were acquired on a JEOL JEM2100F HRTEM operating at an accelerating voltage of 200 keV utilizing a 2K x 2K CCD camera.

4.2 $\mathrm{Cu(In_{1-x}Ga_{x})Se_2}$

State-of-the-art $\mathrm{Cu(In_{1-x}Ga_{x})Se_2}$ (CIGS) polycrystalline solar cells are still below their efficiency limit primarily due to recombination losses [91]. Inhomogeneity of the material leading to potential fluctuations is an important cause for recombination, however all previous measurements of recombination in polycrystalline CIGS focus on device areas that average over many hundreds to thousands (10^2 - 10^5) of micron-scale grains. In this chapter we explore variations in the composition and recombination dynamics at the length scale of a few grains. We use lithographically defined electrical contacts to measure the charge transport and current-voltage (IV) behavior as a function of temperature over micron-scale (few-grain) areas within a CIGS device in order to understand the grain-to-grain variation of recombination. We correlate these electrical measurements with energy dispersive X-ray spectroscopy (EDS) measurements of single-grain elemental composition, and aberration corrected transmission electron microscopy (TEM) with selected-area electron diffraction to ascertain the single-grain material structure. We find that local regions with a higher fraction of copper-rich grains (and primarily chalcopyrite structure) show enhanced interfacial recombination, whereas regions with a higher fraction of copper-poor grains (and a stannite-type structure) show bulk recombination limited behavior.

4.2.1 Nanoscale Electrical Measurements

Polycrystalline $Cu(In_{1-x}Ga_x)Se_2$ (CIGS) thin-film photovoltaics (PVs) have reached the highest efficiencies of all thin film photovoltaic technologies and have the potential to achieve a lower levelized cost of electricity than silicon. To realize this potential, the power conversion efficiency (η) of CIGS must be increased from the current state-of-the-art value of 21.7% [92] towards the single-junction Shockley-Queisser (SQ) limit of 33% [93]. Previous measurements on record devices have shown that their efficiency is limited by optical/collection losses, and recombination losses [91]. Although mitigating optical and collection losses could improve the device efficiency by an absolute 3%, the primary losses in state-of-the-art CIGS solar cells are due to recombination (7% absolute). The dominant source of this recombination is the presence of local spatial electrostatic potential fluctuations caused by inhomogeneities such as charged defects, grain boundaries, and dislocations [91]. Previous work on understanding these potential fluctuations has typically focused on charged defects at grain boundaries [94–97]. However theoretical and experimental studies, though not entirely conclusive, have shown potentially beneficial grain boundaries in CIGS [98–100]. Here we quantify the variation in Cu concentration from grain to grain, and conclusively correlate the measured Cu fraction to the dominant charge recombination mechanism in the local region near these grains. This spatial correlation between Cu content and recombination is most likely due to the electrostatic potential fluctuations caused by the spatially varying charged defect chemistry resulting from the grain-to-grain variation in Cu concentration [91].

Solar cells made with non-stoichiometric Cu-poor CIGS are known to have higher power-conversion efficiencies than cells made with stoichiometric and non-stoichiometric Cu-rich CIGS, even though stoichiometric and non-stoichiometric Cu-rich CIGS contain lower defect concentrations [101]. In order to make a stoichiometric chalcopyrite CIGS structure, the material is grown under copper excess where the leftover copper forms a copper selenide secondary phase. It has been shown that even after the removal of the excess CuSe on the surface using a KCN etch, the devices made with these absorbers are dominated by interfacial recombination [102]. Absorbers that use an overall copper poor composition (current state-of-the-art) are generally believed to be limited by SRH recombination in the space charge region (bulk of the absorber)[103]. However micron-scale copper rich regions within the absorber layer of a device that is grown overall copper poor could potentially increase interfacial recombination. Such absorbers made overall Cu-poor have been shown to have a surface layer that is even more Cu-poor than the bulk [104]. This surface layer develops naturally and has a higher band gap than the bulk preventing interfacial recombination by inhibiting holes from reaching the interface [105–112]. Although no evidence of any structural phase associated with the copper poor surface layer in working CIGS devices exists [113–118], studies have shown that specially grown copper poor absorber layers have a non-stoichiometric structure [105, 108, 109, 119–126]. Due to the low formation energies of different non-stoichiometric phases [127, 128], even small compositional variations at the nanoscale can cause structural and phase variations [129].

In this chapter, we systematically study charge transport and recombination within a CIGS device on the scale of a few grains, and correlate this behavior with the composition and structural variation among individual grains. We use CIGS samples with a large-area average composition (similar to those currently giving the highest efficiencies) of Ga/(In+Ga)= 0.297 and a Cu/(In+Ga) = 0.957 (referred to as the “Cu fraction”), as measured using X-ray fluorescence. These same samples are measured to have a power conversion efficiency of 15-18% when made into complete CIGS solar cells. Using temperature-dependent IV measurements on lithographically defined contacts that probe only a few grains, we extract the potential barrier height at the p-n CIGS-CdS heterojunction. We find that regions with a high number of copper rich grains show a lower potential barrier (0.03eV) than regions with more copper poor grains (potential barrier of 0.49eV). The lowered potential barrier at the interface causes enhanced interfacial recombination. The recombination is understood to be enhanced by tunneling, as evidenced by the temperature-dependent diode quality factor. In order to link the high-Cu (and low-Cu as a reference) copper region to a specific phase or structure, we perform EDS and aberration corrected TEM with electron diffraction on individual grains.

4.2.2 Fabrication of Devices

The devices start with a partially completed standard CIGS solar cell (see Fig. 4.2: 1) CIGS (2.4 μm)/molybdenum (Mo, 300 nm)/soda lime glass (SLG, 3mm). A cadmium sulfide (CdS, 50-100nm) layer is deposited using chemical bath deposition (CBD). To make temperature-dependent IV measurements on individual CIGS grains we deposit 375nm of SiO_2 via plasma-enhanced chemical vapor deposition (PECVD) at 160C at 1.6 nm/s rate, as a resistive layer on the CdS to prevent current flow through the absorber from the contact pads to the back Mo anode (Fig. 4.2: 3). 3x4 μm^2 regions were patterned on the PECVD SiO2 using electron-beam lithography technique (E-beam).

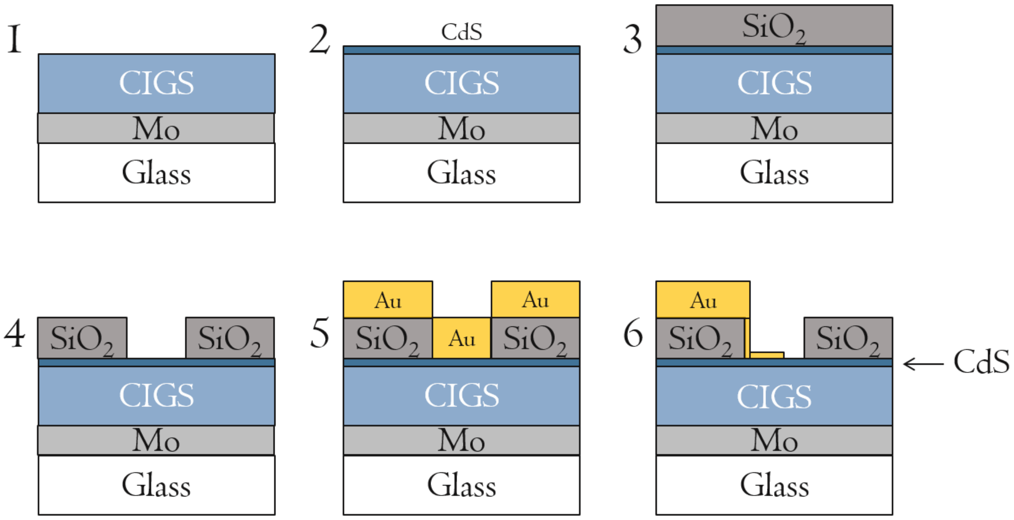

Figure 4.2: A step-by-step outline of the fabrication of devices. 1: Partial CIGS/Mo/SLG device, 2: Cadmium sulfide layer deposited using CBD, 3: SiO2 layer deposited using PECVD, 4: SiO2 layer etched away using FDRIE, 5: Gold (Au) contact deposition using e-beam evaporation, 6: Contact lift-off using electron beam lithography.

E-beam was performed using the JEOL JBX-6300FS lithography system on E-beam resist positive resist ZEP520A (spun at 3000 rpm for 45s annealed at 180C for 3 minutes) by exposing with a dose of 400 μC/cm^2 at 100 keV and developed with amylacetate for 90 sec and washed off with isopropanol for 45s. At the same time, alignment markers are also placed which are used as fiducial marks for the deposition of gold contacts.

The SiO_2 is etched into using deep reactive ion etching (DRIE) using a mixture of (CHF3 and Ar) and localized regions of the CdS surface are exposed (Fig. 4.2: 4). After etching, e-beam lithography is again used to align on the markers and put down the contact pattern. The electrical contacts (100nm of gold/3 nm of chromium) are deposited using electron beam evaporation. The resist is lifted off overnight using N-Methyl-2-pyrrolidone at 80°C. The gold contacts are $\sim$1μm long and 100nm wide and extend into the region where the CdS surface is exposed, providing a contact to the CdS/CIGS interface over a small and controlled area (Fig. 4.2: 6).

Figure 4.3 a) shows a schematic of the cross section of the sample and Figure 4.3 b) shows a scanning electron microscopy (SEM) image of the top view of sample used in the measurement. The gold contacts can be seen extending over the SiO_2 layer into the etched region where they make contact

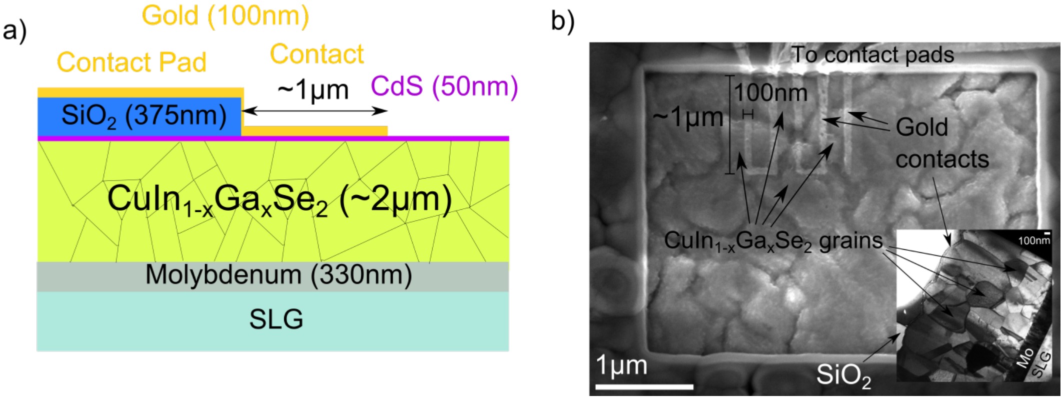

Figure 4.3: a) Schematic of the cross section of a device used for low temperature current voltage measurements. The top contact is $\sim 1\mu$m long and 100nm in width with a thickness of $\sim$100nm. The schematic also shows the CIGS grains showing that each contact is affected by $\sim$ 8 CIGS grains. b) Scanning electron microscopy image of the top view of the electronic devices showing the SiO$_2$ mask and opening to the bare CdS/CIGS material, as well as each gold contact individually contacting 2-3 grains at the surface of the absorber material. Inset shows a cross section of the sample with the SiO$_2$, the contacts, the CIGS grains, the back molybdenum contact, and the soda-lime glass (SLG) substrate.

to the CdS surface. The CIGS grains are easily visible in Figure 4.3 b), and we see that each gold finger laterally contacts only 2-3 grains at the CIGS/CdS surface.

4.2.3 Recombination Mechanisms

We performed dark low-temperature IV measurements using these small-area gold contacts to extract saturation current densities and diode quality factors as a function of temperature. Low temperature current-voltage measurements were performed using the MMR technologies variable temperature micro-probe system. The temperature is varied from 83-300K in steps of 10K using a micro miniature refrigerator that cools the sample using the Joule-Thompson expansion of high-pressured nitrogen gas (chamber pressure <1mTorr). At each temperature an IV curve is extracted using a Kiethley 2600 source meter.

Although the overall copper composition of the CIGS absorber layer is copper poor when averaged over the mm-length scale (Cu/(In+Ga) = 0.957), the investigation of single grains using EDS reveals grain-to-grain variation in the Cu fraction, with the single-grain Cu fraction ranging from 0.821 to

1.061. Figure 4.4 a) shows a band diagram of the CdS/CIGS interface. The predominant recombination paths are shown as: (1) interfacial and (2) bulk. It has been seen in the past that devices grown with an overall (large-area average) Cu-poor absorber are primarily limited by bulk recombination [103, 130].

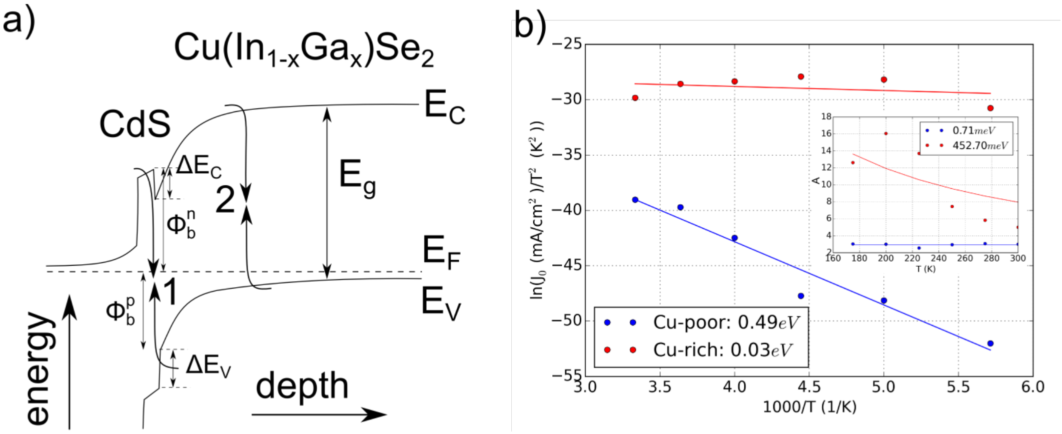

Figure 4.4: a) Schematic of the band alignment between n-type CdS buffer and CIGS chalcopyrite absorber material showing major recombination paths at the interface (1) and in the bulk (2) where E_C is the conduction band, E_V is the valence band, E_g is the band gap, E_F is the Fermi energy and Φ_b^n indicates the potential barrier at the heterointerface. b) The natural log (ln) of the saturation current density (in units of mA/cm^2) divided by the temperature (in Kelvin) squared as a function of the inverse temperature where the extracted barrier height of the heterointerface, Φ_b^n, for the average copper poor region and the higher-than-average (HTA) Cu region is shown. Inset shows the diode quality factor, A, as a function temperature fit to Eq. 4.3 giving the characteristic tunneling energy, E_{00}, as shown in the legend.

Using the saturation current density, we can extract information about the potential barrier, Φ_b^n, at the CdS/CIGS heterointerface in order to understand potential variations at the interface. The barrier height at the interface is given by $\Phi_b^n = E_C - E_F$ as shown in Figure 4.4a). Assuming the major conduction mechanism across the barrier is thermionic emission, the electron current density across the conduction band spike is given by

$$J_n \approx J_0 e^{qV/kT} \tag{4.1}$$

$$J_0 = A^* T^2 e^{(-\Phi_b^n)/kT} \tag{4.2}$$

where J_0 is the reverse saturation current density, and A^* is the Richardson coefficient [131]. We can extract the potential barrier height, Φ_b^n, by fitting a straight line through $ln(J_0/T^2)$ against $1000/T$ as shown in Figure 4.4 b).

Figure 4.4 b) compares two regions from the same CIGS sample (laterally <5mm apart). From the region showing a higher-than-average (HTA) Cu fraction (red), we extract a barrier height of 0.03eV which is significantly lower than the barrier height extracted from the average copper region (blue) at 0.49eV. This lowered potential barrier height at the interface in the case of HTA Cu regions can significantly increase the interfacial recombination. The temperature dependent diode quality factor (shown as inset in Figure 4.4 b) in the HTA Cu region confirms that the lowered potential barrier increases tunneling enhanced interfacial recombination. The diode quality factor, A, in the case of tunneling enhanced interfacial recombination is given by

$$A = 1/\alpha \frac{E_{00}}{kT} coth(\frac{E_{00}}{kT}) \tag{4.3}$$

where E_{00} is the characteristic tunneling energy, and the quantity α is related to the band bending at the interface. The characteristic tunneling energy, E_{00}, increases from 0.71meV for the standard copper poor region to 452.7meV in the HTA Cu region indicating an enhancement of tunneling due to the reduced potential barrier height at the interface.

4.2.4 Grain-to-Grain Compositional and Structural Variation

In order to prepare these selected (average and HTA Cu fraction) regions for study using TEM electron diffraction and EDS, we used a focused ion beam with a gallium source. Bulk milling was performed at 30 keV until the sample could be removed and attached to a TEM grid after which the sample was thinned down at 2keV until the sample was the size of the contact as shown in Figure 4.3 b). The cross sectional images of a sample from a Cu-rich region with enhanced interfacial recombination taken using a scanning electron microscope (SEM) with a transmission detector at 30keV is shown in Figure 4.5 a).

As a reference, Fig. 4.5 b) shows a cross sectional image of a standard copper poor sample which is known to be limited by bulk recombination. At each individual grain in Figure 4.5 a) and b), EDS was performed at 20keV and data was collected for 120s. As the sample is only ∼100nm thick, the probe volume of the sample at this energy is 100nm deep with a lateral radius

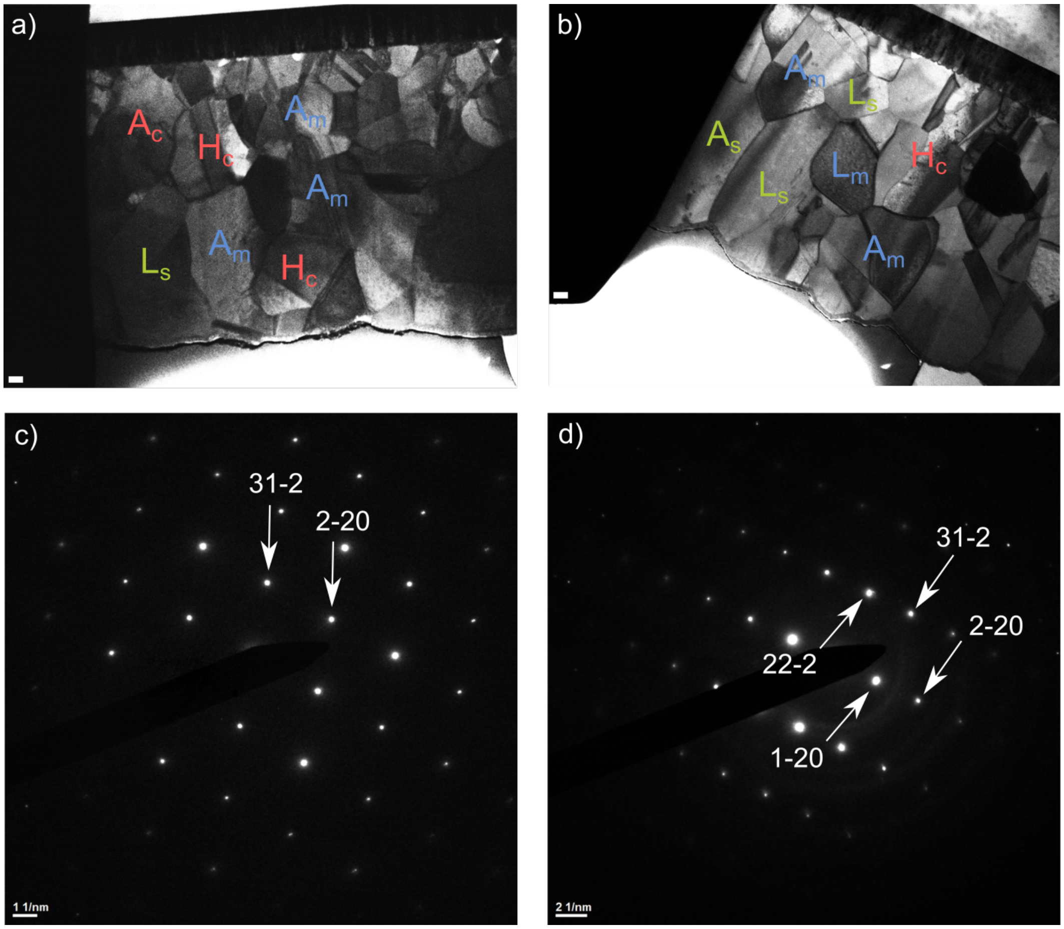

Figure 4.5: Scanning electron microscopy images with a transmission detector showing the grains from devices with a) enhanced interfacial and b) bulk recombination. Using energy dispersive X-ray spectroscopy at each individual grain the copper composition is extracted and the grains are labeled as “A” for average copper composition, “H” for high copper, and “L” for low copper grains. The subscript and color identifies the structure within the specific grain as stannite (green, and subscript “s”), chalcopyrite (red, and subscript “c”) or a mixed phase (blue, and subscript “m” where reflections allowed in both stannite and chalcopyrite structures are seen. The scale bar is equivalent to 100nm. Electron diffraction patterns of c) chalcopyrite structure (I-42d) and b) the stannite structure (I-42m) along the [112] zone axis is shown. In the copper poor stannite phase, additional spots at (1-20) and (22-2) appear which are forbidden in the chalcopyrite structure.

of 100nm. By performing EDS on pure copper tape, a quantitative correction was done for the EDS signal from the tape alone. Figure 4.5 labels the grains with the results obtained using EDS measurements, showing average copper as "A" (defined as the large-area average: Cu fraction = 0.957), high (larger than one standard deviation from the mean) copper as "H", and low (smaller than one standard deviation from the mean) copper as "L". Assuming the average copper ratio of all grains measured was equal to the values measured using X-ray fluorescence (0.957) from the entire sample, we measure a Cu fraction from the low copper grains to be in the range of 0.82-0.88, and from the high-Cu grains to be in the range of 1.05-1.06. The sample showing enhanced interfacial recombination (Fig. 4.5 a) shows a lesser number of Cu-poor grains, and a larger number of Cu-rich grains than the sample limited primarily by bulk recombination (Fig. 4.5 b).

In order to detect any structural changes due to these compositional grain-to-grain variations, electron diffraction with transmission electron microscopy was performed on each labeled grain in Figure 4.5 a) and b). Absorber layers that are grown copper rich generally show the -chalcopyrite structure with space group I-42d. Figure 4.5 c) shows the diffraction pattern from a copper rich (Cu/[Ga+In] >1) grain along zone axis [112] which agrees well with a stoichiometric chalcopyrite structure. Figure 4.6 c) shows a unit cell with this structure and Figure 4.6 a) shows a simulated electron diffraction image [132] which agrees well with experimental data.

Copper poor grains show different diffraction patterns, with additional peaks at forbidden locations for the I-42d space group due to the existence condition 2h+l = 4n. This is shown in Figure 4.5 d) where extra peaks can be seen at (22-2) and (1-20). These can be explained by a stannite type structure with space group I-42m which has been reported previously in literature for Cu- poor compounds [119–125]. Furthermore, Figure 4.6 d) shows a unit cell with this structure and Figure 4.6 b) shows a simulated electron diffraction pattern [132] which agrees well with experimental data.

Grains with a copper composition close to the average of the sample (which is overall copper poor, Cu/(Ga+In) $\sim$ 0.957), also show a mixed diffraction pattern where both the chalcopyrite phase and the stannite phase can be seen. The defect stannite phase cannot be represented by a simple unit cell however the average structure is known to belong to the space group I-42m. The primary difference between the stoichiometric chalcopyrite phase and the defect stannite phase originates from the segregation of gallium (Ga) and indium (In) atoms on separate atomic planes as Ga and In share the same crystallographic site in the I-42d structure, whereas in the I-42m structure Ga and Cu share the same site and In is segregated to a different site.

In this chapter we use lithographically defined contacts to measure recombi-

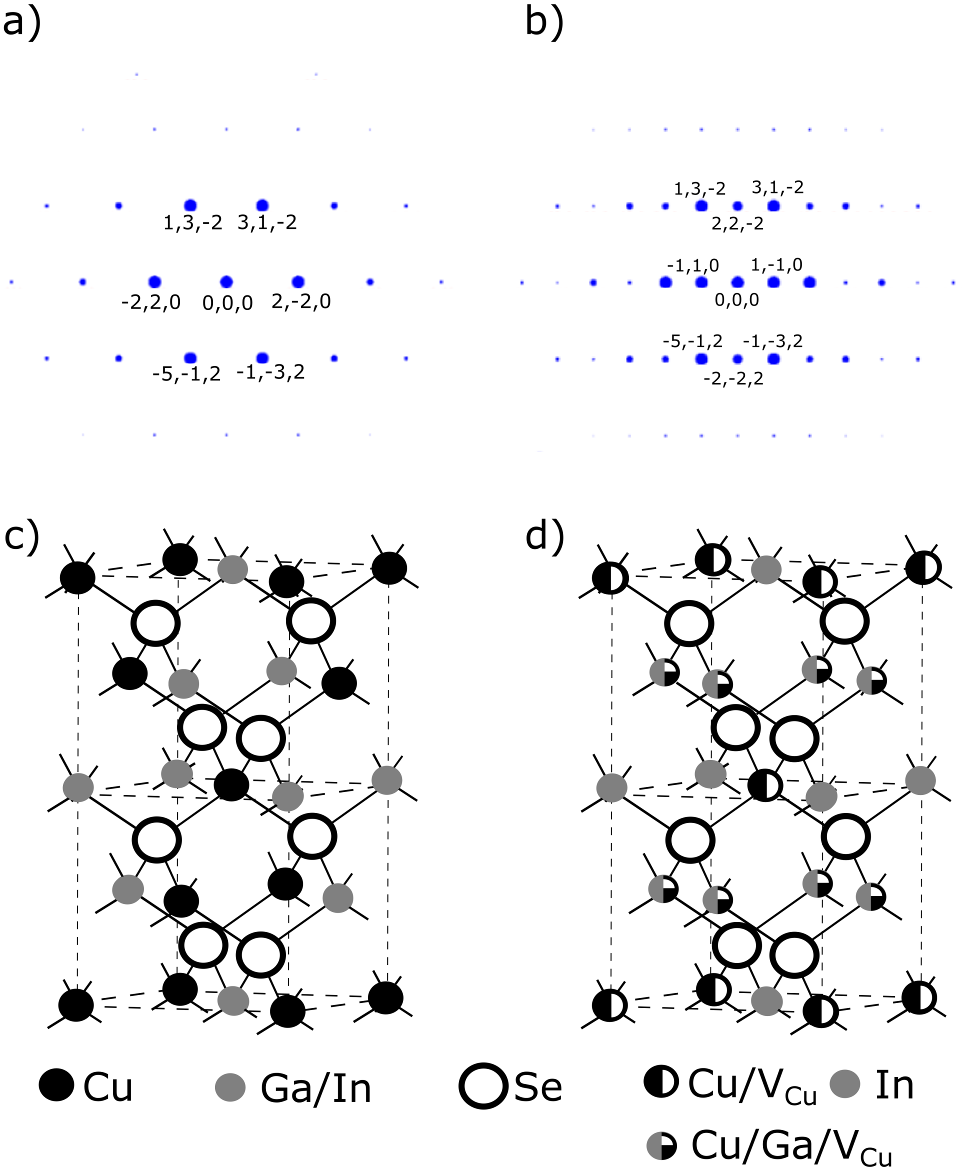

Figure 4.6: Simulated electron diffraction patterns for the a) chalcopyrite structure (I-42d) and b) the stannite structure (I-42m) along the [112] zone axis is shown. In the copper poor stannite phase, additional spots at (1-20) and (22-2) appear which are forbidden in the chalcopyrite structure. Unit cells for CIGS in (c) the chalcopyrite and (d) the stannite crystal structure are shown as well.

nation mechanisms with few-grain resolution in polycrystalline CIGS solar cell, and identify the main driver for an enhancement in interfacial recombination as due to spatial variations in the electrostatic potential due to grain-to-grain variation in in the Cu fraction. While the large-area average Cu fraction of the device is Cu poor (0.957), specific grains exhibit Cu fractions in a wide range, from 0.82 - 1.05. Grains with higher Cu fraction show an increase in recombination due to tunneling enhanced interfacial recombination. These regions were isolated and prepared using a focused ion beam for cross sectional EDS and electron diffraction on each individual grain. The regions with enhanced interfacial recombination showed a higher proportion of copper rich grains and a lower number of copper poor grains than the regions dominated by bulk recombination. Electron diffraction showed that the copper poor grains with a copper ratio of $\sim$ 0.82-0.88 typically show a stannite type structure, whereas copper rich grains showed a chalcopyrite structure with average copper grains often showing a mixed phase. These measurements demonstrate the usefulness of our technique by directly quantifying the source of recombination in CIGS solar cells, and point the way forward toward higher efficiency CIGS devices.

Chapter 5

Novel Techniques for Measuring Inhomogeneity

The understanding of inhomogeneities often requires novel techniques to enable measurements at the length scales of the expected variations. This chapter will outline some specific techniques.

Key Findings:

- We describe a novel charge-extraction technique, micron-scale charge extraction by linearly increasing voltage (μCELIV), which enables simultaneous spatially resolved measurements of charge carrier mobility and photocurrent in thin-film photovoltaic devices with micron-scale resolution
- We introduce a novel hyperspectral laser beam induced current system using a supercontinuum laser (400nm - 1200nm) with diffracted limited spot size allowing the extraction of performance metrics with high lateral and depth resolution, and the simultaneous correlation with material deformations while the device is at operating conditions

5.1 Mobility at Micron-scale Resolution

In this section, we will outline a novel charge-extraction technique, micron-scale charge extraction by linearly increasing voltage (μCELIV), which enables simultaneous spatially resolved measurements of charge carrier mobility and photocurrent in thin-film photovoltaic devices with micron-scale resolution. An intensity-modulated laser with beam diameter near the optical diffraction limit is scanned over the device while a linear voltage ramp in reverse bias is applied at each position of illumination. We calculate the majority carrier mobility, photocurrent, and number of photogenerated charge carriers from the resulting current transient. We demonstrated this technique on an organic photovoltaic device, but it is applicable to a wide range of photovoltaic materials.

5.1.1 μ-Charge Extraction by Linearly Increasing Current

The measurement and control of charge-transport properties is critical to the improvement of organic optoelectronic devices. The majority carrier mobility in organic photovoltaics (OPVs) has been measured using: IV curves in the space charge limited current (SCLC) regime [133], field effect transistor (FET) method [84, 134], and time of flight (ToF) method [134–136]. However, mobility measured with SCLC and FET are at saturated charge transport and high external bias, respectively, and do not represent normal operating conditions in OPVs [137–140], while ToF measurements require extremely high optical density films. As a result, CELIV (Charge Extraction by Linearly Increasing Voltage) [141], and photo-CELIV [142, 143] have become popular methods for measuring the mobility and lifetime of majority charge carriers in OPVs.

In CELIV, equilibrium majority charge carriers are extracted under a linear voltage ramp in reverse bias with no illumination, thereby depleting the junction while blocking carrier injection. The resulting current transient is used to calculate the majority charge-carrier mobility and charge density. In photo-CELIV, charge carriers are generated by an ultra-short laser pulse and then extracted under a linear voltage ramp after a time delay (t_{del}). The charge carrier mobility and lifetime can be obtained from photo-CELIV using the current transient and by calculating the change in the photocarrier density as a function of t_{del}. CELIV and photo-CELIV have each been used to measure the mobility and lifetime of many different photovoltaic (PV) systems, including organic PVs [143–147] and hydrogenated microcrystalline silicon (μc-Si:H) [141, 142, 148, 149]. The morphology and spatial variations within donor/acceptor bulk heterojunction (BHJ) blends used in OPVs are critical to OPV performance, especially in moving from lab-scale to industrial-scale devices. The previously identified morphology-performance relationships were inferred indirectly from different measurements often on different devices. However, the morphology is highly sensitive to processing conditions such as choice of solvent, drying time [29], thermal treatments, and solvent additives [37, 38]. Variations in processing conditions can alter local morphology, resulting in significant spatial variations in performance. For these reasons, the ability to measure mobility, locally and commensurately with performance metrics, is critical to the understanding of morphological spatial inhomogeneities on device performance. In this chapter we demonstrate a spatially-resolved CELIV technique, referred to as μCELIV (micron-scale charge extraction by linearly increasing voltage), and use μCELIV to simultaneously measure the mobility and photocurrent of a polymer-fullerene blend, poly(3-hexylthiophene) (P3HT) and [6,6]-phenyl-C61-butyric acid methylester (PCBM) solar cell with <5 μm spatial resolution. The details of device preparation can be found in Section 3.1. A 13mg/ml P3HT:PCBM solution was spin-coated at 700rpm to achieve a thickness of 149nm (measured using a Veeco Dektak 150 in a class 1000 cleanroom). The top aluminum contact was deposited by physical vapor deposition (PVD) using a shadow mask to define the active area (0.105cm^2), and then thermally annealed at 150°C for 10 minutes in a vacuum oven for post processing.

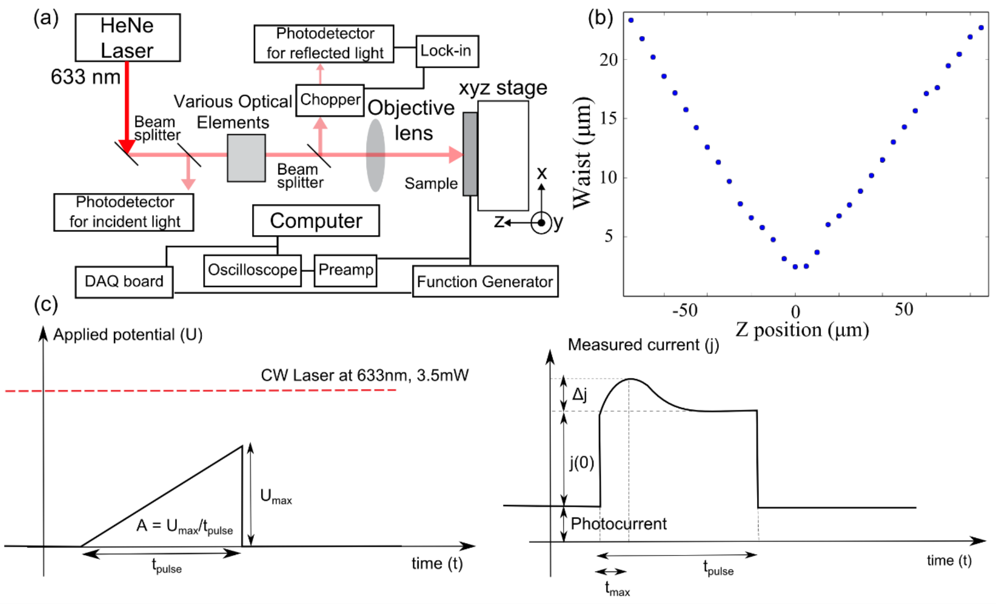

Figure 5.1: (a) Schematic of the micro-CELIV experimental setup. HeNe Laser = Thorlabs HNL150L. (b) Beam radius versus z-position. Beam waist (radius) = 2.5μm. (c) Schematic of the linear voltage ramp (left) and the resulting transient current (right). CW laser is on throughout the measurement.

A HeNe laser is expanded in diameter by 4x using Thorlabs BE04R and then focused onto the sample using an objective lens (Newport reflective objective, Model 50105-02, 15x magnification N.A. = 0.4). The sample is placed on an x-y-z stage (x and y: Newport GTS150, z: Newport GTS30V) with accuracy of ±1μm over 150mm in the x and y in-plane directions, and ±0.75μm over 30mm in the z-direction. The beam reflected from the sample is aligned onto the incident beam path and picked off using a Thorlabs pellicle beamsplitter, BP208. The reflected beam is chopped (Thorlabs, MC2000) at a frequency of 307Hz and focused onto a photodiode. The photodiode output is fed to an SRS DSP lock-in amplifier (SR830), with the chopper connected to the lock-in reference. An SRS DS345 function generator is used to generate a 3.0Vpk-pk, 20 kHz voltage ramp in reverse bias that sweeps the voltage from 0V to 3.0V in 50μs. The transient current is collected through a Femto DLPCA-200 fast transimpedance amplifier at 102V/A gain connected to a 200MHz oscilloscope (Tektronix).

5.1.2 Mobility Variation in OPVs

The OPV device was placed on the x-y-z stage and the laser was focused onto the device, illuminating it from the glass side with the aluminum contact facing down (see Fig. 5.1(a) for schematic). The z position of the stage is set such that the beam waist is in the center of the absorber layer. At each x-y position (increments of 100μm in Fig. 5.3, 25μm in Fig. 5.4), a focused 633nm laser spot with power 3.5mW and radius of 2.5μm (Fig. 5.1(b)) continuously illuminates the device during the measurement. The frequency and the amplitude of the voltage ramp are tuned until we observe the characteristic transient current curve (see Fig. 5.1(c)), which occurs when all excess photogenerated carriers (with respect to the equilibrium charges) can be extracted by the potential-induced field. At time t = 0, a linearly increasing potential is applied to the device with a ramp rate $A = U_{max}/t_{pulse}(U_{max} = -3.0V, t_{pulse} = 50\mu s)$ in reverse bias, where the depletion width of the junction, and therefore the capacitance of the device, stays relatively constant. For a material with no free charge carriers, the current would look rectangular with a height, j_0, given by the geometric capacitance of the diode. We calculate the geometric capacitance from j_0 to be 5.27nF, in agreement with literature values for P3HT:PCBM devices[150]. Due to the linear increase in the electric field, all free charge carriers (thermal and photogenerated) begin to move and are extracted at the electrodes, resulting in an additional peak in the current, j_{max}, at a time t_{max}. The time t_{max} gives information about mobility, μ, of the extracted charges. The current transient can be calculated using a combination of the continuity, current, and Poisson equations. The equations can be solved using a numerical model [144, 147, 151], and for a device comprised of π-conjugated polymers with uniformly generated charge carriers, the mobility is given by the following [147]:

$$\mu = \frac{2d^2}{3At_{max}^2(1+0.36\Delta j/j_0)}, \tag{5.1}$$

where $\Delta j = j_{max} - j_0$. Although other numerical solutions exist for devices with very significant values of $(j_{max} - j_0)/j_0$ where the photogenerated charge is larger than the amount of charge on the electrode, for our devices the photogenerated charge is approximately equal to the electrode charge and $(j_{max} - j_0)/j_0 << 1$, and therefore Eq. 5.1 provides an accurate description [144, 151]. To apply the technique to other material systems the appropriate equation for the calculation of mobility must be used based on values for j_{max} and j_0.

The photo-carrier mobility obtained from μCELIV when the device is illuminated is higher than dark CELIV measurements, highlighting the effect of photo-carrier density on mobility. The dependence of mobility on charge-density in organic semiconductors in the low-charge density regime of $n = 10^{14} - 10^{17} cm^3$ has been shown to follow a power law given by the equation [152]:

$$\mu(n) \propto n^{\delta}, \tag{5.2}$$

where $\delta = 0.35$. This is due to the decay dynamics in the OPV being dominated by bimolecular recombination, and the bimolecular recombination coefficient k being strongly charge-density dependent, increasingly almost linearly with increasing n [153].

In order to make a spatial map of mobility that allows for meaningful comparison between different lateral positions, we must account for the spatial variation in photo-carrier density due to reflection and thickness variations. The μCELIV measurement was performed at various incident optical intensities (including in the dark) and the mobility was calculated using Eq. 5.1. Fig. 5.2(a) shows that t_{max} decreases as the optical intensity increases (the dark current transient curve with no optical excitation is also shown). Although the steady-state photocurrent (offset of baseline current) also increases as a function of optical intensity, all curves shown in Fig. 5.2(a) are normalized by subtracting the steady-state photocurrent offset from the entire current transient curve. Although CELIV assumes a perfectly blocking junction in reverse bias, realistic devices can have a small leakage current since the extracted current transient for the illuminated device does not reach the capacitive response at the end of the 50μs voltage pulse. In order to make sure that the number

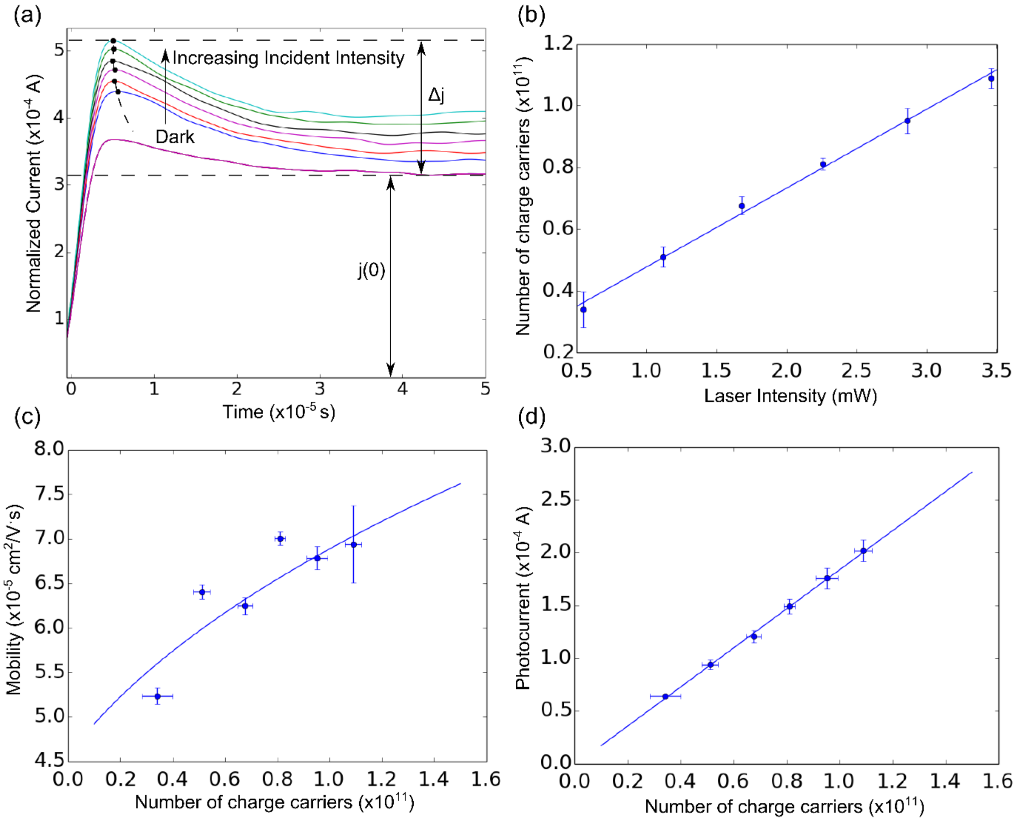

Figure 5.2: (a) μCELIV curves extracted at different laser intensities, on a single position. As the laser intensity is increased, t_{max} decreases and the mobility increases. The transient current curves are normalized by subtracting the steady-state photocurrent offset shown in Fig. 5.1(c) from the entire current transient curve. The current transient curve from the device for no laser illumination is also shown labelled as Dark. (b) The number of photogenerated charge carriers, calculated by subtracting the integrated area under the dark current-response curve from the integrated area under the illuminated current-response curve, plotted against laser intensity. (c) Mobility, calculated via Eq. 5.1 versus number of photogenerated charge carriers. (d) Photocurrent as a function of the number of charge carriers. Error bars equal standard deviation of values from multiple positions on the same device.

of photogenerated charge carriers increases with incident light intensity, Fig. 5.2(b) shows the linear relationship between the number of charge carriers and the incident light intensity, demonstrating that the device is not saturated. The number of photogenerated charge carriers is calculated using the area under the transient current curve for the illuminated device, and subtracting it

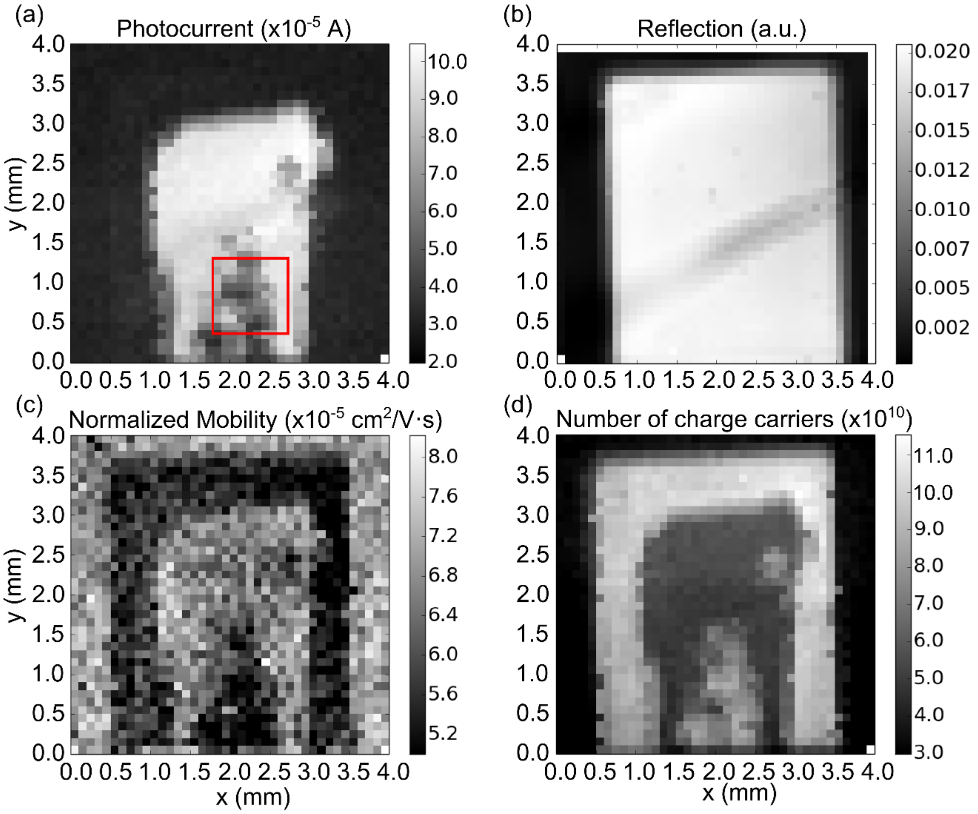

Figure 5.3: (a) Photocurrent map extracted using the baseline shift in the measured current transient shown in Fig. 5.1(c). (b) Reflection map measured using the reflected laser sampled from the beam path. (c) Normalized photocarrier mobility calculated at each illuminated spatial position on the device using Eq. 5.1. The mobility normalization is performed separately for each spatial position by subtracting, from the measured mobility, the mobility offset due to the number of photogenerated charge carriers. The mobility offset for a given spatial position is calculated by subtracting the zero-charge-carrier mobility in Fig. 5.2(c) (4.56x10^{-5}cm$^2/Vs$) from the mobility value in Fig. 5.2(c) for which the corresponding number of charge carriers (x-axis in Fig. 5.2(c)) is equal to the measured number of charge carriers shown in Fig. 5.3(d) for the given spatial location. (d) Number of photogenerated charge carriers at each spatial position, calculated by subtracting the integrated area under the dark current-response curve from the integrated area under the illuminated current-response curve after normalizing for the photocurrent. Pixel spacing is 100μm for all measurements.

from the current transient of the dark device. Fig. 5.2(c) plots the mobility versus the number of photogenerated charge carriers. The error bars represent the standard deviation of multiple measurements from different spots of illumination on the same device. This data is fitted to Eq. 5.2, giving the best fit line shown in Fig. 5.2(c). As an additional saturation check, we also extract the photocurrent from the transient using the offset from the baseline and verify that photocurrent versus number of photogenerated charge carriers is linear (Fig. 5.2(d)).

2D maps with 100μm x-y spacing of the photocurrent, reflection, mobility, and the number of photo-generated charge carriers as measured with μCELIV, are shown in Figs. 5.3(a)-(d). The high-reflection areas from the aluminum contact in Fig. 5.3(b) show the active area of the device. The photocurrent map in Fig. 5.3(a) shows degradation on the edges of the device due to exposure to air after fabrication. Regions of high photocurrent can be identified between x = 1.0mm to x = 3.0mm and y = 1.5mm to y = 3.0mm; regions of lower performance include x = 2.25mm, y = 1.0mm. A finer scan with 25μm x-y spacing (Fig. 5.4) is performed in the region highlighted by the red square.

Fig. 5.3(c) shows the mobility at each spatial location on the device calculated using Eq. 5.1 and normalized using the data in Figs. 5.2(c) and 5.3(d), to represent the mobility value at each location in the limit of vanishing photogenerated charge-carrier density. This normalization ensures that Fig. 5.3(c) shows mobility variations due to fundamental material inhomogeneities and not simply due to reflection or thickness variations. From Fig. 5.3, we see that the mobility is strongly correlated with the photocurrent, and that the air-induced degradation around the edges is remarkably clear in the mobility map. In the regions of highest photocurrent, the mobility reaches its maximum value of 7.2x10^{-5} to 7.6x10^{-5}cm$^2/Vs$. This ability to map the spatial variation of mobility (ultimately only limited by the laser diffraction limit of a few microns) cannot be probed with any other existing techniques - techniques that measure the bulk mobility lose this information about the micron-scale variation that is critical to understanding and overcoming device limitations due to spatial inhomogeneities.

Comparing Fig. 5.3(c) and 5.3(d) more closely, we see that the areas of higher normalized mobility have a lower number of photogenerated carriers, and the degraded areas of lower mobility have a higher number of carriers. This observation of photogenerated carrier increase due to degradation agrees well with previous studies [154], and is due to an increase in electron traps due to oxygen doping, resulting in an increase in the number of holes [155]. A finer scan (25 μm x-y spacing) of the area with lower photocurrent (red square in Fig. 5.3(a)), is shown in Figs. 5.4(a)-(d). We observe that the correlations

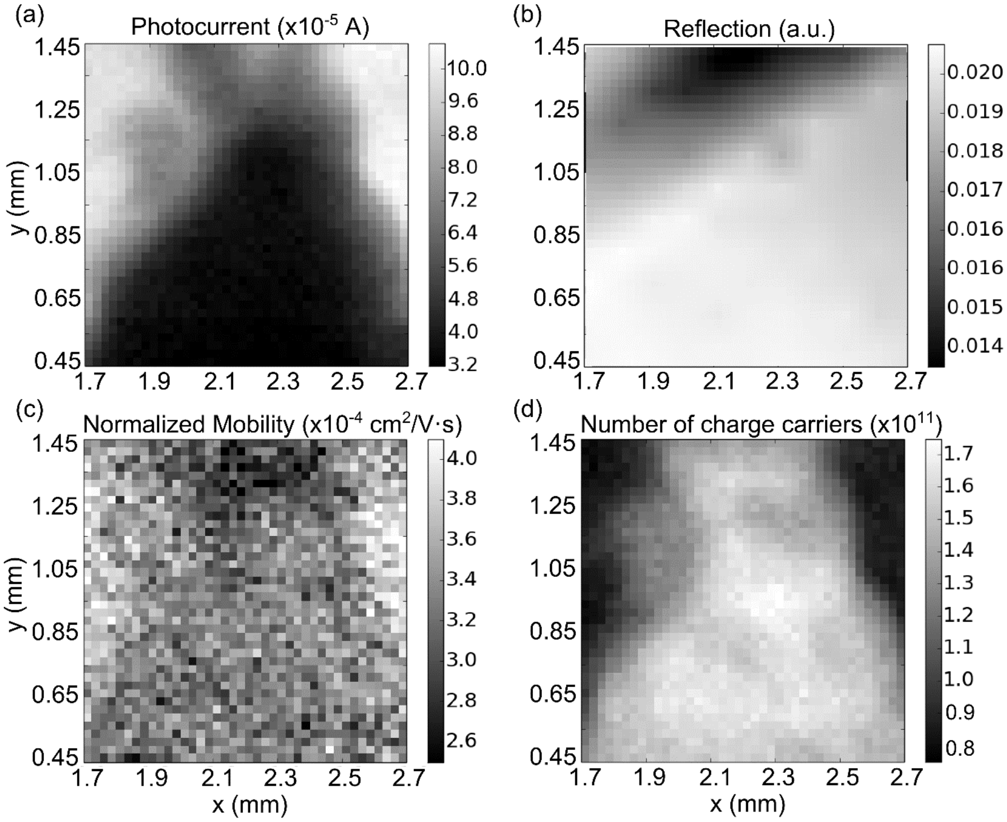

Figure 5.4: A fine scan with steps of 25μm is taken in the area shown by the red square in Fig. 5.3. (a) Photocurrent, (b) Reflection, (c) Normalized photo-carrier mobility, and (d) Number of photo-generated charge carriers. The pixel spacing is 25μm for all measurements.

among mobility, photocurrent, and number of carriers seen in Fig. 5.3 are still evident at the finer resolution imaged in Fig. 5.4.

In this section we demonstrated a characterization technique, μCELIV, which enables the simultaneous study of mobility and photocurrent variations in a photovoltaic device over cm^2 areas with micron-scale resolution. The technique is demonstrated on an organic photovoltaic device, but it is generally applicable to a wide range of photovoltaic materials. This can be done by numerically modeling the current transient curve using a combination of the continuity, current, and Poisson equations to get an equation equivalent to Eq. 5.1 for the particular photovoltaic system.

This technique can provide insight into the effect of spatial inhomogeneity on device properties. The nondestructive nature of this technique allows it to be used in complete working devices over large areas to scan for deleterious inhomogeneities in a wide range of semiconductor devices.

5.2 Simultaneous Measurements of Performance Metrics and Material Deformations

In this section we introduce a novel hyperspectral laser beam induced current (LBIC) system that uses a supercontinuum laser that can be tuned from 400nm - 1200nm with diffracted limited spot size. The solar cell is light biased while simultaneously being illuminated by a chopped laser beam at a given wavelength. Current-voltage measurements performed by measuring the current perturbation due to the laser using a lock-in amplifier allow us to extract performance metrics at a specific lateral position and depth (by tuning the wavelength of the laser) while the device is at operating conditions. These parameters are simultaneously compared to material deformations as determined from the doping density, and the built-in voltage. Concurrently we also probe lateral recombination variation by measuring the activation energy thereby providing a comprehensive and unique analysis.

5.2.1 Hyperspectral Laser-Beam Induced Current Technique

The laser beam induced current (LBIC) method has been demonstrated to be a useful technique for measuring the spatial variation of photocurrent response over the lateral area of semiconductor devices such as solar cells and photodiodes. LBIC produces a two-dimensional spatially resolved photocurrent map of a semiconductor surface by rastering a focused laser beam over the surface and recording the device's photocurrent response to this optical excitation. In previous studies, this technique proved useful for the investigation of grain boundaries in polycrystalline solar cell materials as well as localized shunts and other spatial inhomogeneities [156, 157]. Due to the monochromatic output of typical lasers, previously demonstrated LBIC systems have been limited to single wavelengths for single-laser systems, or to only a few different wavelengths for some systems that combine multiple monochromatic lasers [158]. Despite these spectral limitations, lasers are used in LBIC systems because of their ability to be focused down to a spot size approaching the diffraction limit ($\sim$ few microns for visible light), which determines the lateral spatial resolution of the photocurrent maps produced using the LBIC technique.

In this section, we describe a novel hyperspectral LBIC system that uses as its light source a supercontinuum (SC) laser with white light output from

400nm to 2000nm in combination with a tunable acousto-optical filter (AOF), yielding monochromatic laser light that can be tuned from 400nm-1200nm. The use of reflective optics enables diffraction limited spot sizes (∼ few micron) over this entire spectral range. In addition to the ability to perform standard LBIC measurements at any wavelength from 400nm to 1200nm, the system can measure complete external quantum efficiency (EQE) curves at each pixel by scanning the wavelength over the desired range. By fitting the EQE curve to a band edge model, we can extract an optical band gap (E_g), and back surface recombination parameters [159].

A voltage sweep is applied to the light-biased device while it is being illuminated by a chopped laser. The current measured using a lock-in amplifier provides the AC component of the current response from the device, which corresponds to the current that is photo-generated by the laser. By examining the AC component of the current response, specifically the points of saturation of the laser photocurrent, we calculate the built-in voltage as well as the doping density at a given location and depth. In order to understand lateral recombination dynamics we further measure the spatial variation of the open-circuit voltage due to the laser as a function of temperature thereby extracting the activation energy at a given location and depth. Combining these techniques together gives us a comprehensive and thorough analysis system for solar cell characterization.

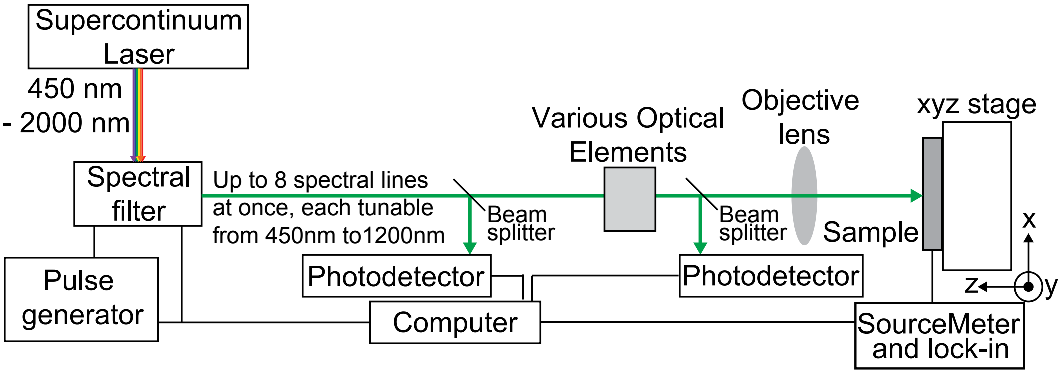

Figure 5.5: Schematic of the measurement apparatus showing the SC laser aligned and focused onto an x-y-z stage using an objective lens.

Fig. 5.5 shows a schematic of the measurement apparatus. The broadband SC laser output (Fianium, WhiteLase micro) is directed into the AOF for tuning the wavelength. For diffraction-limited spot sizes over the entire wavelength range, a reflective objective lens (Newport reflective microscope objective, Model 50105-02, 15x magnification and a numerical aperture of 0.4) in conjunction with a beam expander (Thorlabs, 4X reflective beam expander, BE04R), can be used. However for large area applications where much bigger spot sizes are desired, we use a standard refractive lens. The AOF is computer controlled and allows the simultaneous selective output of up to eight monochromatic (spectral FWHM $\sim$ 3-5nm) laser wavelengths. The SC laser is pulsed with a 20MHz repetition rate and 6ps-wide pulses, although the measurements described in this work are concerned with time-averaged behavior over much longer timescales, and so all optical powers referred to in this thesis are time-averaged powers. All mirrors used in the setup are silver mirrors with an average reflection greater than 97.5% from 450nm to 2 μm in order to guarantee high, relatively constant reflectance over the spectral range of interest. The sample is placed on a an x-y-z stage (x and y: Newport GTS150, z: Newport GTS30V) with on-axis accuracy of ± 1 μm over a 150 mm travel range in the x and y in-plane directions, and an on-axis accuracy of ± 0.75 μm over a 30 mm travel range in the z-direction. For larger area applications, x-y stages (Zaber T-LSR150B) with on-axis accuracy of ± 15 μm over a 150 mm travel are used instead. The stage includes a thermoelectric cooler capable of tuning the temperature from 5°C - 65°C using an Arroyo Instruments 5400 TECSource temperature controller. The incident laser beam is chopped at a frequency of 307Hz and focused onto the device using an objective lens. The photovoltaic device is biased using a Kiethley 2602 dual source meter. The current is measured by reading the voltage across a 10Ω resistor in series to the device using a Stanford instruments DSP lock-in amplifier, SR830. The reference input for the lock-in amplifier is connected to the Thorlabs optical chopper system MC2000.

5.2.2 Doping Density Variation in Silicon PVs

We demonstrate the setup on a standard multicrystalline silicon Al back surface field (Al-BSF) solar cell (156mm x 156mm) made from a 200μm p-type wafer with $\sim 10^{16}$ cm^{-3} background concentration of boron resulting in a bulk wafer resistivity $\sim$1-2 Ωcm. The front side emitter is phosphorus doped with sheet resistance of $\sim$60-70 $\Omega/\square$ and a depth of $\sim$200nm. The surface is an isotropically etched crater-type structure (i.e., isotexture) with a $\sim$75 nm passivation layer of hydrogenated amorphous silicon nitride film with an index of $\sim$2.0-2.1 (at 600 nm). The front and rear contacts are prepared using standard screen-printable pastes for Al-BSF cells and co-fired following screen-printing.

Using the SC laser, we can select a wavelength that corresponds to a given absorption depth into the device. The wavelength used for this study is 1064nm, corresponding to an absorption depth greater than the thickness of the silicon device [160]. For these measurements we adjust the laser beam to have a relatively large spot size on the device of 1mm, although the system

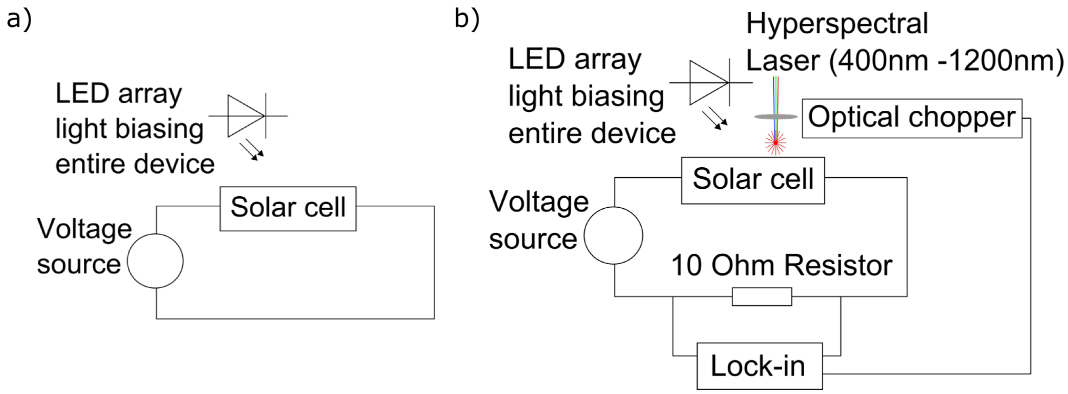

Figure 5.6: A simplified schematic of the measurement apparatus showing measurement of the (a) DC component, and (b) the AC component of the I-V curve.

is capable of diffraction limited beam diameters of a few microns. The entire device is light biased using two 18 x 12 LED (light emitting diode) arrays at a color temperature of 5600K to mimic solar conditions.

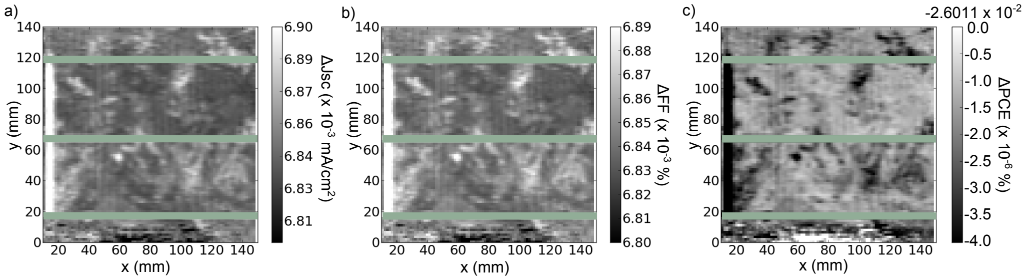

Figure 5.7: Spatial maps of variation in a) Δ Jsc (mA/cm^2), b) Δ Fill factor (%), and c) Δ Power conversion efficiency (%) extracted for a 808nm laser illuminated sample with a bias light. The horizontal green bars represent bus bars on the sample. Laser spot diameter = 1mm.

While the entire device is being illuminated by the bias light and the chopped laser light at a given spatial position, a voltage bias is applied. In series with the device, a 10Ω resistor is connected across which the voltage is measured using a lock-in amplifier at the same frequency as the chopping of the laser. Using this voltage, the current through the device was extracted, and a current-voltage (I-V) curve was determined at each spatial location on the device. The AC I-V curve extracted using the lock-in is the photogenerated current due to the excitation of the laser only. This is a perturbation to the light biased I-V curve. A simplified schematic figure shown in 5.6 shows the measurement of (a) the DC, and (b) the AC component of the I-V curve. By adding the AC I-V curve (corresponding to the current photogenerated by the laser at one spatial location) to the DC I-V curve (corresponding to the current photogenerated by the bias light over the entire device surface), the open circuit voltage (V_{OC}), the short circuit current density (J_{SC}), the fill factor (FF) and the power conversion efficiency (PCE) are extracted. These extracted parameters for each spatial location are then subtracted by the common light biased parameters for the entire device resulting in the Δ of these parameters due to the laser at each location. This gives us the lateral variation in these parameters from the bulk I-V characteristics. These maps (shown in Figure 5.7 a-c) allow for a relative comparison of the variation of each of these parameters over the lateral area of the device. We can detect regions of lower and higher power conversion efficiencies and simultaneously correlate the performance to other parameters. A lower ΔJ_{SC} on the two-dimensional maps corresponds to more photogenerated current, a higher ΔFF corresponds to improved fill factor, and a higher ΔPCE points towards better power conversion efficiency from that lateral region.

The extracted I-V curves (both only light biased and light biased with the chopped laser) can also be fit to a simple diode equation, Eq. 5.3, allowing for the extraction of saturation current density (J_0), diode quality factor (n), series resistance (R_S), and shunt resistance (R_{SH}). As before, the change in these parameters (Δ) due to the perturbing laser can be determined by subtracting the parameters extracted by fitting to the bias plus laser curve minus the parameters fit to the bias only curve. The lateral variation from the bulk values is shown in Figure 5.8 a-d) respectively.

$$J = J_L - J_0(e^{q\dfrac{V+IR_s}{nkT}} - 1) - \frac{V+IR_s}{R_sh} \tag{5.3}$$

where J_L is the current due to illumination, J_0 is the saturation current, q is the electronic charge, k is the Boltzmann constant, and T is the temperature in Kelvin. Areas of higher shunt resistance and lower series resistance are clearly visible on these maps.

The poorer or better performing regions in the PCE map from Figure 5.7 c) can now be identified from these parameter maps. A careful analysis of these maps allows us to identify the cause of the lateral performance variations. Regions of improved FF in Figure 5.7 b) can be associated with lower R_S and increased R_{SH} in Figures 5.8 c) and d). The primary cause of the PCE variation in Figure 5.7 c) can be identified as lower diode quality factors (Figure 5.8 b) and increased reverse saturation current density (Figure 5.8 a). This is

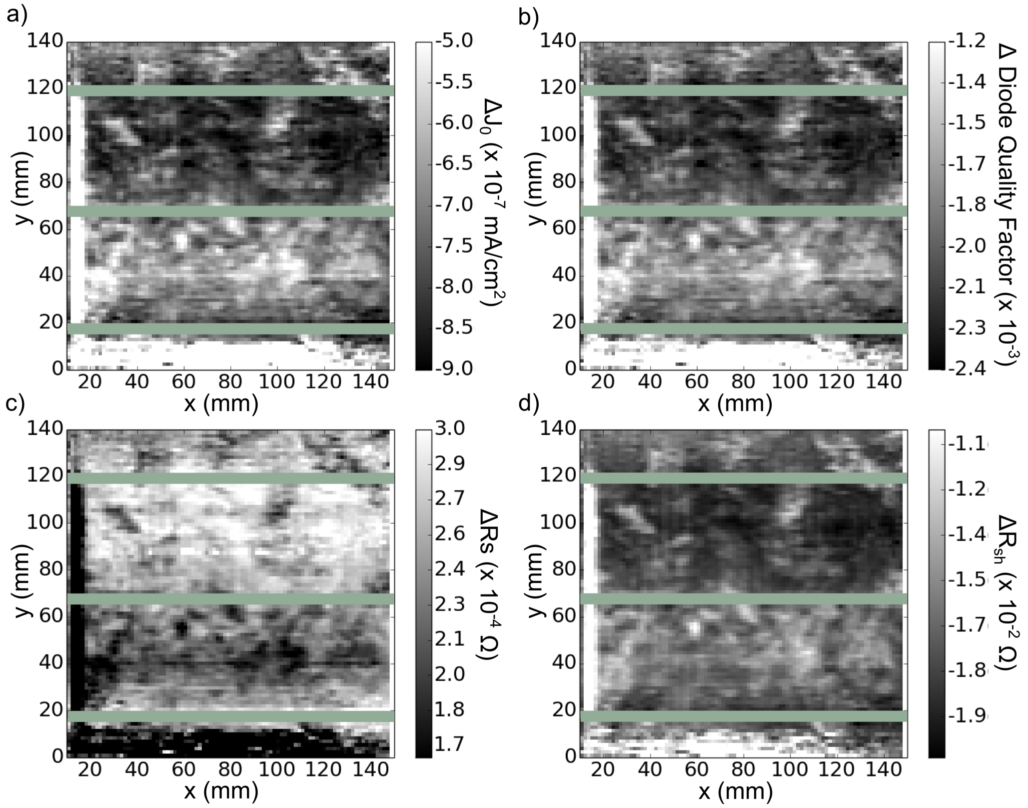

Figure 5.8: Spatial maps of a) ΔJ_0 (mA/cm^2), b) Δ Diode quality factor, c) Δ Series resistance (Ω) and d) Δ Shunt resistance (Δ) extracted by fitting the current-voltage curve to Equation 5.3. The horizontal green bars represent bus bars on the sample. Laser spot diameter = 1mm.

later confirmed using an independent technique (photoluminescence).

Using the same setup, we concomitantly measure the activation energy (E_a) in order to understand the lateral variation of recombination dynamics. The perturbation in V_{OC} of the solar cell (under white light bias) is measured using a lock-in amplifier due to the chopped laser illuminating the device at each spatial location while the temperature of the cell is varied from 5°C - 65°C. Using the variation of V_{oc} as a function of temperature, we extract the activation energy using Equation 5.4.

$$V_{oc} = E_a - nkTln[\frac{J_{00}}{J_L}] \tag{5.4}$$

where J_{00} is constant in temperature. We can compare this extracted acti-

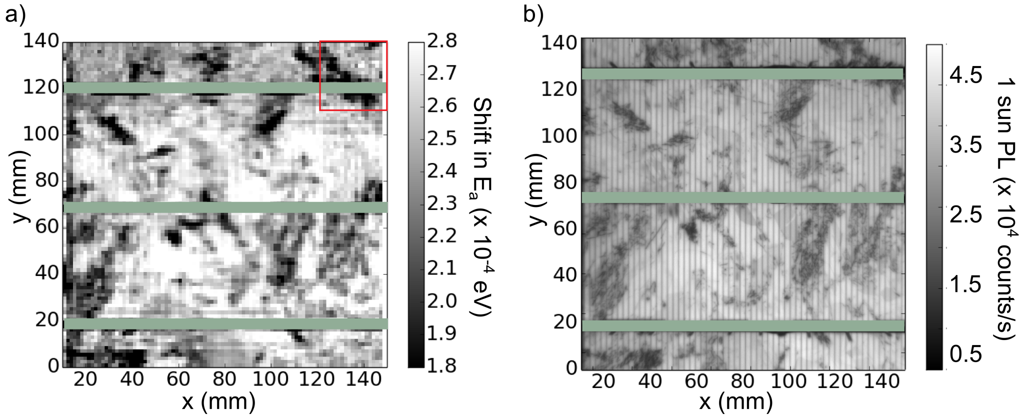

Figure 5.9: (a) Activation energy (E_a) due to 1064nm laser perturbation at each spatial location. (b) Photoluminescence map at 1 sun conditions.

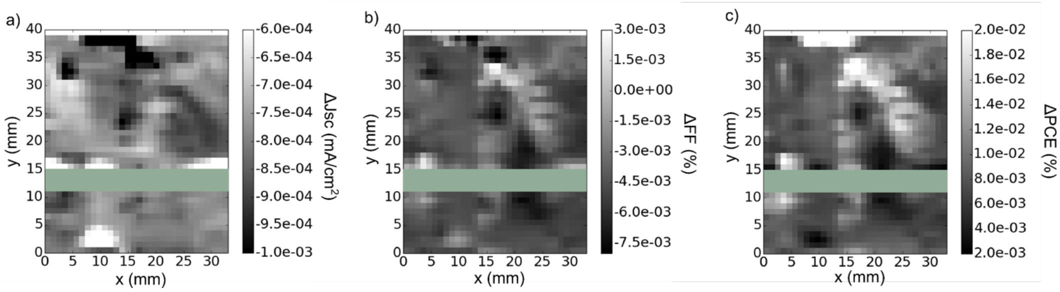

Figure 5.10: A fine spatial map of the area shown as the red square in 5.9. Variation in a) Δ Jsc (mA/cm^2), b) Δ Fill factor (%), and c) Δ Power conversion efficiency (%) extracted for a 808nm laser illuminated sample with a bias light. The horizontal green bars represent bus bars on the sample. Laser spot diameter = 1mm.

vation energy to an established technique such as photoluminescence. Figure 5.9 shows (a) E_a due to the laser perturbation, and (b) Photoluminescence at 1 sun conditions with a photon flux of 2.86 x 10^{17}cm^{-2}s^{-1} and an exposure time of 1 second. This allows to confirm the lateral variation of recombination extracted using E_a since areas showing lower E_a in Figure 5.9 a) show a lower PL signal in Figure 5.9 b).

We can expand the area outlined by the red square in Figure 5.9 a) for a deeper analysis. This is shown in Figure 5.10. Focusing on the area at (15, 25) shows a decrease in the short circuit current and the fill factor which results in an overall decrease in the PCE. In order to understand this variation we perform a scan of the change in the series and shunt resistance in the same area.

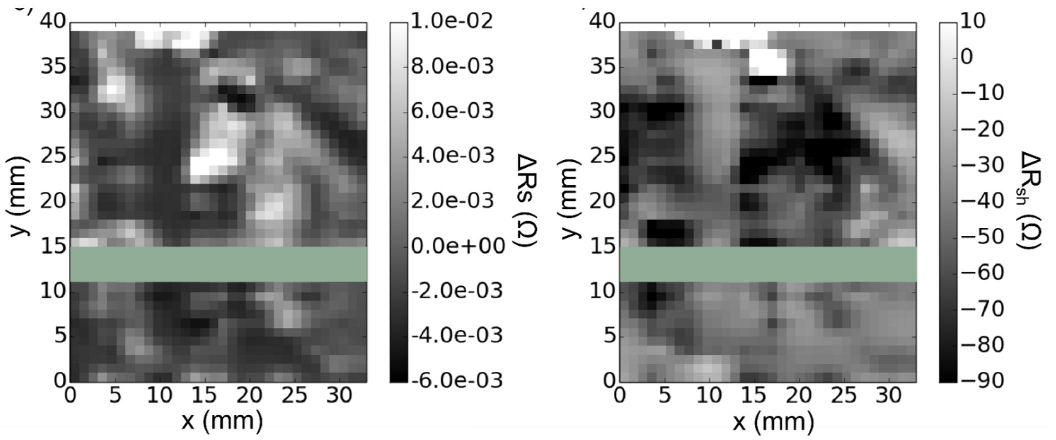

Figure 5.11: A fine spatial map of the area shown as the red square in 5.9. Variation in a) Δ Series resistance (Ω) and b) Δ Shunt resistance (Δ) extracted by fitting the current-voltage curve to Equation 5.3. The horizontal green bars represent bus bars on the sample. Laser spot diameter = 1mm.

Figure 5.11 shows the (a) Δ series and (b) Δ shunt resistances from the same area as in Figure 5.10. The region at (15, 25) which was showing a decrease in overall PCE also shows an increase in the ΔR_S and a decrease in ΔR_{SH}. In order to connect the increase in the ΔR_S to material properties, we can use the AC I-V curve.

We extract built-in voltage (V_{bi}) and the doping charge concentration (N). From the AC current photo response the depletion depth (x_d) is calculated at the applied bias voltage:

$$x_d = \sqrt{\frac{2\epsilon(V_{bi} - V)}{qN}} \tag{5.5}$$

where ϵ is the permittivity, and q is the electronic charge. When the depletion depth reaches zero, the bias voltage is equal to the built-in voltage. On the other hand, when the depletion depth is equal to the entire device thickness, the charge concentration can be extracted using the calculated built-in voltage. This analysis is conditional upon laser illumination with a wavelength where the absorption depth is greater than or equal to entire thickness of the device. An example of the AC current (mA) curve as a function of the voltage sweep can be seen in Figure 5.12. As the voltage is increased the depletion width of the device goes from being the entire thickness of the device to 0 μm.

This AC Current (mA) vs. Voltage (V) curve is taken at each point on the

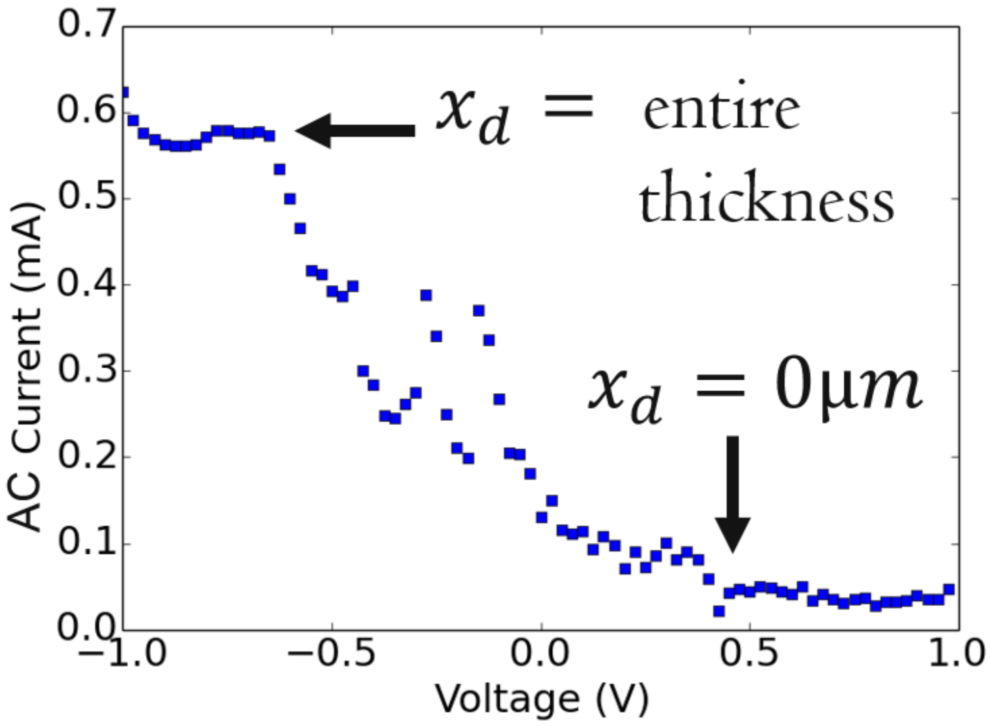

Figure 5.12: An example of a AC Current (mA) curve as the voltage is sweeped from -1V to 1V.

device and the built-in voltage, V_{bi}, and the doping charge concentration (N) is extracted at each point on the device.

The region with the higher series resistance in 5.11 (15, 25) shows a decreased doping density (Figure 5.13). This could explain the higher series resistance. We can perform an intensity correlation analysis on the two maps to understand 2D correlation. Figure 5.14 shows the two maps overlayed. Using a feature size of 10mm, we perform a 2D colocalization analysis and get a value of -0.189 which is statistically significant up to 3σ.

This analysis using spatially resolved performance metrics along with activation energy and band gap will enable for a deeper understanding of the recombination dynamics and a mechanistic knowledge of lateral performance variation, and could be correlated with spatial maps of complimentary parameters such as the charge collection probability [79].

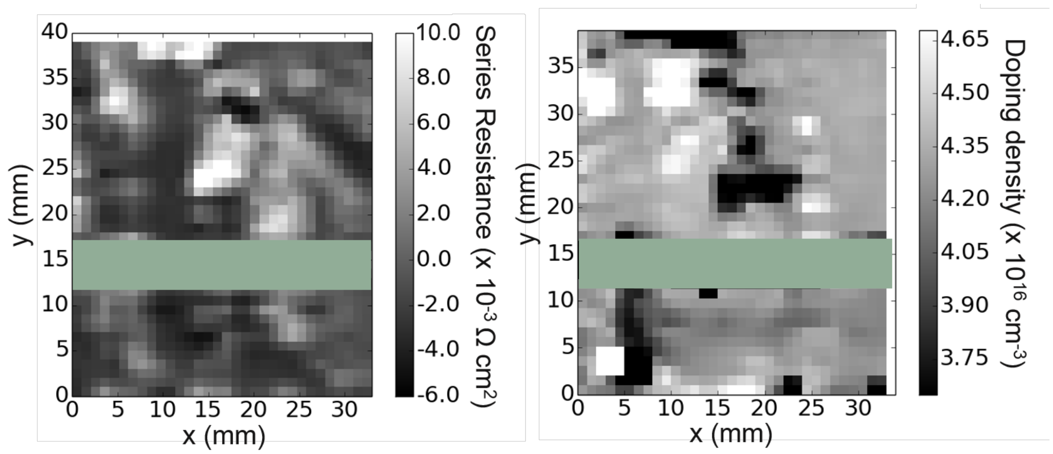

Figure 5.13: (a) Δ Series Resistance (Ωcm^2) and (b) Doping charge concentration (cm^{-3}) as calculated using Eq. 5.5 at each spatial location. The horizontal green bars represent bus bars on the sample. Laser spot diameter = 1mm.

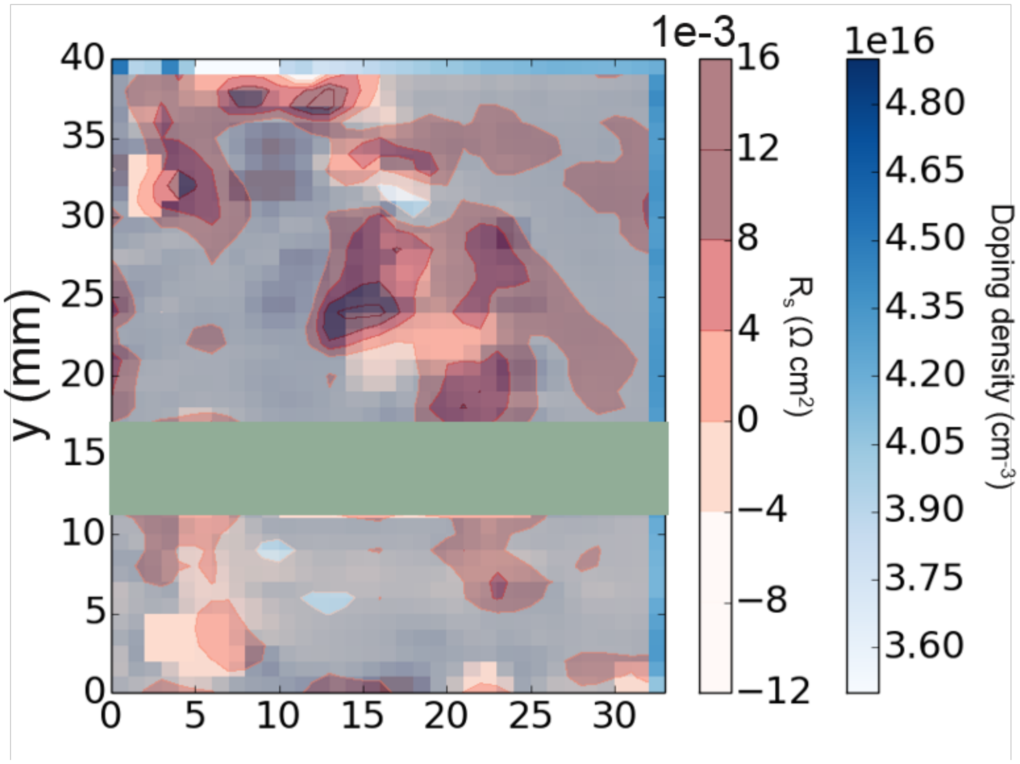

Figure 5.14: An overlay of the Δ Series Resistance (Ωcm^2) and Doping charge concentration (cm^{-3}) as calculated using Eq. 5.5 at each spatial location. The horizontal green bars represent bus bars on the sample. Laser spot diameter = 1mm.

Chapter 6

Exploiting Inhomogeneity for Novel Device Architectures

Although inhomogeneities are often detrimental to photovoltaic devices, by understanding variations in material properties and their effect on the performance metrics of a device, we can exploit them for our benefit. This section will outline novel device architectures and materials that leverage engineered inhomogeneities at surfaces.

Key Findings:

- We demonstrate strong (2.11x10^{13} e/cm^2), robust, and spontaneous n-doping of multi-layer graphene on polycrystalline $Cu(In_{1-x}Ga_x)Se_2$ due to surface-transfer doping from sodium ions embedded in CIGS
- We demonstrate broadband tunable antireflection using densely packed silicon nanotextures, comprising a surface layer whose optical properties differ substantially from those of the bulk, providing the key to improved performance

6.1 n-doping of Graphene due to Sodium Inhomogeneity in CIGS

As mentioned in Chapter 4, CIGS photovoltaics are a promising candidate for low-cost, high-throughput, and sustainable solar cell technology, [161] with champion cell power conversion efficiency of 20.5 %. Despite being one of the most efficient thin-film technologies, 21% efficiency is still significantly lower than theoretical maximum of 32.5%. A primary reason for this disappointing performance is parasitic optical absorption from the standard top-layers CIGS solar cells, including the n-doped CdS (~50 nm) buffer layer that creates the built-in electric-field at the interface with p-doped CIGS, and the Al-doped ZnO (AZO) (~160 nm) and intrinsic-ZnO (iZnO) (~80 nm) layers that form the transparent electrode on top of the CdS layer. Together these layers absorb light in different wavelength ranges ($<$500 nm for the AZO, $<$400 nm for the iZnO and $<$700 nm for the CdS), which then gets lost as heat, resulting in a decrease in η by about 5% (absolute). This optical loss can be significantly reduced by replacing these sub-layers with materials having higher optical band-gaps. As an example, the CdS layer which has a band-gap of 2.4 eV could be replaced with ZnS which has a band-gap of ~3.6 eV [162, 163]. Similarly, there has been significant interest in replacing these conventional top layers using materials such as $Cd_{1-x}Zn_xS$, (Cd,Zn), $Zn_x(O,S)_y$, $Zn(O,S,OH)_x$, ZnO, $Zn(O,OH)_x$, In_2S_3, $In(OH)_3$, SnO_2, $Sn(S,O)_2$, ZnSe, $Zn(Se,OH)_x$, ZrO_2, MnS, or $Mn(S,OH)_x$. [164–167] Among them, the use of $Cd_{1-x}Zn_x$ and ZnS have shown the largest improvements in optical transmission. However, use of non-conventional top layers can also crucially affect the electrical properties in the CIGS, which can lead to a lower open circuit voltage (V_{oc}), higher series resistance (eg. ZnS), and overall lower η. Finally, there is also the desire to completely eliminate Cd from the cell due to its toxicity.

Graphene[168, 169], which is a quasi two-dimensional crystalline material consisting of a hexagonal orientation of carbon atoms, is extensively explored and offers great promise for a host of novel optoelectronic applications, including graphene-semiconductor diodes, batteries, fuel cells, sensors, and solar cells[170]. Among its unique electrical properties, the combination of excellent optical transmission (97.7%)[169] with rapid charge transporting properties (~ 25,000 30,000 $cm^2V^{-1}s^{-1}$ for substrate-bounded graphene and greater than 200,000 $cm^2V^{-1}s^{-1}$ for suspended graphene [171] is promising for development of low-cost and flexible transparent electrical contacts for solar cells and photodetectors [172, 173]. If graphene could be used directly as part of the p-n junction, in addition to the its somewhat limited use as an electrode, it will be possible to harness its full potential in photovoltaic device applications by eliminating the parasitic resistance of many common n-type emitter layers such as the CdS in CIGS and CdTe thin-film photovoltaics, and allowing band-offset engineering of the p-n junction through precise doping control of the graphene.

The direct incorporation of graphene as part of the active-junction and a replacement for the CdS, iZnO, and AZO in CIGS solar cells is requires the ability to strongly and sustainably electron (n) or hole (p) dope graphene. Thus far electrostatic doping has been used to realize n (p)-doped graphene interfaced with p (n)-Si as Schottky diodes[174]. Furthermore, extrinsic chemical p-type doping has resulted in the development of surprisingly efficient photovoltaic devices between graphene and n-type Si[175, 176]. However, unlike the strong p-type doping, obtained when graphene is bound to substrates such as Si that harbor hydroxyl ions captured from the ambient air, achieving strong and persistent n-doping has been more challenging. Even though chemical approaches have been proposed for n-doping, the doping strength has been limited, and n-doped graphene interfaced with a technologically relevant p-type semiconducting substrates has not been realized[177]. As a result, permanent n-doping is a major challenge until now that prevented the coupling of n-doped graphene with intrinsically p-doped photoactive solar cell materials such as CIGS and CdTe, which comprise the largest the majority of commercial thin-film photovoltaic technologies today.

6.1.1 Sodium Inhomogeneity in CIGS Devices

We demonstrate a scalable method for achieving strong n-doping in pristine CVD/exfoliated graphene via electron-transfer from Na atoms embedded in low-cost soda-lime-glass substrates, which can be a robust platform to realize n-graphene and p-semiconductor junctions for optoelectronics devices including thin-film photovoltaics. We discover that n-doping effect is further strengthened by the diffusion and concentration of the dopant Na near the top air-surface of a standard 2-μm p-type CIGS/Mo photoactive thin-film when deposited on soda-lime glass. The fundamental basis of the doping mechanism is supported by theoretical and experimental findings that the adsorption of alkali metal atoms, including Na, as a monolayer adjacent to graphene can create uniform n-doping in graphene via ground-level electron transfer[178]. However, the reactivity of alkali metals and weak doping strengths have limited the practical demonstration of n-doping of graphene in functional device applications[179]. We solve these drawbacks and utilize the sodium embedded in an inert and low-cost substrate such as production-grade soda-lime-glass and practically demonstrate a robust, scalable route towards strongly n-doping graphene for device applications by introducing a prototype photovoltaic device between n-doped graphene and the p-type CIGS on SLG with $\eta \sim 0.98\%$.

Figure 6.1 a) and b) show energy dispersive spectroscopy images of carbon and sodium in Graphene/CIGS devices. We can see the higher carbon concentration on the surface which corresponds to the graphene. Figure 6.1 c) shows an aberration-corrected high resolution-TEM cross-sectional image of the interface between multi-layers CVD graphene transferred on to a CIGS/Mo/soda-lime-glass (CIGS/Mo/SLG) substrate. The lattice separation measured (shown by the arrows) is 340 pm which is an exact match to

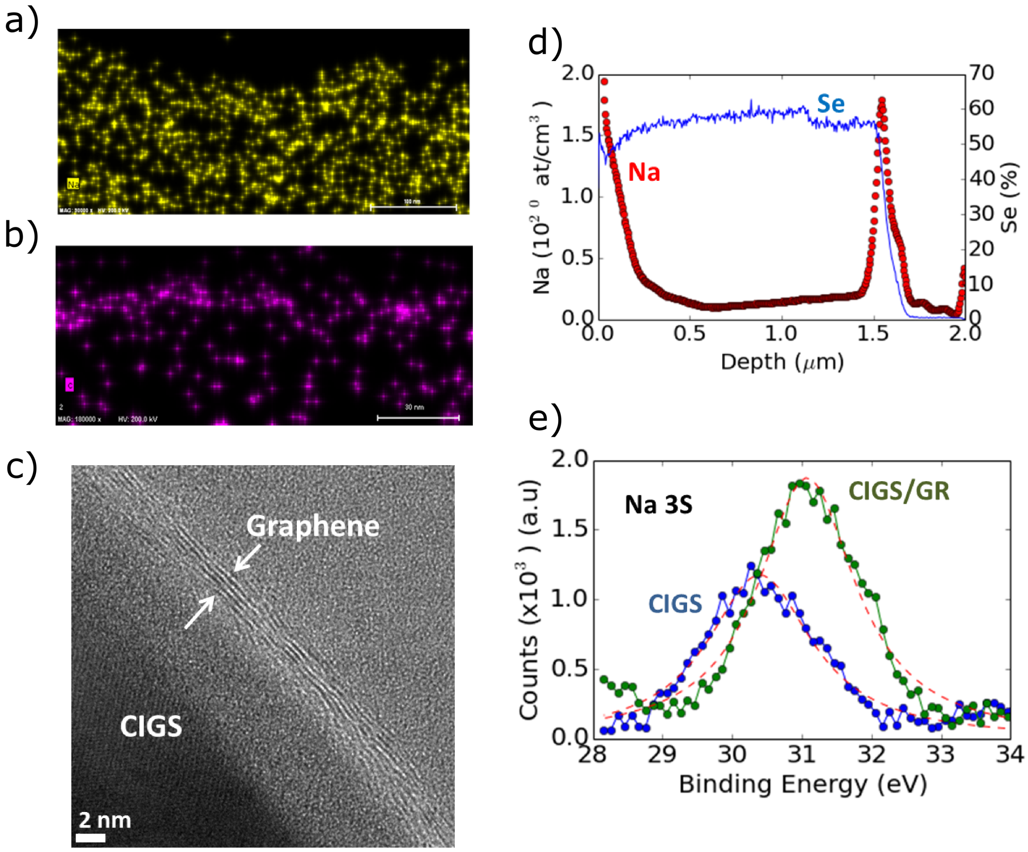

Figure 6.1: Energy Dispersive Spectroscopy (EDS) of a) Sodium and b) Carbon on graphene/CIGS on Soda-lime-glass substrate. c) Aberration corrected High resolution Transmission Electron Micrograph (HR-TEM) of a 100nm thick cross-section of the graphene/ CIGS/Mo/SLG interface. d) Time-of-flight SIMS measurement on CIGS showing depth profile of Na and Se from the top interface ($x = 0.0$ m). Na concentration increases greater than 2 x 10^{20} at/cm^3 near the top CIGS-air interface. e) X-ray photoelectron spectroscopy (XPS) of the Na 3S energy level on neat CIGS/Mo/SLG (blue-curve) and graphene/CIGS/Mo/SLG (green-curve) with the
Lorentzian curve-fits given in red-dashed lines.

pristine graphene. The impurity distribution of neat CIGS/Mo/SLG, and graphene/CIGS/Mo/SLG was investigated using (time of flight) SIMS, focusing on Na, which is a common impurity within CIGS and is found to have a major impact on the performance of state-of-art CIGS photovoltaics[180]. During the deposition process, Na atoms diffuse from the underlying SLG on to CIGS lattice which improves the growth of the film. Figure 6.1 d) shows the Na and Se distribution as a function depth from the top surface of CIGS/Mo/SLG and we use the Se depth-profile as a proxy for the entire CIGS composition and film thickness. Concentration of Na diffused from the 14% Na-rich SLG, is seen to significantly increase near the top air-surface of CIGS at a volume density of 2.0x10^{20} at/cm^3. The surface density of Na is estimated to be in the order of 10^{15} cm^{-2} which is close to the atomic density of a Na monolayer. The Na peak at the CIGS-Mo edge at 1.5m depth is from trace Na impurities in the Mo sputter target localized near the Mo-CIGS interface). In the EDS data, at the graphene/CIGS interface, the carbon signal shows a higher intensity attributed to graphene however Na density seems uniform. This is likely due to the the detector saturation limit in EDS. EDS mapping also reveals that Na is uniformly distributed in-plane to graphene with close proximity to the carbon lattice, suggesting fertile grounds for electronic interaction between Na and graphene. Evidence of possible ground-level electron-transfer from Na into graphene is measured via XPS which probes up to 10nm from the top of the graphene/CIGS interface. Figure 6.1 e) shows the Na 3S binding energy (BE) of the neat CIGS/Mo/SLG (blue-curve) and graphene/CIGS/Mo/SLG (green-curve). It is seen that the Na 3S peak is shifted higher by 680meV from 30.39 eV to 31.07 eV upon contact with graphene. Similarly, core Na 1S peak is also shifted by 490meV higher and BE increase in both the valence and core orbitals in Na after graphene deposition suggest net positive charging of Na, suspected from a strong ground-level electron transfer from Na in to graphene [181, 182]. Moreover, density functional theory (DFT) calculations on graphene interacting with a monolayer of Na show 482 meV shift in the Fermi energy at the K point in graphene Brillouin zone also support n-doping mechanism at the interface (DFT calculations were performed by collaborators and are being presented in the thesis for the sake of completeness). The DFT calculations are in full agreement of n-doping seen via alkali metal absorbed on graphene reported earlier[178]. Therefore, using above experimental observations and DFT calculations, we postulate that graphene is strongly n-doped from charge transfer from Na atoms concentrated on the interface of CIGS deposited on SLG.

6.1.2 CIGS/Graphene Devices

We explored the n-doped graphene on CIGS/Mo/SLG as a charge-separating junction and as a transparent top contact for a prototype thin-film photovoltaic device. Figure 6.2 b) is the I-V measured between graphene and the Mo electrodes in dark (dashed-curves) and light (solid-curves), with (red curves) and without (blue curves) the Al_2O_3 gate dielectric on graphene. It is seen that n-graphene/p-CIGS/Mo/SLG forms a non-linear junction and generates

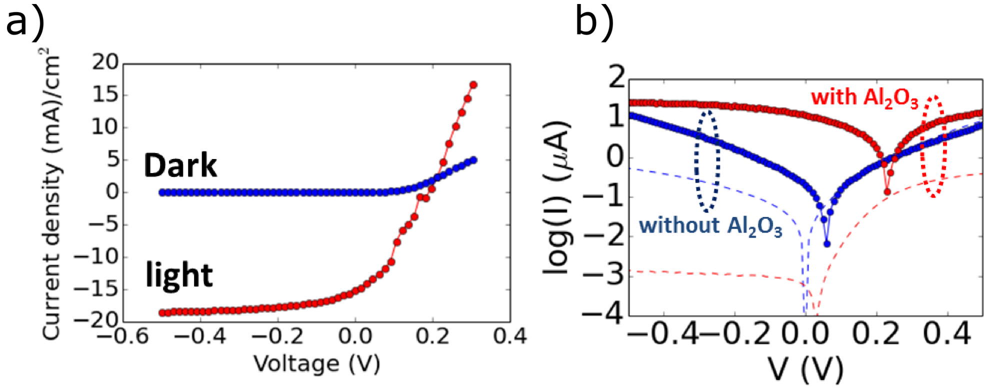

Figure 6.2: a) Graphene and Mo optoelectronic measurements with Al2O3 top-dielectric (red curves) and without the Al2O3 (curves) top-dielectric under light (solid-line) and dark (dashed-line). b) The I-V characteristics of the graphene/CIGS device measured under AM1.5G.

photocurrent under illumination. Moreover, deposition of the Al_2O_3 dielectric enhances the non-linearity of the junction (resulting in an ideality factor of 1.29) reducing the reverse saturation current (J_0) and increasing rectification rate. The improved diode behavior also enhances the photocurrent generated in graphene/CIGS/Mo/SLG after the deposition of the top-dielectric. We attribute this improvement to screening of graphene from p-type counter-dopants from ambient oxygen resulting in overall higher net n-doping which improve the overall junction properties. These counter p-dopants are confirmed to be oxygen, seen by the shift in the oxidation state of oxygen 1S measured by XPS, after graphene is transferred on to CIGS (Figure 6.3).

We measure the photovoltaic behavior of the graphene/CIGS/Mo/SLG junction fabricated above under AM1.5G illumination, as shown in Figure 6.2 a), where short-circuit current (J_{sc}) of 13.6 mA/cm2, fill factor of 0.35 and V_{oc} of 210 meV results in η of 0.98%. The η is primarily limited by the lower open circuit voltage V_{oc} and lower fill-factor. The ideality factor is calculated as 1.21, which indicates lower recombination in the space-charge region from Shockley-Read-Hall (SRH), but higher interfacial recombination from tunneling-enhanced recombination processes. Apart from recombination losses, the performance of above prototype graphene/CIGS is affected by the higher sheet resistance (R_s) of ∼15 kΩ/sq of graphene on CIGS/Mo/SLG in the dark, which is more resistive than single and multilayer graphene (180 - 3000 Ω/sq.) on smooth dielectrics such as Si/SiO2, quartz or plastic[183, 184]. We attribute the higher R_s to possible graphene-CIGS substrate-interactions,

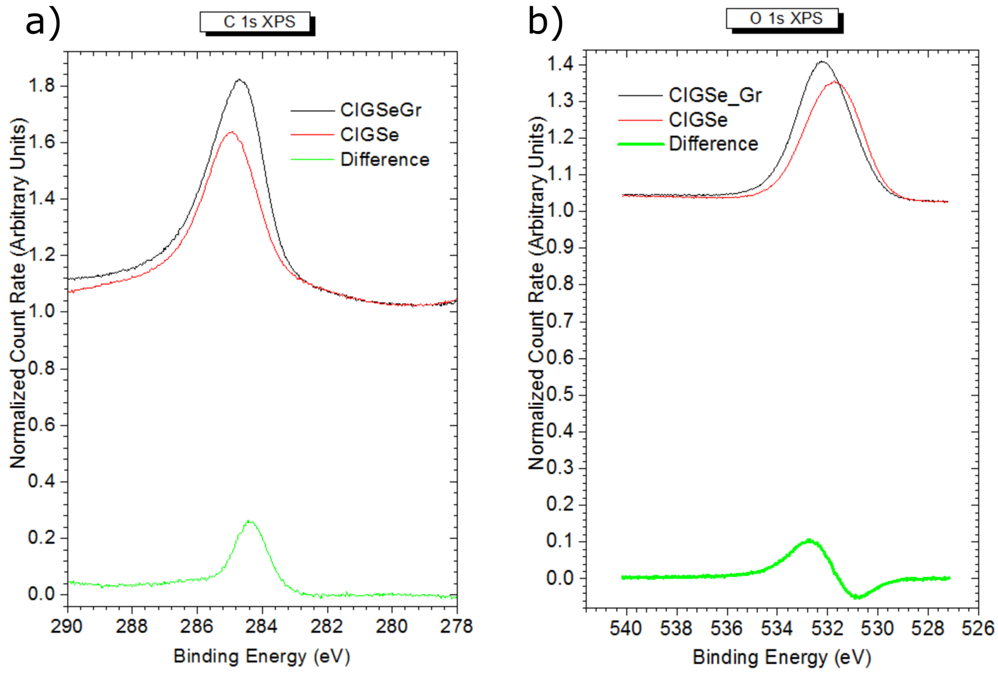

Figure 6.3: a) XPS of the C 1S before and after the deposition of graphene. The extra peak after graphene deposition (green curve) is at 284.3 eV which agrees with sp^2 hybridized graphene reported in literature. b) XPS of the oxygen peak of CIGS before and after the deposition of graphene. A shift in the oxygen peak to higher energies points to a change in oxidation state from metal oxides to more hydroxyls.

structural damage of graphene upon transfer on to the rough CIGS as well as potential degradation sustained from the deposition of the top-dielectric on graphene. Furthermore, the carrier mobility (17 $\mathrm{cm^2V^{-1}s^{-1}}$) of the graphene layer on CIGS/Mo/SLG is also significantly lower than pristine graphene on smooth dielectric substrates, as a result of the above mentioned degradation processes.

The behavior of J_0 vs. temperature (T) is modeled assuming Landauer transport [185] in the GR/CIGS/Mo/SLG (Fig. 6.4 a) giving $\Phi_b = 0.13$eV. Assuming ideal Schottky-diode behavior, $ln(J_0/(T^2))$ vs. $1/T$ (inset to Fig. 6.4 a) yields $\Phi_b = 0.11$eV, with a constant Richardson coefficient of 4x10^{-4} $\mathrm{Acm^{-2}K^{-2}}$. As is discussed below, this range for Φ_b is lower than expected, which we believe is due to surface defects and surface sodium doping of CIGS that lowers the surface ionization potential of CIGS relative to the bulk.

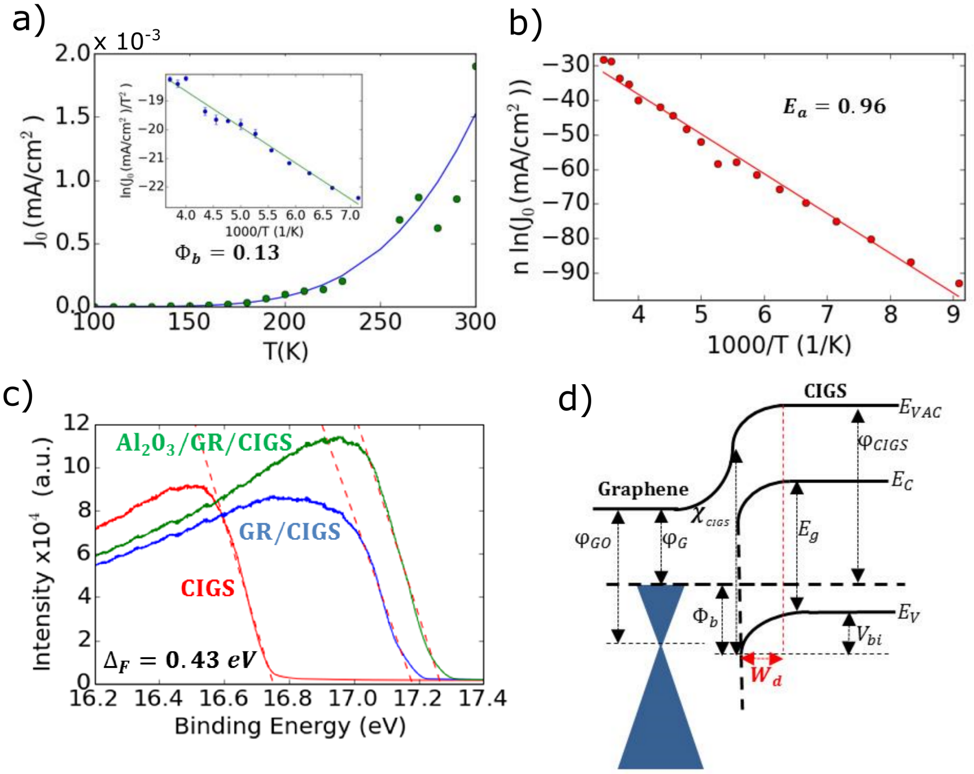

Figure 6.4: (a) Data (green circles) and best-fit model prediction (solid blue line) for J_0 (mA/cm^2) vs. T for GR/CIGS/Mo/SLG, using a Landauer transport model giving Φ_b = 0.13eV. (Inset) Same data (blue circles) plotted as ln(J_0/(T^2)) vs. 1000/T where J_0 is in mA/cm^2 and T is in K, but using an ideal Schottky diode model, $J_0 = A^*T^2exp^{(-\Phi_b)/kT}$, for the solid green line with best-fit value Φ_b = 0.11eV. (b) Same data (red circles) used in panel (a), but plotted as a modified Arrhenius-plot ($n*ln(J_0/(T^2))$ vs. $1000/T$), where n is the ideality factor and J_0 is in mA/cm^2; finding the best-fit (solid red line) to the data gives Ea = 0.96eV. (c) Ultraviolet photo-electron spectroscopy (UPS) on the CIGS/Mo/SLG (red) , graphene/CIGS/Mo/SLG (blue) and Al_2O_3/graphene/CIGS/Mo/SLG (green) to find the shift in the CIGS work function with graphene and Al_2O_3 deposited on Al_2O_3. (d) Schematic band structure of multi-layer-GR/CIGS/ Mo/SLG interface. ϕ_{G0} = Work function of intrinsic graphene, ϕ_G = Work function of graphene, Φ_b = Schottky barrier height, χ_{CIGS} = Work function of CIGS, IP$_{CIGS}$ = Ionization potential of CIGS, E_G = Band gap of CIGS, V_{bi} = Built-in potential.

For an ideal Schottky barrier, $J_0 = A^*T^2e^{(-\Phi_b)/kT}$ where Φ_b is the Schottky barrier height. By fitting $ln(J_0/T^2)$ vs. $1000/T$, we obtain Schottky barrier height of $\Phi_b = 0.11$eV and $A^* = 1.18\text{x}10^{-6}$ mAcm^{-2}K^{-2}. This is assuming a fixed Richardson constant A^*. For finite density of states, A^* becomes temperature dependent and the Landauer transport model is used as given below:

$$J_0 = \big[\frac{qD_o}{\tau}(k_BT)^2(\frac{\Phi_B}{k_BT}+1)\big]e^{-\Phi_B/(k_BT)} \tag{6.1}$$

where $D_0 = 2/(\pi(\nabla v_F)^2$ with ∇ the Planck's constant, and v_F the Fermi velocity ($v_F \sim 10^6$ m/s for graphene) represents the prefactor that gives the graphene density of states when multiplied by the energy, and τ is the time scale for carrier injection from the contact. In order to fit this equation to the data shown in the main panel of Fig. 6.4 a), we find the best-fit values for two parameters: $c \equiv (qD_o)/\tau$ and Φ_B. The blue solid best-fit line shown in the main panel to Fig. 6.4a is Eq. 6.1 with best-fit parameter values of $c = 58.15$ and $\Phi_B = 0.13$eV. We observe that the diode quality factor is temperature dependent which means that there is a strong contribution of tunneling in the recombination mechanism. High ideality factors at low temperatures suggest a transition from tunneling dominated interface recombination at low temperatures to standard Shockley-Read-Hall (SRH) behavior at room temperature. The barrier height (Φ_b) is equal to the ionization potential of the CIGS semiconductor (IP$_{CIGS}$) minus the work function of graphene (ϕ_G), and represents the barrier that holes in the valence band of CIGS must overcome to be injected into the graphene. The activation energy (E_a), on the other hand, represents the characteristic energy that governs the rate of minority carrier (electron) excitation into the conduction band of the p-type semiconductor CIGS. In an intrinsic semiconductor, E_a is equal to half the bandgap, and for a doped p-type semiconductor like CIGS, its value should be close to the bandgap energy, since in this case the Fermi level is close to the valence band. An expression for E_a can be derived from an equation that takes the ideality factor n into account, thereby including the effect of recombination. The same J_0 data can be used in a different model where the diode quality factor, n, is taken into account. In this model the reverse saturation current, J_0 can be written as a function of temperature T, activation energy, E_a, the diode quality factor, n, and J_{00}, which is a weakly temperature-dependent prefactor.

$$J = J_0e^{qV/nkT} = J_{00}e^{-E_a/nkT}e^{qV/nkT} \tag{6.2}$$

Compared to the typical definition of activation energy, where the exponential term containing E_a does not include the ideality factor n in the denominator, Eq. 6.2 includes the n in the denominator of both exponential terms to account for the temperature dependence of n. In the case of tunneling, where the ideality factor n becomes temperature dependent, we can rewrite Eq. 6.2 to obtain

$$n \cdot ln(J_0) = -E_a/kT + n * ln(J_{00}) \tag{6.3}$$

Assuming that J_{00} is temperature independent, we can extract the activation energy E_a using a modified Arrhenius plot, $nln(J_0)$ vs. $1/T$ (in contrast to a standard Arrhenius plot - $ln(J_0)$ vs. $1/T$ that one would use when the denominator of the exponential term in Eq. 6.2 containing E_a does not include the ideality factor n). In an intrinsic semiconductor, the activation energy is equal to half the bandgap, and for a doped semiconductor it should be close to the bandgap energy since the donor/acceptor ionization levels are close to the bandgap. We extract an activation energy $E_a = 0.96$ eV which is lower than the CIGS bandgap of 1.15 eV, suggesting a contribution of tunneling enhanced interfacial recombination [131, 131].

The activation energy, E_a, represents the characteristic energy that governs the rate of carrier excitation into the conduction band of the semiconductor. Fig. 6.4 b) shows a modified Arrhenius-plot indicating dominant interfacial recombination. We have demonstrated that this interfacial recombination can be reduced using a very thin (4nm) TiO_2 blocking layer between graphene and CIGS, thereby improving V_{oc} from 0.23 V to 0.49 V. Figure 6.4 c) shows the secondary-cutoff of neat CIGS/Mo/SLG (red) , graphene/ CIGS/Mo/SLG (blue) and Al_2O_3/graphene/CIGS/Mo/SLG measured via UPS under HeI (21.22 eV) excitation. It is seen that the secondary cut-off energy is increased from 16.75 eV to 17.18 eV when graphene is deposited on CIGS and is further up-shifted to 17.26 eV when Al_2O_3 is deposited on top of graphene. The Fermi energy is therefore shifted progressively from 4.46 eV to 4.03 eV and finally to 3.95 eV for pristine CIGS, graphene/CIGS and Al_2O_3/graphene/CIGS respectively. Furthermore, we note that the overall lower Fermi energy of neat CIGS compared to literature is attributed to the presence of Na on the CIGS surface. Upon the deposition of Al_2O_3 the surface is passivated, and the Fermi level is seen to further reduce suggesting higher net n-doping consistent with the earlier measurements. We propose that the 0.51 eV difference of the Fermi energy (i.e. 4.46 eV 3.95 eV) provides the built-in potential (V_{bi}) at the junction of a Al_2O_3/graphene/CIGS/Mo/SLG which in-turn determines upper limit for V_{oc}. As discussed earlier, due to interfacial recombination V_{oc} of pristine graphene/CIGS is pinned at 0.23 V but with a hole-blocking layer

(TiO_2) the V_{oc} is increased to 0.49 V which is nearly at the V_{bi} potential of the junction. Moreover, by improved deposition of graphene on CIGS R_s could be lowered which overall can improve the performance of the graphene/CIGS junction.

The approximate band structure of the Schottky diode is given in Fig. 6.4 d). The difference between the CIGS ionization-potential ($IP_{CIGS} = 5.65$eV [186]), and graphene work function 4.69 eV [187] modified by the image-potential correction (0.15eV), gives a theoretical $\Phi_b = 0.81$eV. Due to defects and Na surface density, IP_{CIGS} is 0.5eV lower, [188, 189] yielding $\Phi_b = 0.31$eV, which is much closer to the measured range of Φ_b.

In this section, we demonstrated strong (1.33x10^{13} e/cm^{-2}, corresponding to a Fermi energy shift of +426meV), robust, and spontaneous n-doping of graphene on the surface of a low-cost industrial-grade soda-lime-glass substrate via surface-transfer doping from the Na. By leveraging the Na diffusion through a p-type CIGS semiconductor deposited onto the soda-lime glass, we applied this method to the formation of a graphene(n)/semiconductor(p) Schottky diode with even stronger graphene n-doping (2.11x10^{13} e/cm^{-2}, corresponding to a Fermi energy shift of +536meV) than was achieved on bare glass. This method of n-doping does not require any high-temperature annealing steps, and should be compatible with a wide range of semiconductor/substrate systems. The junction properties, such as Schottky barrier height and interfacial recombination rate, can be controlled by tuning the doping strength via the thickness of a few-nm dielectric layer such as TiO_2 or Al_2O_3. Advantages of this technique include the lack of external chemicals whose doping strength decays over time, the ability to achieve strong and persistent n-doping of graphene that is placed on top of a p-doped semiconductor, the ability to n-dope graphene on a wide range of p-doped semiconductors via the use of a Na host that is in direct contact with the graphene layer, and the ability to control the strength of the doping via the use of a spacer layer (e.g., TiO_2) between the Na host and the graphene layer. Disadvantages include the possible restriction to p-doped semiconductors that are not too strongly affected by the Na diffusion from the Na host to the graphene layer, in the case where the semiconductor lies between the Na host and the graphene layer. Strong, robust, and tunable graphene doping opens the door for the practical realization of many envisioned applications of graphene such as touch screens and organic light-emitting diodes1, where the reduction of sheet resistance is crucial to future success, and a broad array of other applications where strong and tunable n-doping is important, such as microelectronics, photodetectors, photovoltaics, electrochemical energy storage, and sensors.

6.2 Enhanced Broadband Antireflection in Silicon Solar Cells using Nanotextures

Materials providing broadband light antireflection have applications [190] as highly transparent glass and plastic window coatings,[191–197] as military camouflage, and as coatings for efficiently coupling light into solar cells [198–210] and out of light emitting diodes [195, 211–213]. Self-assembled block copolymer thin films can provide a scalable platform for design of material optical properties by patterning highly regular, sub-wavelength surface textures over macroscopic areas. In this section we demonstrate that densely packed silicon nanotextures with feature sizes as small as 10nm impart broadband antireflection, reducing average reflectance to less than one percent across the wavelength range from 400nm to one micron in structures as short as 155nm. This efficient antireflection results from our simultaneous control over the nanotexture profile and the silicon optical properties, which we measure using spectroscopic ellipsometry. The nanotextured surface reflectivity is quantitatively well modeled only after accounting for both its shape and changes in refractive index. Implementing this antireflection approach in crystalline silicon solar cells improves the photovoltaic power conversion efficiency by 50 percent (to 12.6% overall) compared to an untextured device, consistent with proficient coupling of all incident light wavelengths into the cell.

In order to design an antireflection coating we need to manage the mismatch of refractive indices at the abrupt optical interface between the substrate and air. The most straightforward approach uses a single thin-film layer of intermediate optical index at the interface to create destructive interference for the reflected light, providing full antireflection at only a single wavelength, $\lambda = 4n_i \cdot t$, with material thickness (t) and refractive index $n_i \equiv \sqrt{n_S n_A}$, where n_S and n_A are the refractive indices of the substrate and air, respectively. Increasingly broadband coverage requires more complex layering schemes. An alternative to thin-film coating strategies instead patterns the interface at sub-wavelength dimensions, creating an effective medium between the substrate and air with a refractive index that gradually changes from n_A to n_S [200, 201, 214]. Such structures are often called moth eyes because of their biomimicry, and have been shown to provide broadband antireflection over a wide range of incident light angles when the sub-wavelength structures are taller than $t \sim 0.4\lambda$ and spaced closer than $l \sim \lambda/(2n_s)$ [204, 207, 215–217]. The nanotextures we describe here combine these two antireflection schemes by simultaneously controlling both the geometry and optical properties, resulting in improved performance compared to either approach alone.

6.2.1 Reflectance and Nanotextured Refractive Index Profile

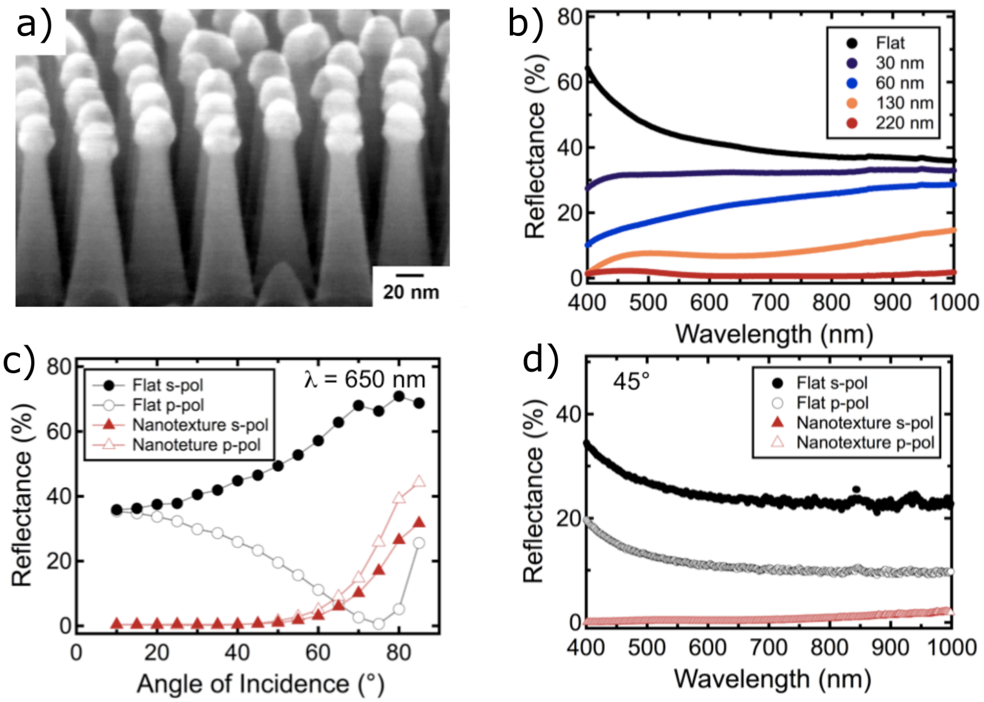

Figure 6.5: a) An example of the textured surface; 70 degree angle cross-sectional SEM image of close packed alumina nanostructures formed by infiltration of a 99 kg/mol cylindrical phase PS-b-PMMA block copolymer thin film. b) Reflectance versus wavelength for nanotextures with l = 50 nm and heights ranging from 30 nm to 220 nm. c) Reflectance (at 650 nm) for s- and p-polarization versus incident angle for flat silicon (black circles) and nanotextures with l = 50nm and height 220 nm (red triangles). d) Reflectance of s- and p-polarization versus wavelength (45 degree incident angle) for nanotextures with l = 50 nm and 220 nm height.

In this work, we combine block copolymer self assembly and plasma based etching to produce highly regular, nanotextured surfaces with precise control over the lateral feature size, vertical profile, and texture density. Fabrication was performed by collaborators and is being presented in the thesis for the sake of completeness. We pattern surface nanotextures on polished (100) silicon wafers by first self-assembling a cylindrical phase poly(styrene)-b-poly(methyl methacrylate) (PS-b-PMMA) block copolymer thin film (Mw = 99 kg/mol, PS:PMMA $\sim$ 0.7) by spin-coating (3 KRPM, spun from 1% wt. solution in toluene) and thermal annealing above the polymer glass transition temperature (205 °C in vacuum, >12 hours). Appropriate surface pretreatment prior to coating the block copolymer facilitates perpendicular orientation of uniformly sized 25 nm diameter PMMA cylindrical microdomains, locally arranged in a hexagonal lattice (with nearest neighbor separation, l = 50 nm) with the surrounding PS matrix.4243 We have systematically varied l in the self-assembled nanotexture from 42 nm to 70 nm by using block copolymers whose total molecular weight range between 67 kg/mol to 177 kg/mol. Exposing assembled copolymer films to three sequential cycles of trimethylaluminum (TMA) and water vapor selectively loads the PMMA microdomains with alumina, a process termed sequential infiltration synthesis. A subsequent oxygen plasma treatment (20W, 100 mT, 3m) removes all organic material from the surface, leaving uniformly-sized alumina nanostructures whose shape and arrangement mimics that of the initial PMMA template.

The average reflectance of the nanotextured silicon surface decreases with increasing feature height in the wavelength range of 400 nm to 1 micron, from 45% on a flat surface to less than 1% for tapered nanotextures with heights of 220 nm. The tapered vertical profile provides a gradual refractive index change from air ($n_a = 1$) to silicon ($n_s = 5.6$ at 400 nm; $n_s = 3.6$ at 1μm). Shallower nanotextures preferentially decrease the reflectance at shorter wavelengths (Figure 6.5b, blue color), consistent with the requirement of $t/\lambda > 0.4$ for full antireflection from a moth eye structure. Taller nanotextures extend the anti-reflective properties to longer wavelengths (Figure 6.5c, red color), with 220 nm tall structures providing less than 1% reflectance from 400 nm to the silicon optical bandgap. We can estimate $n_{eff}(z)$ for hexagonal arrangements of cones with subwavelength dimensions that taper to a point at their top (z = 0) and join at their base (z = t) using the effective medium approximation by calculating the fractional areal coverage of silicon and air versus depth (z): $f_{Si}(z) = \pi/(2\sqrt{3} * (z/t)^2)$ and $f_{air}(z) = [1 - f_{Si}(z)]$, with t the nanostructure height, and $z = 0$ at the cone tip. Neglecting any light absorption in either the air or silicon, we find:

$$n_{eff}(z) = \sqrt{\epsilon_{eff}} = \sqrt{\epsilon_{Si} f_{Si}(z) + \epsilon_{air}[1 - f_{Si}(z)]} \tag{6.4}$$

$$= \sqrt{\epsilon_{air} + \pi/(2\sqrt{3}(\epsilon_{Si} - \epsilon_{air})(z/t)^2} \tag{6.5}$$

The tapered surface nanotexture provides broadband antireflection over a wide range of incident light angles. The reflectance of a flat silicon surface (at 650 nm) versus incident angle is markedly different for s- and p-polarized light, while a similar silicon surface having a nanocone nanotexture with 220 nm

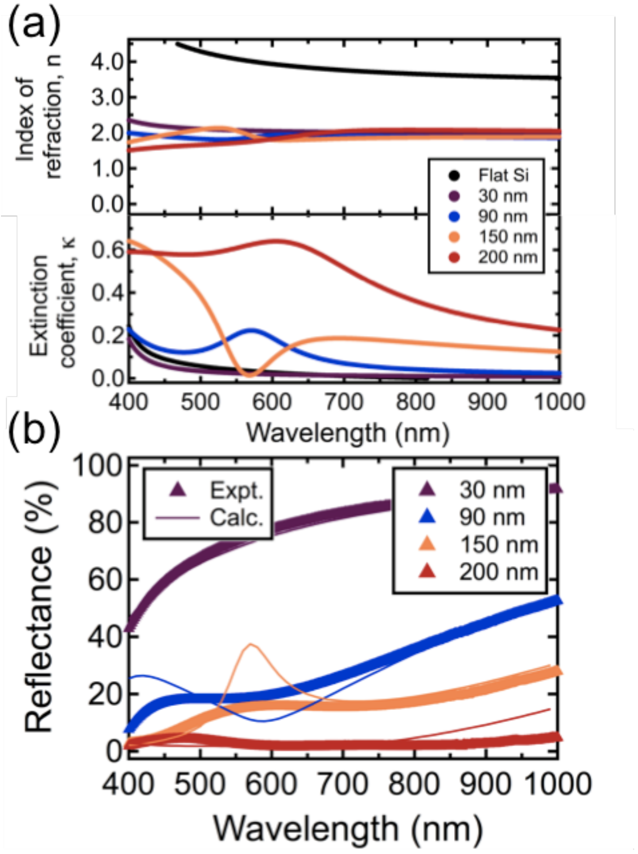

Figure 6.6: (a) Spectroscopic ellipsometry measurements of the real (n) and imaginary (k) parts of the refractive index ($n+ik$) for surface nanotextures of different heights. (b) Reflectance measurements (thick lines) and transfer matrix calculations (thin lines) (normalized to the flat substrate reflectance) versus wavelength for surface nanotextures with l = 50 nm and different heights.

height and 50 nm nearest neighbor separation (l) displays similar (lower) reflectance for both polarizations. The texture's deep subwavelength lateral separation minimizes any diffractive effects (i.e., $l < \lambda/2n$) such that the average reflectance of the nanostructured surface ($R \equiv ((s_{pol} + p_{pol}))/2$) remains less than 4% for angles as high as 60 degrees from normal. The surface nanotexture provides omnidirectional antireflection across a broad wavelength range. For example, at a 45 degree incident angle the average reflectance of s- and p-polarized light with wavelengths between 400 nm to 1 μm is <0.7% and <0.5%, respectively more than 10x smaller than that of flat silicon, which reflects an average of 26% and 12% of s- and p-polarized light in this range.

Textures with smaller feature sizes outperform the geometric model of

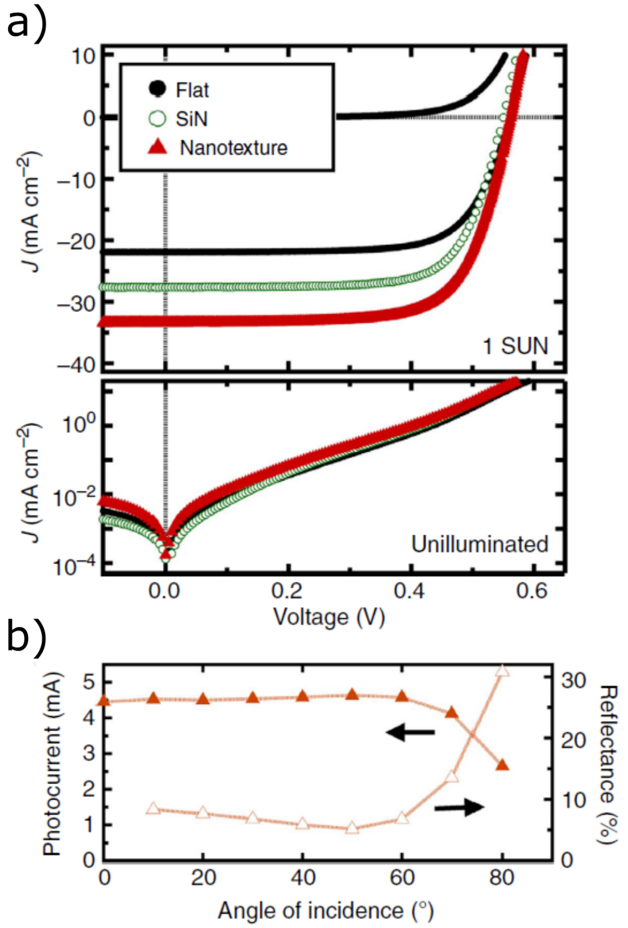

Figure 6.7: a) Illuminated (1 sun) and unilluminated current-voltage (J-V) characteristics of (black) flat silicon solar cell and similar cells coated with (green open circles) an 80-nm-thick silicon nitride antireflection coating and (red) a surface nanotexture. (b) Angular dependence of device photocurrent (solid red triangles) and reflectance (red open triangles) when illuminated with 632-nm light. Left and right arrows refer plotted data to the appropriate horizontal axes.

equation 6.5, needing <50% of the minimum height $t \sim 0.4x\lambda \sim 400nm$ to achieve average broadband reflectance of <1%. The required nanotexture height decreases linearly with l, shrinking to only ∼ 165nm for $l = 40$ nm. The largest textures we measured($l = 67$ nm) require a height of t = 440nm, similar to the value of 430nm for <1% average reflectance calculated using the transfer matrix method and consistent with the taller heights of other silicon moth eye structures with larger lateral dimensions.

Nevertheless, our transfer matrix method calculations of the reflectance of silicon nanotextures having an asymmetric, flared profile do not explain the measured values. However, the chlorine and bromine etch chemistries we use to generate the nanotextures are known to modify the silicon material properties within $\sim$ 10 nm of the surface, [218–220] which can substantially alter the material optical properties [221] and provide an additional mechanism for grading the refractive index between air and silicon beyond the geometry alone. Because our nanotextures consist of lateral feature sizes on the scale of 10 nm, even material modifications within 1 - 5 nm of the surface comprise a significant fraction of the total volume, and can thus substantially alter the effective index of the entire structure. We infer changes in nanotexture material properties by comparing spectroscopic ellipsometry measurements of the complex refractive index ($n + ik$) of a flat silicon surface to those of silicon nanotextures with l = 50 nm and increasing height (t) (Figure 6.6 a).

From these measurements, we surmise that the effective refractive index of the nanotextured layer results from not only the changing silicon volume fraction with depth, but also through material modification resulting from the etch process. While the measured n and k values for unetched silicon (Figure 6.6 a, black) agree with previously published values, the optical properties of the material comprising the etched nanotextures differ significantly from silicon (Figure 6.6 a). Our ellipsometry data are consistent with an abrupt decrease in the etched silicon nanostructure's n from 4 to $\sim$ 2 after even a short etch (Figure 6.6 a, upper graph), and a more gradual increase in k with increasing etch time (Figure 6.6 a, lower graph). Transfer matrix calculations of the reflectance of the nanotextured silicon interface (l = 50 nm) using both the measured geometric profile and the modified optical constants obtained from spectroscopic ellipsometry measurements more accurately describe the measured data for all nanotexture heights, capturing both the magnitude of the reflectance as well as the positions of optical resonances. In our model, we divide the nanotexture into discrete, 1 nm thick vertical slices and apply an effective medium approximation to each slice. These simulations provide a significantly improved description of the data as compared to a similar calculation using bulk silicon optical constants.

Applying the block copolymer-based surface nanotexture to a crystalline silicon solar cell improves the power conversion efficiency under simulated AM1.5G illumination from 8.3% to 12.6% (Figure 6.7 a). The broadband antireflection provided by the nanostructured surface increases the device current output. The short-circuit photocurrent (J_{sc}) improves from 24 mA/cm^2

to 35 mA/cm^2, a substantial increase of nearly ∼50% that slightly less than the ∼65% increase estimated from improved light coupling into the device from ∼60% to 99%. We understand this difference as stemming from reduced charge collection efficiency in the textured device, which manifests as both increased device dark current (J_0) and diode ideality factor (n). The magnitude of the dark current increase (from 10^{-3} mA/cm^2 to ∼10^{-2} mA/cm^2, Figure 6.7 b) is consistent with the 10x higher surface area due to the nanotexture. The simultaneous increase in n from 1.46 to ∼2 has the net effect of slightly increasing the nanotextured device open circuit voltage (V_{oc}). The silicon nitride antireflection coating slightly reduces both J_0 (to 10^{-3}mAcm^2) and n compared with both planar and nanotextured devices, which improves the device fill factor from 70 to 71%. Future studies will target understanding the passivation effects of the nanotextured interface and integration with higher-performance devices.

6.2.2 Spectroscopic Ellipsometry Models

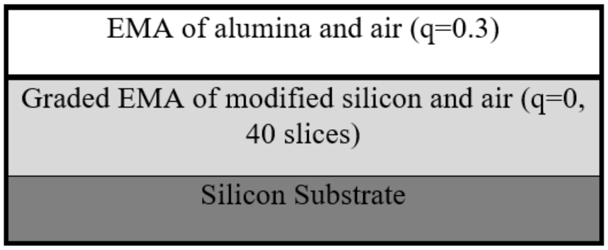

Figure 6.8: Schematic of the model used in the analysis of spectroscopic ellipsometry data from etched silicon samples.

The analysis of the ellipsometric data was done using the J. A. Woollam software, WVASE32 (version 3.770). First, the optical constants for the bare silicon substrates were obtained. The bare silicon films were modeled using two critical-point-parabolic-band (CPPB) oscillators, and a Drude model to describe the free carrier effects on the response of a dielectric. It was assumed that there is no anisotropy in the samples. The CPPB oscillator complex dielectric permittivity ϵ as a function of energy E is defined as:

$$\epsilon(E) = Ae^{i\theta}(B/(2E_n - 2E - iB))^{\mu} \tag{6.6}$$

where the amplitude is represented by a dimensionless quantity A, the phase projection factor by a dimensionless quantity θ, threshold energy by E_n (eV), broadening parameter B (eV), and the exponent μ. The CPPB oscillator energy positions for bare silicon were at 3.34 (eV), and at 4.31 (eV). The Drude model complex dielectric permittivity ϵ as a function of energy E is defined as:

$$\epsilon(E) = -(AB)/(E^2 + iB * E) \tag{6.7}$$

where the amplitude is given by A (eV), and the broadening by B (eV). A film with patterned alumina particles on bare silicon was then measured before any etching. The data was analysed using an effective medium approximation (EMA) of the optical constants of alumina and air/void. The depolarization factor q, which is governed by the shape of the material in the void was kept at 0.3. This is a simple linear combination of the pristine optical constants using the Bruggeman approach [58]. The resulting dielectric function ϵ for the mixture of two materials a and b is given by,

$$\epsilon = (\epsilon_a\epsilon_b + \kappa\epsilon_h(f_a\epsilon_a + f_b\epsilon_b))/(\kappa\epsilon_h + (f_a\epsilon_a + f_b\epsilon_b)) \tag{6.8}$$

where ϵ_a and ϵ_b are the complex dielectric constants of materials a and b repectively, and f_a and f_b are the volume fractions of the two materials. In the Bruggeman approach, $\kappa = 2$ and $\epsilon_h = \epsilon$. We constructed a model where the optical constants of the constituents were fixed and only the volume fraction and thickness of the layer was allowed to vary.

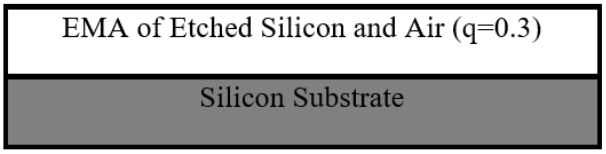

Figure 6.9: Schematic of the model used in the analysis of spectroscopic ellipsometry data from etched silicon samples.

Data from all samples with different etch times was collected using the same approach. Multiples spots on the sample were measured at different angles in the wavelength range of 210 nm and 1700 nm. A model was created where a graded effective medium approximation (EMA) of optical constants of modified silicon and air/void were varied using the geometrically calculated volume fraction:

$$f(z)_{silicon} = (\pi(r_{neck} + (z(p/2 - r_{neck}))/h)^2)/(2\sqrt{3}(p/2)^2) \tag{6.9}$$

The optical constants found from the bare silicon were allowed to vary to give the modified silicon optical constants. These were used in the EMA along with void to calculate the effective optical constants of the etched silicon pillars. The depolarization factor q, was held at zero in this EMA layer and the layer was split into 40 slices for each model. The modified silicon optical constants are held constant in each of the slices. The same model is also created for each of the different spots and angles the data was collected for and the modified optical constants are coupled in the models for all spots. The height of the silicon pillars gives the thickness of the EMA layer and this was found using scanning electron microscopy images of each of the samples and was held fixed in the model. A schematic of the model in given in Figure 6.8.

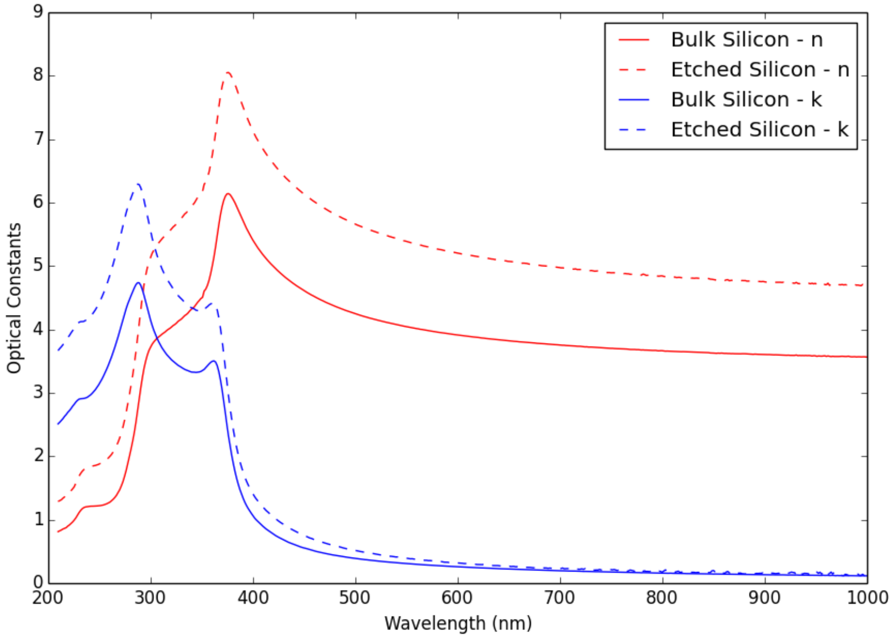

Figure 6.10: Complex refractive index for bulk and etched silicon (100s) for a flat Si wafer with no Al_2O_3 patterns applied to the surface prior to etch.

The bare silicon films were modeled using two critical-point-parabolic-band (CPPB) oscillators, and a Drude model to describe the free carrier effects on the response of a dielectric. It was assumed that there is no anisotropy in the samples. The CPPB oscillator complex dielectric permittivity ϵ as a function of energy E is defined as before:

$$\epsilon(E) = Ae^{i\theta}(B/(2E_n - 2E - iB))^{\mu} \tag{6.10}$$

The CPPB oscillator energy positions for bare silicon were at 3.34 (eV), and at 4.31 (eV). After modeling the bare silicon substrates, data was collected from the flat etched silicon samples. In this case, a flat Si substrate, with no Al_2O_3 nanopattern on the surface, The flat silicon was etched for a 100s. This experiment allows us to understand the effect of the etch process it self on the surface properties of the silicon. Previous studies of similar etch chemistries for silicon observed a significant modification of the surface optical properties due to etch-induced surface roughness/void fraction and material modification. Since the surface-area-to-volume ratio of the anti-reflective nanotextures is very high, any effect of the etch process on the silicon surface could have a significant effect on the optical properties of the nanotextured silicon. Data was taken at three different points on the sample and simultaneously fit assuming equivalent optical constants. The data was analyzed using an effective medium approximation (EMA) of the optical constants of etched silicon and air/void. This is done in order to model the roughness induced due to etching. The optical constants of the etched silicon were allowed to vary. The thickness of the etched part of silicon and the volume fraction of the void in the EMA layer were also allowed to vary. The depolarization factor q, which is governed by the shape of the material in the void was kept at 0.3. This is a simple linear combination of the pristine optical constants using the Bruggeman approach. The resulting dielectric function ϵ for the mixture of two materials a and b is given by Eq. 6.8.

The volume fraction of air in the EMA layer was found to be 25% and the thickness of the layer was found to be 4.75 nm. The optical constants are shown in Figure 6.10. These constants agree very well with previous studes of the etch-induced effects on Si optical constants from literature for etched silicon.

A uniqueness analysis on the volume fraction of the air, i.e., the void fraction, in the EMA was performed where the volume fraction of air was varied systematically from 0% to 100% and all other parameters were allowed to vary at every step. The mean squared error (MSE) was seen to be equally low for values between 0% and 62% after which the MSE increased dramatically, as shown in Fig. 6.11. The local minimum was found at 25% however the sensitivity to the volume void fraction is found to be low betwseen 0% and 62%. From this analysis, we can say that the void fraction in the top 4.5 nm of the surface is less than 62%, but we cannot quantify the void fraction with any more precision that that due to the insensitivity of the MSE to void fraction in the range 0%-62% seen in Fig. 6.11.

A separate model was also created as a consistency check for the 30s etched silicon pillars. Assuming the etched silicon forms a skin layer on top on the pure silicon, the the pillars can be modeled as a three component EMA of

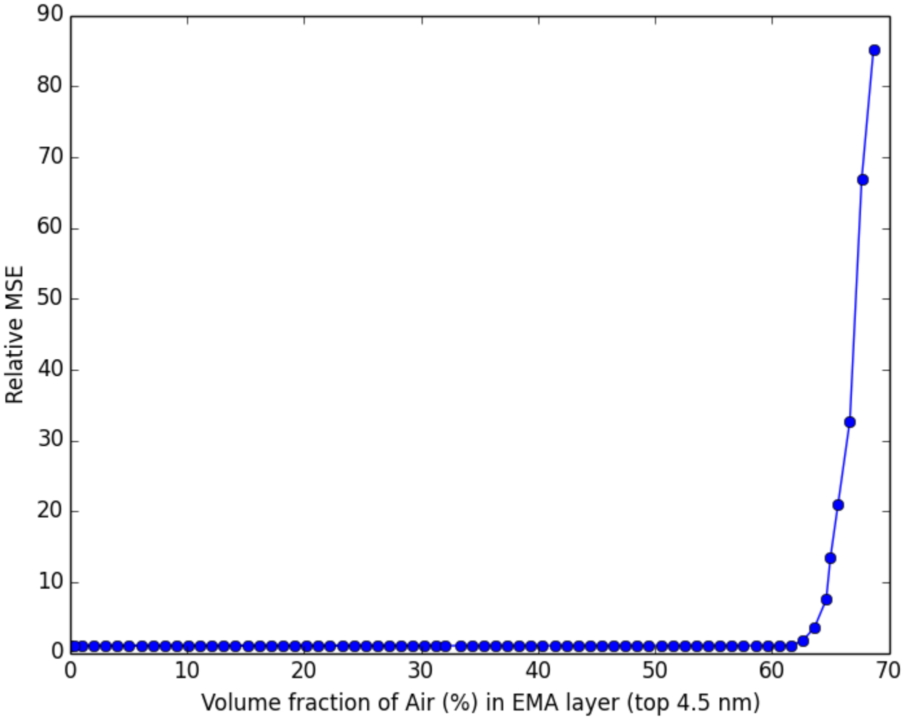

Figure 6.11: Relative MSE of the spectroscopic ellipsometry fit as a function of the air volume fraction.

pure silicon, an EMA consisting of etched silicon and void/air (EMA_{etch}), and air. A schematic of this is shown in Figure 6.12. The EMA_{etch} skin layer in this model is the same as the top layer in the flat etched silicon case described above.

The volume fraction for the EMA_{etch} skin layer and air is calculated using the geometrical equations described before. The 3-component EMA layer is split into 40 subslices. The thickness of the EMA_{etch} skin layer on the pure silicon is allowed to vary but is restricted to the radius of the top of the pillar. The volume fraction of air/void in the EMA_{etch} is also allowed to vary. The MSE is lowest when the volume fraction is calculated to be 65.9% and the thickness of the EMA_{etch} skin layer is 14nm. This result is consistent with the constraint on void fraction observed in Fig. 6.11 for an etched flat silicon wafer (surface layer of 4.5nm with <62% void fraction). The larger surface area exposed to the etch in the nanostructured case is expected to result in slightly larger void fraction and modified surface thickness compared to the flat wafer case. From this measurement, we plot the refractive index profile

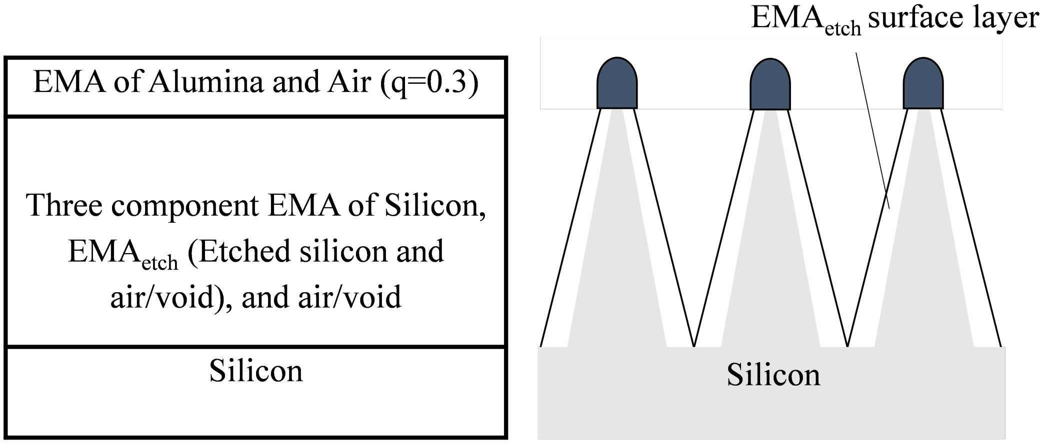

Figure 6.12: Schematic of the model used in the analysis of spectroscopic ellipsometry data from etched silicon samples with Al_2O_3 patterns applied to the surface prior to etch.

seen by incoming light in Fig. 6.13.

Due to the surface modification of the etch, even the base of the nanocone layer touching the silicon wafer does not have a refractive index as high as bulk silicon, resulting in the slight jump in refractive index at the nanocone/substrate interface. In this plot, we assume an abrupt beginning to bulk silicon optical constants, our measurements on etched flat silicon wafers suggest that in fact this transition occurs smoothly over a distance of about 5nm. The inset to Fig. 6.13 shows the effective index of the nanocones themselves, including the etch-modified surface layer, but not including the intermix with air between the cones. This shows that the effective index of the cones is significantly reduced to the effect of the etch-modified surface layer, and that the effect of the surface modification is larger near the top of the cone where the surface area-to-volume ratio is larger. The optical constants for the top and bottom most layer of the three component EMA calculated using this model are shown in Figure 6.13.

In nanotextures with larger dimensions, this surface layer is an inconsequential fraction of the total volume. However, because our nanotextures have lateral feature sizes on the scale of 10nm, even material modifications within a few nm of the surface comprise a significant volume fraction, and can thus substantially alter n of the entire structure.

In order to validate the surface modification of the nanotexture surface we treated the nanotextured silicon with a dilute (50:1) hydrofluoric acid:water mixture (buffered with NH_4F), which removes surface oxides. In addition to

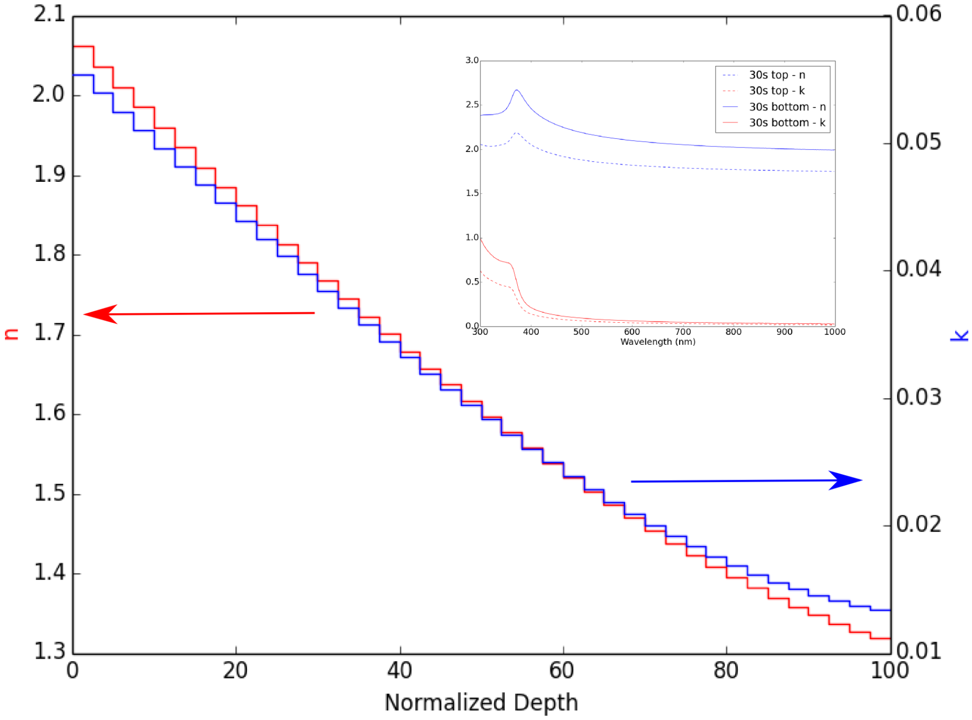

Figure 6.13: Optical constants for the 30s etched silicon pillar sample found using the model described in the Figure 6.12.

stripping the alumina caps, the etch narrows the texture radius by several nm, consistent with removal of a silicon oxide layer. X-ray photoelectron spectra of the nanotexture's Si 2p and O 1s core levels also display higher binding-energy peaks, consistent with those of a material previously identified as a porous, anodic silicon oxide [222] (XPS measurements were performed by collaborators).

Chapter 7

Conclusion

This work can be broadly broken down into three distinct sections: a) new understanding of inhomogeneity in material systems, b) development of new techniques for the measurement of spatial inhomogeneity, and c) development of new architectures taking advantage of nanoscale spatial inhomogeneity within materials. The key findings, open questions, and application areas from each of these subcategories can be found in Figure 7.1.

There are several open questions and future directions of this research. Within the first section, we primarily worked with a model organic material system. Although the work sheds light on the mechanism, we need to understand the effects of confinement on morphology for other polymers as they can be extremely sensitive to processing conditions and chemical structure. The crystallization of polymers is also affected by the presence of the fullerene in a BHJ. Although we found kinetic effects to be more important than the presence of the fullerene when the film is confined, this could vary for different polymers and needs further study.

Apart from organic photovoltaics, this work also deepens our understanding of organic bulk heterojunction systems and can be applied in areas such as photodetectors, organic light emitting diodes (OLEDs), and other organic optoelectric systems.

In CIGS PVs, some recent work has shown the existence of nanodomains of Cu-rich and Cu-poor regions within the grain [223] making an interconnected network of p and n-type material that may improve charge collection. The role of such nanodomains in the recombination mechanism presented in this thesis needs to be studied. Furthermore, as shown in Chapter 6 of this thesis, there is a gradation of sodium with depth in the active layer of CIGS. Although we did not find any correlation of sodium inhomogeneity (within grains) with recombination, the sodium could be aggregating on the grain boundaries. The effect of this on recombination and charge collection needs to be studied in more detail.

Although directly applicable to CIGS, this work also lends understanding to other polycrystalline semiconducting compounds. For example the results of this work can be used to help guide research in another promising candidate for large scale PVs, CdTe, which has similar properties.

In the second category of this thesis (of new techniques), in order to apply the μ-CELIV technique to other material systems, we need to model the current transient curve using a combination of the continuity, current, and Poisson equations for different material systems. Furthermore, we would also like to use the hyperspectral laser for illumination in the μ-CELIV technique as this would allow us to excite charges at different depths within the film giving us the ability to measure mobility in three dimensions (laterally and as a function of the depth of the thin-film). In the hyperspectral system, we can also use optical and electrical modeling to extend our current technique to measure quantities such as the back surface recombination and lifetime of charges in complicated structures such as silicon passivated emitter rear contact (PERC) solar cells considered as a promising low cost alternative to traditional c-Si based solar cells [161].

These new techniques can be used not only by researchers but also by industry professionals to understand the effect of mobility variations, and material deformations on performance metrics in PVs. These techniques can be used on a wide range of material systems and can be easily adjusted to be quicker for industry use in large area solar cells or made more accurate and higher resolution for lab scale measurements.

We also present the development of new architectures based on material inhomogeneity. Although we give a basic model for the strong and persistence n-doping of graphene, more work needs to be done to understand the exact mechanism of the doping. The form of sodium in SLG and the CIGS layer and its effect of doping strength also needs to be understood.

Strong and persistent n-doping of graphene open up a wide range of previously unexplored applications such as in microelectronics, photodetectors, photovoltaics, electrochemical energy storage systems, and sensors.

Finally, in the last section we also describe silicon nanotexturing for broadband antireflection. Although the optical properties for the surface layer were measured and understood to give enhanced antireflection, the exact composition and structure of this surface layer still needs to be understood. An extra phase can be seen in XPS measurements and still needs to be analyzed further.

The nanotexturing technique presented can also be applied to other substrates such as glass and plastics (kapton, polyimide, PET, and Teflon). This technique can be used for photovoltaics, energy storage systems, electronics products, military equipment, and automotive or aircraft windshields. Apart from providing broadband antireflection, the technique can also be used to provide hydrophobic surfaces with a high degree of water repellency.

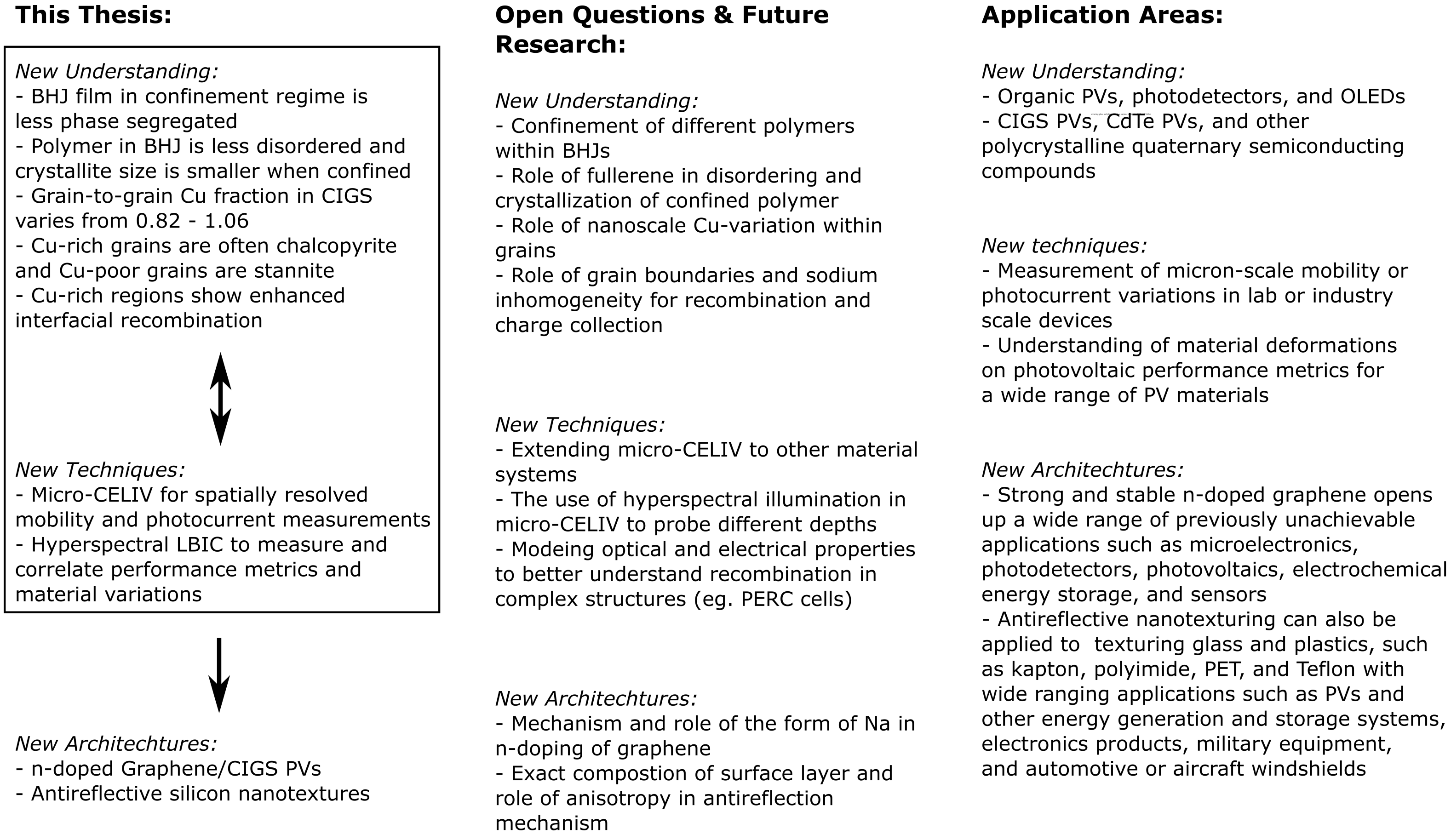

This Thesis:

New Understanding:
- BHJ film in confinement regime is less phase segregated
- Polymer in BHJ is less disordered and crystallite size is smaller when confined
- Grain-to-grain Cu fraction in CIGS varies from 0.82 - 1.06
- Cu-rich grains are often chalcopyrite and Cu-poor grains are stannite
- Cu-rich regions show enhanced interfacial recombination

↕

New Techniques:
- Micro-CELIV for spatially resolved mobility and photocurrent measurements
- Hyperspectral LBIC to measure and correlate performance metrics and material variations

↓

New Architechtures:
- n-doped Graphene/CIGS PVs
- Antireflective silicon nanotextures

Open Questions & Future Research:

New Understanding:
- Confinement of different polymers within BHJs
- Role of fullerene in disordering and crystallization of confined polymer
- Role of nanoscale Cu-variation within grains
- Role of grain boundaries and sodium inhomogeneity for recombination and charge collection

New Techniques:
- Extending micro-CELIV to other material systems
- The use of hyperspectral illumination in micro-CELIV to probe different depths
- Modeing optical and electrical properties to better understand recombination in complex structures (eg. PERC cells)

New Architechtures:
- Mechanism and role of the form of Na in n-doping of graphene
- Exact compostion of surface layer and role of anisotropy in antireflection mechanism

Application Areas:

New Understanding:
- Organic PVs, photodetectors, and OLEDs
- CIGS PVs, CdTe PVs, and other polycrystalline quaternary semiconducting compounds

New techniques:
- Measurement of micron-scale mobility or photocurrent variations in lab or industry scale devices
- Understanding of material deformations on photovoltaic performance metrics for a wide range of PV materials

New Architechtures:
- Strong and stable n-doped graphene opens up a wide range of previously unachievable applications such as microelectronics, photodetectors, photovoltaics, electrochemical energy storage, and sensors
- Antireflective nanotexturing can also be applied to texturing glass and plastics, such as kapton, polyimide, PET, and Teflon with wide ranging applications such as PVs and other energy generation and storage systems, electronics products, military equipment, and automotive or aircraft windshields

Figure 7.1: A concluding summary showing the key findings, open questions, future work, and applications areas of the research

Bibliography

[1] Intergovernmental Panel on Climate Change. *Climate Change 2007 - Impacts, Adaptation and Vulnerability.* Cambridge University Press, 2008. ISBN 0521880106. URL `http://www.ebook.de/de/product/6732679/intergovernmental_panel_on_climate_change_climate_change_2007_impacts_adaptation_and_vulnerability.html`.

[2] A. Cho. Energy's tricky tradeoffs. *Science*, 329(5993):786–787, aug 2010. doi: 10.1126/science.329.5993.786. URL `http://dx.doi.org/10.1126/science.329.5993.786`.

[3] Anthony Lopez, Billy Roberts, Donna Heimiller, Nate Blair, and Gian Porro. Us renewable energy technical potentials: A gis-based analysis. Technical report, NREL, 2012.

[4] European Comission. World energy technology outlook to 2050. Technical report, 2013.

[5] Martin A Green. Solar cells: operating principles, technology, and system applications. 1982.

[6] William Grylls Adams and RE Day. The action of light on selenium. *Proceedings of the Royal Society of London*, 25(171-178):113–117, 1876.

[7] Charles E Fritts. On a new form of selenium cell, and some electrical discoveries made by its use. *American Journal of Science*, (156):465–472, 1883.

[8] Daryl M Chapin, CS Fuller, and GL Pearson. A new silicon p-n junction photocell for converting solar radiation into electrical power. *Journal of Applied Physics*, (25):676–677, 1954.

[9] Jenny Nelson. *The physics of solar cells*, volume 1. World Scientific, 2003.

[10] D Eo Carlson and CR Wronski. Amorphous silicon solar cell. *Applied Physics Letters*, 28(11):671–673, 1976.

[11] RC Chittick, JH Alexander, and HF Sterling. The preparation and properties of amorphous silicon. *Journal of the Electrochemical Society*, 116(1):77–81, 1969.

[12] LL Kazmerski, FR White, and GK Morgan. Thin-film cuinse2/cds heterojunction solar cells. *Applied Physics Letters*, 29(4):268–270, 1976.

[13] R Farchioni and G Grosso. Organic electronic materials. *Springer Ser. Mater. Sci*, 41, 2001.

[14] C K Chiang, CR Fincher Jr, YW Park, AJ Heeger, H Shirakawa, EJ Louis, SC Gau, and Alan G MacDiarmid. Electrical conductivity in doped polyacetylene. *Physical Review Letters*, 39(17):1098, 1977.

[15] KG Amal and F Tom. Merocynanine organic solar cells. *Journal of Applied Physics*, 49:5982–5989, 1978.

[16] Ching W Tang. Two-layer organic photovoltaic cell. *Applied Physics Letters*, 48(2):183–185, 1986.

[17] NS Sariciftci, L Smilowitz, Alan J Heeger, F Wudl, et al. Photoinduced electron transfer from a conducting polymer to buckminsterfullerene. *Science*, 258(5087):1474–1476, 1992.

[18] NS Sariciftci, David Braun, C Zhang, VI Srdanov, AJ Heeger, G Stucky, and F Wudl. Semiconducting polymer-buckminsterfullerene heterojunctions: Diodes, photodiodes, and photovoltaic cells. *Applied physics letters*, 62(6):585–587, 1993.

[19] G. Yu, J. Gao, J. C. Hummelen, F. Wudl, and A. J. Heeger. Polymer photovoltaic cells: Enhanced efficiencies via a network of internal donor-acceptor heterojunctions. *Science*, 270(5243):1789–1791, Dec 1995. doi: 10.1126/science.270.5243.1789. URL `http://dx.doi.org/10.1126/science.270.5243.1789`.

[20] Neil W Ashcroft, N David Mermin, and Sergio Rodriguez. Solid state physics. *American Journal of Physics*, 46(1):116–117, 1978.

[21] ISO Standard. 9845-1: 1992. *Solar energy-Reference solar spectral irradiance at the ground at different receiving conditions-Part*, 1.

[22] Riccardo Farchioni and Giuseppe Grosso. *Organic electronic materials: conjugated polymers and low molecular weight organic solids*, volume 41. Springer Science & Business Media, 2013.

[23] K. Jarrendahl and H. Arwin. Multiple sample analysis of spectroscopic ellipsometry data of semi-transparent films. *Thin Solid Films*, 313-314: 114–118, February 1998. doi: 10.1016/S0040-6090(97)00781-5.

[24] Ernst Meyer. Atomic force microscopy. *Progress in surface science*, 41 (1):3–49, 1992.

[25] Hiroyuki Fujiwara. *Spectroscopic Ellipsometry: Principles and Applications*. Wiley, 2007. ISBN 0470016086. URL `http://www.amazon.com/Spectroscopic-Ellipsometry-Applications-Hiroyuki-Fujiwara/dp/0470016086%3FSubscriptionId%3D0JYN1NVW651KCA56C102%26tag%3Dtechkie-20%26linkCode%3Dxm2%26camp%3D2025%26creative%3D165953%26creativeASIN%3D0470016086`.

[26] Harland Tompkins and Eugene A Irene. *Handbook of Ellipsometry (Materials Science and Process Technology)*. William Andrew, 2006. ISBN 0815514999. URL `http://www.amazon.com/Handbook-Ellipsometry-Materials-Science-Technology/dp/0815514999%3FSubscriptionId%3D0JYN1NVW651KCA56C102%26tag%3Dtechkie-20%26linkCode%3Dxm2%26camp%3D2025%26creative%3D165953%26creativeASIN%3D0815514999`.

[27] A. C. Arias, N. Corcoran, M. Banach, R. H. Friend, J. D. MacKenzie, and W. T. S. Huck. Vertically segregated polymer-blend photovoltaic thin-film structures through surface-mediated solution processing. *Applied Physics Letters*, 80(10):1695, 2002. doi: 10.1063/1.1456550. URL `http://dx.doi.org/10.1063/1.1456550`.

[28] David S. Germack, Calvin K. Chan, R. Joseph Kline, Daniel A. Fischer, David J. Gundlach, Michael F. Toney, Lee J. Richter, and Dean M. DeLongchamp. Interfacial segregation in polymer/fullerene blend films for photovoltaic devices. *Macromolecules*, 43(8):3828–3836, Apr 2010. doi: 10.1021/ma100027b. URL `http://dx.doi.org/10.1021/ma100027b`.

[29] Gang Li, Vishal Shrotriya, Jinsong Huang, Yan Yao, Tom Moriarty, Keith Emery, and Yang Yang. High-efficiency solution processable polymer photovoltaic cells by self-organization of polymer blends. *Nature Materials*, 4(11):864–868, Oct 2005. doi: 10.1038/nmat1500. URL `http://dx.doi.org/10.1038/nmat1500`.

[30] Ananth Indrakanti, Ronald L Jones, and Sanat K Kumar. Do "nonequilibrium" effects control strong surface segregation from polymer blends? *Macromolecules*, 37(1):9–12, 2004. URL `http://pubs.acs.org/doi/pdf/10.1021/ma035010%2B`.

[31] Ronald L Jones, Ananth Indrakanti, Robert M Briber, Marcus Muller, and Sanat K Kumar. Phase behavior of ultrathin polymer mixtures. *Macromolecules*, 37(18):6676–6679, 2004. URL `http://pubs.acs.org/doi/pdf/10.1021/ma049108f`.

[32] Christopher L. Soles, Jack F. Douglas, Wen-li Wu, and Robert M. Dimeo. Incoherent neutron scattering as a probe of the dynamics in molecularly thin polymer films. *Macromolecules*, 36(2):373–379, Jan 2003. doi: 10.1021/ma020952k. URL `http://dx.doi.org/10.1021/ma020952k`.

[33] Christopher L. Soles, Eric K. Lin, Joseph L. Lenhart, Ronald L. Jones, Wen-li Wu, Dario L. Goldfarb, and Marie Angelopoulos. Thin film confinement effects on the thermal properties of model photoresist polymers. *Journal of Vacuum Science & Technology B: Microelectronics and Nanometer Structures*, 19(6):2690, 2001. doi: 10.1116/1.1415502. URL `http://dx.doi.org/10.1116/1.1415502`.

[34] Dario L. Goldfarb, Marie Angelopoulos, Eric K. Lin, Ronald L. Jones, Christopher L. Soles, Joseph L. Lenhart, and Wen-li Wu. Confinement effects on the spatial extent of the reaction front in ultrathin chemically amplified photoresists. *Journal of Vacuum Science & Technology B: Microelectronics and Nanometer Structures*, 19(6):2699, 2001. doi: 10.1116/1.1421559. URL `http://dx.doi.org/10.1116/1.1421559`.

[35] Mao-Yuan Chiu, U-Ser Jeng, Chiu-Hun Su, Keng S. Liang, and Kung-Hwa Wei. Simultaneous use of small- and wide-angle x-ray techniques to analyze nanometerscale phase separation in polymer heterojunction solar cells. *Advanced Materials*, 20(13):2573–2578, Jul 2008. doi: 10.1002/adma.200703097. URL `http://dx.doi.org/10.1002/adma.200703097`.

[36] Jonathan E. Allen, Kevin G. Yager, Htay Hlaing, Chang-Yong Nam, Benjamin M. Ocko, and Charles T. Black. Enhanced charge collection in confined bulk heterojunction organic solar cells. *Applied Physics Letters*, 99(16):163301, 2011. doi: 10.1063/1.3651509. URL `http://dx.doi.org/10.1063/1.3651509`.

[37] Wei Chen, Maxim P. Nikiforov, and Seth B. Darling. Morphology characterization in organic and hybrid solar cells. *Energy & Environmental Science*, 5(8):8045, 2012. doi: 10.1039/c2ee22056c. URL `http://dx.doi.org/10.1039/c2ee22056c`.

[38] Romain Stalder, Caroline Grand, Jegadesan Subbiah, Franky So, and John R. Reynolds. An isoindigo and dithieno[3,2-b:2',3'-d]silole copolymer for polymer solar cells. *Polymer Chemistry*, 3(1):89, 2011. doi: 10.1039/c1py00402f. URL `http://dx.doi.org/10.1039/c1py00402f`.

[39] Zach Beiley, Andrea Bowring, and Michael D. McGehee. *Modeling low-cost hybrid tandem photovoltaics with power conversion efficiencies exceeding 20 percent*, pages 003129–003130. Institute of Electrical and Electronics Engineers, Jun 2012. ISBN 978-1-4673-0066-7. doi: 10.1109/PVSC.2012.6318242. URL `http://dx.doi.org/10.1109/PVSC.2012.6318242`.

[40] A Mayer, S Scully, B Hardin, M Rowell, and M. D McGehee. Polymer-based solar cells. *Materials Today*, 10(11):28–33, Nov 2007. doi: 10.1016/S1369-7021(07)70276-6. URL `http://dx.doi.org/10.1016/S1369-7021(07)70276-6`.

[41] Yutong Pang, Nanditha Dissanayake, and Matthew D. Eisaman. *Guided-mode absorption in ultrathin organic photovoltaics*, pages 003131–003136. Institute of Electrical and Electronics Engineers, Jun 2012. ISBN 978-1-4673-0066-7. doi: 10.1109/PVSC.2012.6318243. URL `http://dx.doi.org/10.1109/PVSC.2012.6318243`.

[42] Vivian E. Ferry, Marc A. Verschuuren, Hongbo B. T. Li, Ewold Verhagen, Robert J. Walters, Ruud E. I. Schropp, Harry A. Atwater, and Albert Polman. Light trapping in ultrathin plasmonic solar cells. *Optics Express*, 18(S2):A237, Jun 2010. doi: 10.1364/OE.18.00A237. URL `http://dx.doi.org/10.1364/OE.18.00A237`.

[43] Martin A Green. Enhanced evanescent mode light trapping in organic solar cells and other low index optoelectronic devices. *Progress in Photovoltaics: Research and Applications*, 19(4):473–477, Jun 2011. doi: 10.1002/pip.1038. URL `http://dx.doi.org/10.1002/pip.1038`.

[44] Robert Norwood, Palash Gangopadhay, and Shiva Shahin. Ultra-thin organic photovoltaics with increased efficiency. *SPIE Newsroom*, Dec 2012. doi: 10.1117/2.1201212.004593. URL `http://dx.doi.org/10.1117/2.1201212.004593`.

[45] Peter N. Saeta, Vivian E. Ferry, Domenico Pacifici, Jeremy N. Munday, and Harry A. Atwater. How much can guided modes enhance absorption in thin solar cells? *Optics Express*, 17(23):20975, Nov 2009. doi: 10.1364/OE.17.020975. URL http://dx.doi.org/10.1364/OE.17.020975.

[46] Shiva Shahin, Palash Gangopadhyay, and Robert A. Norwood. Ultrathin organic bulk heterojunction solar cells: Plasmon enhanced performance using au nanoparticles. *Applied Physics Letters*, 101(5):053109, 2012. doi: 10.1063/1.4739519. URL http://dx.doi.org/10.1063/1.4739519.

[47] Z. Yu, A. Raman, and S. Fan. Fundamental limit of nanophotonic light trapping in solar cells. *Proceedings of the National Academy of Sciences*, 107(41):17491–17496, Oct 2010. doi: 10.1073/pnas.1008296107. URL http://dx.doi.org/10.1073/pnas.1008296107.

[48] Brian A. Collins, Zhe Li, John R. Tumbleston, Eliot Gann, Christopher R. McNeill, and Harald Ade. Absolute measurement of domain composition and nanoscale size distribution explains performance in ptb7:pc71bm solar cells. *Advanced Energy Materials*, 3(1):65–74, Jan 2013. doi: 10.1002/aenm.201200377. URL http://dx.doi.org/10.1002/aenm.201200377.

[49] Gang Li, Vishal Shrotriya, Jinsong Huang, Yan Yao, Tom Moriarty, Keith Emery, and Yang Yang. High-efficiency solution processable polymer photovoltaic cells by self-organization of polymer blends. *Nature Materials*, 4:864 – 868, 2005.

[50] M. Campoy-Quiles, J. Nelson, P. G. Etchegoin, D. D. C. Bradley, V. Zhokhavets, G. Gobsch, H. Vaughan, A. Monkman, O. Ingnas, N. K. Persson, and et al. On the determination of anisotropy in polymer thin films: A comparative study of optical techniques. *physica status solidi (c)*, 5(5):1270–1273, May 2008. doi: 10.1002/pssc.200777835. URL http://dx.doi.org/10.1002/pssc.200777835.

[51] P.G. Karagiannidis, D. Georgiou, C. Pitsalidis, A. Laskarakis, and S. Logothetidis. Evolution of vertical phase separation in p3ht:pcbm thin films induced by thermal annealing. *Materials Chemistry and Physics*, 129(3):1207–1213, Oct 2011. doi: 10.1016/j.matchemphys.2011.06.007. URL http://dx.doi.org/10.1016/j.matchemphys.2011.06.007.

[52] Uladzimir Zhokhavets, Tobias Erb, Gerhard Gobsch, Maher Al-Ibrahim, and Oliver Ambacher. Relation between absorption and crystallinity of poly(3-hexylthiophene)/fullerene films for plastic solar cells. *Chemical Physics Letters*, 418(4-6):347–350, Feb 2006. doi: 10.1016/j.cplett.2005.11.020. URL http://dx.doi.org/10.1016/j.cplett.2005.11.020.

[53] Sebastian Engmann, Vida Turkovic, Paul Denner, Harald Hoppe, and Gerhard Gobsch. Optical order of the polymer phase within polymer/fullerene blend films. *Journal of Polymer Science Part B: Polymer Physics*, 50(19):1363–1373, Oct 2012. doi: 10.1002/polb.23131. URL http://dx.doi.org/10.1002/polb.23131.

[54] Michael D. Bertolucci Daniel C. Harris. *Symmetry and Spectroscopy: An Introduction to Vibrational and Electronic Spectroscopy*. Courier Dover Publications, illustrated, unabridged, reprint edition, 1978.

[55] G. E. Jellison and F. A. Modine. Parameterization of the optical functions of amorphous materials in the interband region. *Applied Physics Letters*, 69(3):371, 1996. doi: 10.1063/1.118064. URL http://dx.doi.org/10.1063/1.118064.

[56] M. Kelly, P. Etchegoin, D. Fuchs, W. Kratschmer, and K. Fostiropoulos. Optical transitions of c60 films in the visible and ultraviolet from spectroscopic ellipsometry. *Physical Review B*, 46(8):4963–4968, Aug 1992. doi: 10.1103/PhysRevB.46.4963. URL http://dx.doi.org/10.1103/PhysRevB.46.4963.

[57] W. Richter and J. F. McGilp. Optical in situ surface control during movpe and MBE growth [and discussion]. *Philosophical Transactions of the Royal Society A: Mathematical, Physical and Engineering Sciences*, 344(1673):453–467, Sep 1993. doi: 10.1098/rsta.1993.0100. URL http://dx.doi.org/10.1098/rsta.1993.0100.

[58] D. A. G. Bruggeman. Berechnung verschiedener physikalischer konstanten von heterogenen substanzen. i. dielektrizittskonstanten und leitfhigkeiten der mischkrper aus isotropen substanzen. *Annalen der Physik*, 416(7):636–664, 1935. doi: 10.1002/andp.19354160705. URL http://dx.doi.org/10.1002/andp.19354160705.

[59] Jonathan W. Kiel, Brian J. Kirby, Charles F. Majkrzak, Brian B. Maranville, and Michael E. Mackay. Nanoparticle concentration profile in polymer-based solar cells. *Soft Matter*, 6(3):641, 2010. doi: 10.1039/b920979d. URL http://dx.doi.org/10.1039/b920979d.

[60] Akiko Orimo, Kohji Masuda, Satoshi Honda, Hiroaki Benten, Shinzaburo Ito, Hideo Ohkita, and Hiroshi Tsuji. Surface segregation at the aluminum interface of poly(3-hexylthiophene)/fullerene solar cells. *Applied Physics Letters*, 96(4):043305, 2010. doi: 10.1063/1.3294290. URL http://dx.doi.org/10.1063/1.3294290.

[61] Wichard J. D. Beenken and Tnu Pullerits. Spectroscopic units in conjugated polymers: A quantum chemically founded concept? *The Journal of Physical Chemistry B*, 108(20):6164–6169, 2004. doi: 10.1021/jp037332l. URL http://pubs.acs.org/doi/abs/10.1021/jp037332l. PMID: 18950096.

[62] Mariano Campoy-Quiles, Toby Ferenczi, Tiziano Agostinelli, Pablo G. Etchegoin, Youngkyoo Kim, Thomas D. Anthopoulos, Paul N. Stavrinou, Donal D. C. Bradley, and Jenny Nelson. Morphology evolution via self-organization and lateral and vertical diffusion in polymer:fullerene solar cell blends. *Nature Materials*, 7(2):158–164, Jan 2008. doi: 10.1038/nmat2102. URL http://dx.doi.org/10.1038/nmat2102.

[63] Samuele Lilliu, Tiziano Agostinelli, Ellis Pires, Mark Hampton, Jenny Nelson, and J. Emyr Macdonald. Dynamics of crystallization and disorder during annealing of p3ht/PCBm bulk heterojunctions. *Macromolecules*, 44(8):2725–2734, Apr 2011. doi: 10.1021/ma102817z. URL http://dx.doi.org/10.1021/ma102817z.

[64] Frank C. Spano. Modeling disorder in polymer aggregates: The optical spectroscopy of regioregular poly(3-hexylthiophene) thin films. *The Journal of Chemical Physics*, 122(23):234701, 2005. doi: 10.1063/1.1914768. URL http://dx.doi.org/10.1063/1.1914768.

[65] Jenny Clark, Carlos Silva, Richard Friend, and Frank Spano. Role of intermolecular coupling in the photophysics of disordered organic semiconductors: Aggregate emission in regioregular polythiophene. *Physical Review Letters*, 98(20), May 2007. doi: 10.1103/PhysRevLett.98.206406. URL http://dx.doi.org/10.1103/PhysRevLett.98.206406.

[66] Guy Louarn, Miroslaw Trznadel, J. P. Buisson, Jadwiga Laska, Adam Pron, Mieczyslaw Lapkowski, and Serge Lefrant. Raman spectroscopic studies of regioregular poly(3-alkylthiophenes). *The Journal of Physical Chemistry*, 100(30):12532–12539, Jan 1996. doi: 10.1021/jp960104p. URL http://dx.doi.org/10.1021/jp960104p.

[67] Jenny Clark, Jui-Fen Chang, Frank C. Spano, Richard H. Friend, and Carlos Silva. Determining exciton bandwidth and film microstructure in polythiophene films using linear absorption spectroscopy. *Applied Physics Letters*, 94(16):163306, 2009. doi: 10.1063/1.3110904. URL `http://dx.doi.org/10.1063/1.3110904`.

[68] D. Beljonne, J. Cornil, R. Silbey, P. Millir, and J. L. Bredas. Interchain interactions in conjugated materials: The exciton model versus the supermolecular approach. *The Journal of Chemical Physics*, 112(10):4749, 2000. doi: 10.1063/1.481031. URL `http://dx.doi.org/10.1063/1.481031`.

[69] Eric S. Manas and Frank C. Spano. Absorption and spontaneous emission in aggregates of conjugated polymers. *The Journal of Chemical Physics*, 109(18):8087, 1998. doi: 10.1063/1.477457. URL `http://dx.doi.org/10.1063/1.477457`.

[70] Siddharth Joshi, Souren Grigorian, Ullrich Pietsch, Patrick Pingel, Achmad Zen, Dieter Neher, and Ullrich Scherf. Thickness dependence of the crystalline structure and hole mobility in thin films of low molecular weight poly(3-hexylthiophene). *Macromolecules*, 41(18): 6800–6808, Sep 2008. ISSN 1520-5835. doi: 10.1021/ma702802x. URL `http://dx.doi.org/10.1021/ma702802x`.

[71] Scott Himmelberger, Javier Dacuna, Jonathan Rivnay, Leslie H. Jimison, Thomas McCarthy-Ward, Martin Heeney, Iain McCulloch, Michael F. Toney, and Alberto Salleo. Effects of confinement on microstructure and charge transport in high performance semicrystalline polymer semiconductors. *Adv. Funct. Mater.*, 23(16):2091–2098, Nov 2012. ISSN 1616-301X. doi: 10.1002/adfm.201202408. URL `http://dx.doi.org/10.1002/adfm.201202408`.

[72] Duc T. Duong, Michael F. Toney, and Alberto Salleo. Role of confinement and aggregation in charge transport in semicrystalline polythiophene thin films. *Phys. Rev. B*, 86(20):205205, Nov 2012. ISSN 1550-235X. doi: 10.1103/physrevb.86.205205. URL `http://dx.doi.org/10.1103/PhysRevB.86.205205`.

[73] Leslie H. Jimison, Scott Himmelberger, Duc T. Duong, Jonathan Rivnay, Michael F. Toney, and Alberto Salleo. Vertical confinement and interface effects on the microstructure and charge transport of p3ht thin films.

J. Polym. Sci. B Polym. Phys., 51(7):611–620, Feb 2013. ISSN 0887-6266. doi: 10.1002/polb.23265. URL http://dx.doi.org/10.1002/polb.23265.

[74] Stefan C. B. Mannsfeld, Ajay Virkar, Colin Reese, Michael F. Toney, and Zhenan Bao. Precise structure of pentacene monolayers on amorphous silicon oxide and relation to charge transport. *Advanced Materials*, 21(22):2294–2298, Jun 2009. ISSN 1521-4095. doi: 10.1002/adma.200803328. URL http://dx.doi.org/10.1002/adma.200803328.

[75] Ahsan Ashraf, D. M. Nanditha M. Dissanayake, David S. Germack, Conan Weiland, and Matthew D. Eisaman. Confinement-induced reduction in phase segregation and interchain disorder in bulk heterojunction films. *ACS Nano*, 8(1):323–331, Jan 2014. ISSN 1936-086X. doi: 10.1021/nn404172m. URL http://dx.doi.org/10.1021/nn404172m.

[76] Wei-Ru Wu, U-Ser Jeng, Chun-Jen Su, Kung-Hwa Wei, Ming-Shin Su, Mao-Yuan Chiu, Chun-Yu Chen, Wen-Bin Su, Chiu-Hun Su, and An-Chung Su. Competition between fullerene aggregation and poly(3-hexylthiophene) crystallization upon annealing of bulk heterojunction solar cells. *ACS Nano*, 5(8):6233–6243, Aug 2011. ISSN 1936-086X. doi: 10.1021/nn2010816. URL http://dx.doi.org/10.1021/nn2010816.

[77] R. Joseph Kline, Michael D. McGehee, and Michael F. Toney. Highly oriented crystals at the buried interface in polythiophene thin-film transistors. *Nature Materials*, 5(3):222–228, Feb 2006. doi: 10.1038/nmat1590. URL http://dx.doi.org/10.1038/nmat1590.

[78] Peter Peumans, Aharon Yakimov, and Stephen R. Forrest. Small molecular weight organic thin-film photodetectors and solar cells. *Journal of Applied Physics*, 93(7):3693, 2003. ISSN 0021-8979. doi: 10.1063/1.1534621. URL http://dx.doi.org/10.1063/1.1534621.

[79] D. M. Nanditha M. Dissanayake, Ahsan Ashraf, Yutong Pang, and Matthew D. Eisaman. Mapping spatially resolved charge collection probability within p3ht:pcbm bulk heterojunction photovoltaics. *Adv. Energy Mater.*, 4(2), Jan 2014. ISSN 1614-6832. doi: 10.1002/aenm.201300525. URL http://dx.doi.org/10.1002/aenm.201300525.

[80] M. Brinkmann and P. Rannou. Effect of molecular weight on the structure and morphology of oriented thin films of regioregular poly(3-hexylthiophene) grown by directional epitaxial solidification. *Adv. Funct.*

Mater., 17(1):101–108, Jan 2007. ISSN 1616-3028. doi: 10.1002/adfm.200600673. URL http://dx.doi.org/10.1002/adfm.200600673.

[81] Ian M. Craig, Christopher J. Tassone, Sarah H. Tolbert, and Benjamin J. Schwartz. Second-harmonic generation in conjugated polymer films: A sensitive probe of how bulk polymer crystallinity changes with spin speed. *The Journal of Chemical Physics*, 133(4):044901, 2010. ISSN 0021-9606. doi: 10.1063/1.3436517. URL http://dx.doi.org/10.1063/1.3436517.

[82] Detlef-M. Smilgies. Scherrer grain-size analysis adapted to grazing-incidence scattering with area detectors. *J Appl Cryst*, 42(6):1030–1034, Dec 2009. ISSN 1600-5767. doi: 10.1107/s0021889809040126. URL http://dx.doi.org/10.1107/S0021889809040126.

[83] H. Yang, T. J. Shin, L. Yang, K. Cho, C. Y. Ryu, and Z. Bao. Effect of mesoscale crystalline structure on the field-effect mobility of regioregular poly(3-hexyl thiophene) in thin-film transistors. *Adv. Funct. Mater.*, 15 (4):671–676, Apr 2005. ISSN 1616-3028. doi: 10.1002/adfm.200400297. URL http://dx.doi.org/10.1002/adfm.200400297.

[84] H. Sirringhaus, P. J. Brown, R. H. Friend, M. M. Nielsen, K. Bechgaard, B. M. W. Langeveld-Voss, A. J. H. Spiering, R. A. J. Janssen, E. W. Meijer, P. Herwig, and et al. Two-dimensional charge transport in self-organized, high-mobility conjugated polymers. *Nature*, 401(6754):685–688, Oct 1999. ISSN 0028-0836. doi: 10.1038/44359. URL http://dx.doi.org/10.1038/44359.

[85] P. G. Gennes and J. Prost. *The Physics of Liquid Crystals (International Series of Monographs on Physics)*, volume 10. Oxford University Press: New York,, 2nd edition, 1993.

[86] Pere Bruna, Daniel Crespo, Ricard Gonzalez-Cinca, and Eloi Pineda. On the validity of avrami formalism in primary crystallization. *Journal of Applied Physics*, 100(5):054907, 2006. ISSN 0021-8979. doi: 10.1063/1.2337407. URL http://dx.doi.org/10.1063/1.2337407.

[87] Ryan C. Nieuwendaal, Hyun Wook Ro, David S. Germack, R. Joseph Kline, Michael F. Toney, Calvin K. Chan, Amit Agrawal, David Gundlach, David L. VanderHart, and Dean M. Delongchamp. Measuring domain sizes and compositional heterogeneities in p3ht-PCBm bulk heterojunction thin films with 1h spin diffusion nmr spectroscopy. *Adv. Funct.*

Mater., 22(6):1255–1266, Mar 2012. ISSN 1616-301X. doi: 10.1002/adfm.201102138. URL http://dx.doi.org/10.1002/adfm.201102138.

[88] D. H. Kim, Y. D. Park, Y. Jang, H. Yang, Y. H. Kim, J. I. Han, D. G. Moon, S. Park, T. Chang, C. Chang, and et al. Enhancement of field-effect mobility due to surface-mediated molecular ordering in regioregular polythiophene thin film transistors. *Adv. Funct. Mater.*, 15(1):77–82, Jan 2005. ISSN 1616-3028. doi: 10.1002/adfm.200400054. URL http://dx.doi.org/10.1002/adfm.200400054.

[89] Chih-Ming Liu, Ming-Shin Su, Jian-Ming Jiang, Yu-Wei Su, Chun-Jen Su, Charn-Ying Chen, Cheng-Si Tsao, and Kung-Hwa Wei. Distribution of crystalline polymer and fullerene clusters in both horizontal and vertical directions of high-efficiency bulk heterojunction solar cells. *ACS Appl. Mater. Interfaces*, 5(12):5413–5422, jun 2013. doi: 10.1021/am4011995. URL http://dx.doi.org/10.1021/am4011995.

[90] Minh Trung Dang, Lionel Hirsch, Guillaume Wantz, and James D. Wuest. Controlling the morphology and performance of bulk heterojunctions in solar cells. lessons learned from the benchmark poly(3-hexylthiophene):[6,6]-phenyl-c 61 -butyric acid methyl ester system. *Chemical Reviews*, 113(5):3734–3765, may 2013. doi: 10.1021/cr300005u. URL http://dx.doi.org/10.1021/cr300005u.

[91] Susanne Siebentritt. What limits the efficiency of chalcopyrite solar cells? *Solar Energy Materials and Solar Cells*, 95(6):1471–1476, Jun 2011. ISSN 0927-0248. doi: 10.1016/j.solmat.2010.12.014. URL http://dx.doi.org/10.1016/j.solmat.2010.12.014.

[92] Philip Jackson, Dimitrios Hariskos, Roland Wuerz, Oliver Kiowski, Andreas Bauer, Theresa Magorian Friedlmeier, and Michael Powalla. Properties of cu(in,ga)se 2 solar cells with new record efficiencies up to 21.7 *physica status solidi (RRL) - Rapid Research Letters*, 9(1):28–31, Dec 2014. ISSN 1862-6254. doi: 10.1002/pssr.201409520. URL http://dx.doi.org/10.1002/pssr.201409520.

[93] William Shockley and Hans J. Queisser. Detailed balance limit of efficiency of p-n junction solar cells. *Journal of Applied Physics*, 32(3):510, 1961. ISSN 0021-8979. doi: 10.1063/1.1736034. URL http://dx.doi.org/10.1063/1.1736034.

[94] Uwe Rau, Kurt Taretto, and Susanne Siebentritt. Grain boundaries in cu(in, ga)(se, s)2 thin-film solar cells. *Appl. Phys. A*, 96(1):221–234, dec

2008. doi: 10.1007/s00339-008-4978-0. URL http://dx.doi.org/10.1007/s00339-008-4978-0.

[95] C.-S Jiang, R. Noufi, K. Ramanathan, J. A. AbuShama, H. R. Moutinho, and M. M. Al-Jassim. Does the local built-in potential on grain boundaries of cu(in,ga)se[sub 2] thin films benefit photovoltaic performance of the device? *Appl. Phys. Lett.*, 85(13):2625, 2004. doi: 10.1063/1.1793346. URL http://dx.doi.org/10.1063/1.1793346.

[96] Jorgen H. Werner, Julian Mattheis, and Uwe Rau. Efficiency limitations of polycrystalline thin film solar cells: case of cu(in,ga)se2. *Thin Solid Films*, 480-481:399–409, Jun 2005. ISSN 0040-6090. doi: 10.1016/j.tsf.2004.11.052. URL http://dx.doi.org/10.1016/j.tsf.2004.11.052.

[97] Yanfa Yan, R. Noufi, and M. M. Al-Jassim. Grain-boundary physics in polycrystalline CuInSe 2 revisited: Experiment and theory. *Phys. Rev. Lett.*, 96(20), may 2006. doi: 10.1103/physrevlett.96.205501. URL http://dx.doi.org/10.1103/PhysRevLett.96.205501.

[98] C.-S. Jiang, R. Noufi, J. A. AbuShama, K. Ramanathan, H. R. Moutinho, J. Pankow, and M. M. Al-Jassim. Local built-in potential on grain boundary of cu(in,ga)se[sub 2] thin films. *Appl. Phys. Lett.*, 84(18):3477, 2004. doi: 10.1063/1.1737796. URL http://dx.doi.org/10.1063/1.1737796.

[99] M. J. Hetzer, Y. M. Strzhemechny, M. Gao, M. A. Contreras, A. Zunger, and L. J. Brillson. Direct observation of copper depletion and potential changes at copper indium gallium diselenide grain boundaries. *Appl. Phys. Lett.*, 86(16):162105, 2005. doi: 10.1063/1.1906331. URL http://dx.doi.org/10.1063/1.1906331.

[100] Clas Persson and Alex Zunger. Anomalous grain boundary physics in polycrystalline cuinse2 : The existence of a hole barrier. *Phys. Rev. Lett.*, 91(26), dec 2003. doi: 10.1103/physrevlett.91.266401. URL http://dx.doi.org/10.1103/PhysRevLett.91.266401.

[101] Susanne Siebentritt, Levent Gatay, David Regesch, Yasuhiro Aida, and Valrie Deprdurand. Why do we make cu(in,ga)se2 solar cells non-stoichiometric? *Solar Energy Materials and Solar Cells*, 119:18–25, Dec 2013. ISSN 0927-0248. doi: 10.1016/j.solmat.2013.04.014. URL http://dx.doi.org/10.1016/j.solmat.2013.04.014.

[102] M. Turcu, O. Pakma, and U. Rau. Interdependence of absorber composition and recombination mechanism in cu(in,ga)(se,s)[sub 2] heterojunction solar cells. *Applied Physics Letters*, 80(14):2598, 2002. ISSN 0003-6951. doi: 10.1063/1.1467621. URL http://dx.doi.org/10.1063/1.1467621.

[103] U. Rau, M. Schmidt, A. Jasenek, G. Hanna, and H.W. Schock. Electrical characterization of cu(in,ga)se2 thin-film solar cells and the role of defects for the device performance. *Solar Energy Materials and Solar Cells*, 67(1-4):137–143, Mar 2001. ISSN 0927-0248. doi: 10.1016/s0927-0248(00)00273-7. URL http://dx.doi.org/10.1016/S0927-0248(00)00273-7.

[104] D. Schmid, M. Ruckh, F. Grunwald, and H. W. Schock. Chalcopyrite/defect chalcopyrite heterojunctions on the basis of cuinse2. *Journal of Applied Physics*, 73(6):2902, 1993. ISSN 0021-8979. doi: 10.1063/1.353020. URL http://dx.doi.org/10.1063/1.353020.

[105] H. Z. Xiao, L.-Chung Yang, and A. Rockett. Structural, optical, and electrical properties of epitaxial chalcopyrite cuin3se5 films. *Journal of Applied Physics*, 76(3):1503, 1994. ISSN 0021-8979. doi: 10.1063/1.357725. URL http://dx.doi.org/10.1063/1.357725.

[106] A. J. Nelson, G. S. Horner, K. Sinha, and M. H. Bode. Ordered vacancy compound cuin3se5 on GaAs (100): Epitaxial growth and characterization. *Applied Physics Letters*, 64(26):3600, 1994. ISSN 0003-6951. doi: 10.1063/1.111211. URL http://dx.doi.org/10.1063/1.111211.

[107] C. Rincon, S. M. Wasim, G. Marin, R. Marquez, L. Nieves, G. Sanchez Perez, and E. Medina. Temperature dependence of the optical energy gap and urbach's energy of cuin[5]se[8]. *Journal of Applied Physics*, 90(9):4423, 2001. ISSN 0021-8979. doi: 10.1063/1.1405144. URL http://dx.doi.org/10.1063/1.1405144.

[108] Ariswan, G El haj Moussa, M Abdelali, F Guastavino, and C Llinares. Structural, optical and electrical properties of the ordered vacancy compound cuin3se5 thin films fabricated by flash evaporation. *Solid State Communications*, 124(10-11):391–396, Dec 2002. ISSN 0038-1098. doi: 10.1016/s0038-1098(02)00603-8. URL http://dx.doi.org/10.1016/S0038-1098(02)00603-8.

[109] Rachel Reena Philip and B Pradeep. Structural analysis and optical and electrical characterization of the ordered defect compound cuin5se8.

Semicond. Sci. Technol., 18(8):768–773, Jul 2003. ISSN 1361-6641. doi: 10.1088/0268-1242/18/8/309. URL `http://dx.doi.org/10.1088/0268-1242/18/8/309`.

[110] Fangdan Jiang and Jiayou Feng. First principles calculation on polytypes of ordered defect compound cuin[sub 5]se[sub 8]. *Applied Physics Letters*, 89(22):221920, 2006. ISSN 0003-6951. doi: 10.1063/1.2399941. URL `http://dx.doi.org/10.1063/1.2399941`.

[111] M. Morkel, L. Weinhardt, B. Lohmller, C. Heske, E. Umbach, W. Riedl, S. Zweigart, and F. Karg. Flat conduction-band alignment at the cds/cuinse[sub 2] thin-film solar-cell heterojunction. *Applied Physics Letters*, 79(27):4482, 2001. ISSN 0003-6951. doi: 10.1063/1.1428408. URL `http://dx.doi.org/10.1063/1.1428408`.

[112] T. Schulmeyer, R. Hunger, A. Klein, W. Jaegermann, and S. Niki. Photoemission study and band alignment of the cuinse[2](001)/cds heterojunction. *Applied Physics Letters*, 84(16):3067, 2004. ISSN 0003-6951. doi: 10.1063/1.1712034. URL `http://dx.doi.org/10.1063/1.1712034`.

[113] H. Monig, Ch.-H. Fischer, R. Caballero, C.A. Kaufmann, N. Allsop, M. Gorgoi, R. Klenk, H.-W. Schock, S. Lehmann, and M.C. Lux-Steiner. Surface cu depletion of cu(in,ga)se2 films: An investigation by hard x-ray photoelectron spectroscopy. *Acta Materialia*, 57(12):3645–3651, Jul 2009. ISSN 1359-6454. doi: 10.1016/j.actamat.2009.04.029. URL `http://dx.doi.org/10.1016/j.actamat.2009.04.029`.

[114] H. Monig, Ch.-H. Fischer, A. Grimm, B. Johnson, C. A. Kaufmann, R. Caballero, I. Lauermann, and M. Ch. Lux-Steiner. Surface cu-depletion of cu(in,ga)se[sub 2] thin films: Further experimental evidence for a defect-induced surface reconstruction. *Journal of Applied Physics*, 107(11):113540, 2010. ISSN 0021-8979. doi: 10.1063/1.3427539. URL `http://dx.doi.org/10.1063/1.3427539`.

[115] Dongxiang Liao and Angus Rockett. Cu depletion at the cuinse[2] surface. *Applied Physics Letters*, 82(17):2829, 2003. ISSN 0003-6951. doi: 10.1063/1.1570516. URL `http://dx.doi.org/10.1063/1.1570516`.

[116] Dongxiang Liao and Angus Rockett. Electronic and chemical phenomena at cu(in, ga)se2/cds heterojunctions and their implications for photovoltaic devices. In *Matarials Research Society Symposium Proceedings 763 (2003) 243248.*, volume 763, 2003.

[117] Pyuck-Pa Choi, Oana Cojocaru-Miredin, and Roland Wuerz. Compositional gradients and impurity distributions in cuinse 2 thin-film solar cells studied by atom probe tomography. *Surf. Interface Anal.*, 44(11-12):1386–1388, Apr 2012. ISSN 0142-2421. doi: 10.1002/sia.4948. URL `http://dx.doi.org/10.1002/sia.4948`.

[118] O. Cojocaru-Miredin, P. Choi, R. Wuerz, and D. Raabe. Exploring the p-n junction region in cu(in,ga)se2 thin-film solar cells at the nanometer-scale. *Applied Physics Letters*, 101(18):181603, 2012. ISSN 0003-6951. doi: 10.1063/1.4764527. URL `http://dx.doi.org/10.1063/1.4764527`.

[119] M. Souilah, X. Rocquefelte, A. Lafond, C. Guillot-Deudon, J.-P. Morniroli, and J. Kessler. Crystal structure re-investigation in wide band gap cigse compounds. *Thin Solid Films*, 517(7):2145–2148, Feb 2009. ISSN 0040-6090. doi: 10.1016/j.tsf.2008.10.077. URL `http://dx.doi.org/10.1016/j.tsf.2008.10.077`.

[120] J.M Merino, S Mahanty, M Len, R Diaz, F Rueda, and J.L Martin de Vidales. Structural characterization of cuin2se3.5, cuin3se5 and cuin5se8 compounds. *Thin Solid Films*, 361-362:70–73, Feb 2000. ISSN 0040-6090. doi: 10.1016/s0040-6090(99)00771-3. URL `http://dx.doi.org/10.1016/S0040-6090(99)00771-3`.

[121] I. V. Bodnar, A. A. Vaipolin, V. Yu. Rud, and Yu. V. Rud. Crystal structure of cuin3se5 and cuin5se8 ternary compounds. *Tech. Phys. Lett.*, 32(12):1003–1005, Dec 2006. ISSN 1090-6533. doi: 10.1134/s1063785006120029. URL `http://dx.doi.org/10.1134/S1063785006120029`.

[122] S. Lehmann, D. Fuertes Marron, M. Leon, R. Feyerherm, E. Dudzik, E. J. Friedrich, M. Tovar, Y. Tomm, C. Wolf, S. Schorr, and et al. Long-range structure of cu(in[sub x]ga[1-x])[3]se[5]: A complementary neutron and anomalous x-ray diffraction study. *Journal of Applied Physics*, 109 (1):013518, 2011. ISSN 0021-8979. doi: 10.1063/1.3524183. URL `http://dx.doi.org/10.1063/1.3524183`.

[123] M. Souilah, A. Lafond, N. Barreau, C. Guillot-Deudon, and J. Kessler. Evidence for a modified-stannite crystal structure in wide band gap cu-poor cuin[1-x]ga[x]se[2]: Impact on the optical properties. *Applied Physics Letters*, 92(24):241923, 2008. ISSN 0003-6951. doi: 10.1063/1.2944254. URL `http://dx.doi.org/10.1063/1.2944254`.

[124] D.S. Su, W. Neumann, and M. Giersig. Structure modifications in chalcopyrite semiconductors. *Thin Solid Films*, 361-362:218–222, Feb 2000. ISSN 0040-6090. doi: 10.1016/s0040-6090(99)00837-8. URL http://dx.doi.org/10.1016/S0040-6090(99)00837-8.

[125] L. Duran, C. Guerrero, E. Hernandez, J.M. Delgado, J. Contreras, S.M. Wasim, and C.A. Durante Rincan. Structural, optical and electrical properties of cuin5se8 and cuga5se8. *Journal of Physics and Chemistry of Solids*, 64(9-10):1907–1910, Sep 2003. ISSN 0022-3697. doi: 10.1016/s0022-3697(03)00069-6. URL http://dx.doi.org/10.1016/S0022-3697(03)00069-6.

[126] X. Fontane, V. Izquierdo-Roca, L. Calvo-Barrio, J. Alvarez-Garcia, A. Perez-Rodreguez, J. R. Morante, and W. Witte. In-depth resolved raman scattering analysis of secondary phases in cu-poor cuinse[sub 2] based thin films. *Applied Physics Letters*, 95(12):121907, 2009. ISSN 0003-6951. doi: 10.1063/1.3236770. URL http://dx.doi.org/10.1063/1.3236770.

[127] S. B. Zhang, Su-Huai Wei, Alex Zunger, and H. Katayama-Yoshida. Defect physics of the cuinse 2 chalcopyrite semiconductor. *Physical Review B*, 57(16):9642–9656, Apr 1998. ISSN 1095-3795. doi: 10.1103/physrevb.57.9642. URL http://dx.doi.org/10.1103/PhysRevB.57.9642.

[128] S. B. Zhang, Su-Huai Wei, and Alex Zunger. Stabilization of ternary compounds via ordered arrays of defect pairs. *Phys. Rev. Lett.*, 78:4059–4062, May 1997. doi: 10.1103/PhysRevLett.78.4059. URL http://link.aps.org/doi/10.1103/PhysRevLett.78.4059.

[129] Yanfa Yan, R. Noufi, K. M. Jones, K. Ramanathan, M. M. Al-Jassim, and B. J. Stanbery. Chemical fluctuation-induced nanodomains in cu(in,ga)se[sub 2] films. *Appl. Phys. Lett.*, 87(12):121904, 2005. doi: 10.1063/1.2053349. URL http://dx.doi.org/10.1063/1.2053349.

[130] U Rau, A Jasenek, H.W Schock, F Engelhardt, and Th Meyer. Electronic loss mechanisms in chalcopyrite based heterojunction solar cells. *Thin Solid Films*, 361-362:298–302, Feb 2000. ISSN 0040-6090. doi: 10.1016/s0040-6090(99)00762-2. URL http://dx.doi.org/10.1016/S0040-6090(99)00762-2.

[131] V. Nadenau, U. Rau, A. Jasenek, and H. W. Schock. Electronic properties of cugase[2]-based heterojunction solar cells. part i. transport analysis. *Journal of Applied Physics*, 87(1):584, 2000. ISSN 0021-8979. doi: 10.1063/1.371903. URL http://dx.doi.org/10.1063/1.371903.

[132] J.M. Zuo and J.C. Mabon. Web-based electron microscopy application software: Web-emaps url:, 2004. URL http://emaps.mrl.uiuc.edu/.

[133] Obadiah G. Reid, Keiko Munechika, and David S. Ginger. Space charge limited current measurements on conjugated polymer films using conductive atomic force microscopy. *Nano Lett.*, 8(6):1602–1609, Jun 2008. ISSN 1530-6992. doi: 10.1021/nl080155l. URL http://dx.doi.org/10.1021/nl080155l.

[134] Youngkyoo Kim, Steffan Cook, Sachetan M. Tuladhar, Stelios A. Choulis, Jenny Nelson, James R. Durrant, Donal D. C. Bradley, Mark Giles, Iain McCulloch, Chang-Sik Ha, and et al. A strong regioregularity effect in self-organizing conjugated polymer films and high-efficiency polythiophene:fullerene solar cells. *Nature Materials*, 5(3): 197–203, Feb 2006. ISSN 1476-4660. doi: 10.1038/nmat1574. URL http://dx.doi.org/10.1038/nmat1574.

[135] S. A. Choulis, Y. Kim, J. Nelson, D. D. C. Bradley, M. Giles, M. Shkunov, and I. McCulloch. High ambipolar and balanced carrier mobility in regioregular poly(3-hexylthiophene). *Appl. Phys. Lett.*, 85(17):3890, 2004. ISSN 0003-6951. doi: 10.1063/1.1805175. URL http://dx.doi.org/10.1063/1.1805175.

[136] Attila J. Mozer, Niyazi Serdar Sariciftci, Almantas Pivrikas, Ronald Osterbacka, Gytis Juska, Lutz Brassat, and Heinz Bassler. Charge carrier mobility in regioregular poly(3-hexylthiophene) probed by transient conductivity techniques: A comparative study. *Phys. Rev. B*, 71(3), Jan 2005. ISSN 1550-235X. doi: 10.1103/physrevb.71.035214. URL http://dx.doi.org/10.1103/PhysRevB.71.035214.

[137] M. C. J. M. Vissenberg. Theory of the field-effect mobility in amorphous organic transistors. *Phys. Rev. B*, 57(20):12964–12967, May 1998. ISSN 1095-3795. doi: 10.1103/physrevb.57.12964. URL http://dx.doi.org/10.1103/PhysRevB.57.12964.

[138] Amy M. Ballantyne, Lichun Chen, Justin Dane, Thomas Hammant, Felix M. Braun, Martin Heeney, Warren Duffy, Iain McCulloch, Donal D. C. Bradley, and Jenny Nelson. The effect of poly(3-hexylthiophene) molecular weight on charge transport and the performance of polymer:fullerene solar cells. *Adv. Funct. Mater.*, 18(16):2373–2380, Aug 2008. ISSN 1616-3028. doi: 10.1002/adfm.200800145. URL http://dx.doi.org/10.1002/adfm.200800145.

[139] S. M. Tuladhar, D. Poplavskyy, S. A. Choulis, J. R. Durrant, D. D. C. Bradley, and J. Nelson. Ambipolar charge transport in films of methanofullerene and poly(phenylenevinylene)/methanofullerene blends. *Adv. Funct. Mater.*, 15(7):1171–1182, Jul 2005. ISSN 1616-3028. doi: 10.1002/adfm.200400337. URL `http://dx.doi.org/10.1002/adfm.200400337`.

[140] A. Pivrikas, G. Juska, A. Mozer, M. Scharber, K. Arlauskas, N. Sariciftci, H. Stubb, and R. Osterbacka. Bimolecular recombination coefficient as a sensitive testing parameter for low-mobility solar-cell materials. *Physical Review Letters*, 94(17), May 2005. ISSN 1079-7114. doi: 10.1103/physrevlett.94.176806. URL `http://dx.doi.org/10.1103/PhysRevLett.94.176806`.

[141] G. Juska, K. Arlauskas, M. Viliunas, and J. Kocka. Extraction current transients: New method of study of charge transport in microcrystalline silicon. *Physical Review Letters*, 84(21):4946–4949, May 2000. ISSN 1079-7114. doi: 10.1103/physrevlett.84.4946. URL `http://dx.doi.org/10.1103/PhysRevLett.84.4946`.

[142] G. Juska, N. Nekrasasa, K. Geneviciusa, J. Stuchlikb, and J. Kocka. Relaxation of photoexited charge carrier concentration and mobility in micro c-si:h. *Thin Solid Films*, 451-452:290–293, Mar 2004. ISSN 0040-6090. doi: 10.1016/j.tsf.2003.11.053. URL `http://dx.doi.org/10.1016/j.tsf.2003.11.053`.

[143] A. J. Mozer, N. S. Sariciftci, L. Lutsen, D. Vanderzande, R. Osterbacka, M. Westerling, and G. Juska. Charge transport and recombination in bulk heterojunction solar cells studied by the photoinduced charge extraction in linearly increasing voltage technique. *Appl. Phys. Lett.*, 86(11):112104, 2005. ISSN 0003-6951. doi: 10.1063/1.1882753. URL `http://dx.doi.org/10.1063/1.1882753`.

[144] A. Pivrikas, N. S. Sariciftci, G. Juska, and R. Osterbacka. A review of charge transport and recombination in polymer/fullerene organic solar cells. *Prog. Photovolt: Res. Appl.*, 15(8):677–696, 2007. ISSN 1099-159X. doi: 10.1002/pip.791. URL `http://dx.doi.org/10.1002/pip.791`.

[145] G. Dennler, A.J. Mozer, G. Juska, A. Pivrikas, R. Osterbacka, A. Fuchsbauer, and N.S. Sariciftci. Charge carrier mobility and lifetime versus composition of conjugated polymer/fullerene bulk-heterojunction solar cells. *Organic Electronics*, 7(4):229–234, Aug 2006. ISSN 1566-1199.

doi: 10.1016/j.orgel.2006.02.004. URL http://dx.doi.org/10.1016/j.orgel.2006.02.004.

[146] G. Juska, K. Genevicius, N. Nekrasas, G. Sliauzys, and G. Dennler. Trimolecular recombination in polythiophene: fullerene bulk heterojunction solar cells. *Appl. Phys. Lett.*, 93(14):143303, 2008. ISSN 0003-6951. doi: 10.1063/1.2996588. URL http://dx.doi.org/10.1063/1.2996588.

[147] G. Juska, K. Arlauskas, M. Viliunas, K. Genevicius, R. Osterbacka, and H. Stubb. Charge transport in pi-conjugated polymers from extraction current transients. *Phys. Rev. B*, 62(24):R16235–R16238, Dec 2000. ISSN 1095-3795. doi: 10.1103/physrevb.62.r16235. URL http://dx.doi.org/10.1103/PhysRevB.62.R16235.

[148] J. Kocka, A. Fejfar, H. Stuchlikova, J. Stuchlik, P. Fojtik, T. Mates, B. Rezek, K. Luterova, V. Svrcek, and I. Pelant. Basic features of transport in microcrystalline silicon. *Solar Energy Materials and Solar Cells*, 78(1-4):493–512, Jul 2003. ISSN 0927-0248. doi: 10.1016/s0927-0248(02)00449-x. URL http://dx.doi.org/10.1016/S0927-0248(02)00449-X.

[149] G. Juska, M. Viliunas, K. Arlauskas, N. Nekrasas, N. Wyrsch, and L. Feitknecht. Hole drift mobility in c-si:h. *Journal of Applied Physics*, 89(9):4971, 2001. ISSN 0021-8979. doi: 10.1063/1.1359436. URL http://dx.doi.org/10.1063/1.1359436.

[150] J. A. Carr and S. Chaudhary. On accurate capacitance characterization of organic photovoltaic cells. *Appl. Phys. Lett.*, 100(21):213902, 2012. ISSN 0003-6951. doi: 10.1063/1.4720403. URL http://dx.doi.org/10.1063/1.4720403.

[151] Sebastian Bange, Marcel Schubert, and Dieter Neher. Charge mobility determination by current extraction under linear increasing voltages: Case of nonequilibrium charges and field-dependent mobilities. *Phys. Rev. B*, 81(3), Jan 2010. ISSN 1550-235X. doi: 10.1103/physrevb.81.035209. URL http://dx.doi.org/10.1103/PhysRevB.81.035209.

[152] Christopher G. Shuttle, Richard Hamilton, Jenny Nelson, Brian C. O' Regan, and James R. Durrant. Measurement of charge-density dependence of carrier mobility in an organic semiconductor blend. *Adv. Funct. Mater.*, 20(5):698–702, Mar 2010. ISSN 1616-3028. doi: 10.1002/adfm.200901734. URL http://dx.doi.org/10.1002/adfm.200901734.

[153] C. Shuttle, B. O'Regan, A. Ballantyne, J. Nelson, D. Bradley, and J. Durrant. Bimolecular recombination losses in polythiophene: Fullerene solar cells. *Phys. Rev. B*, 78(11), Sep 2008. ISSN 1550-235X. doi: 10.1103/physrevb.78.113201. URL `http://dx.doi.org/10.1103/PhysRevB.78.113201`.

[154] M. Stephen, S. Karuthedath, T. Sauermann, K. Genevicius, and G. Juska. Degradation effects on charge carrier transport in p3ht:pcbm solar cells studied by photo-celiv and tof. *Organic Photovoltaics XV*, Oct 2014. doi: 10.1117/12.2061857. URL `http://dx.doi.org/10.1117/12.2061857`.

[155] H. Hintz, H. Peisert, H.-J. Egelhaaf, and T. Chasse. Reversible and irreversible light-induced p-doping of p3ht by oxygen studied by photoelectron spectroscopy (xps/UPS). *The Journal of Physical Chemistry C*, 115 (27):13373–13376, Jul 2011. ISSN 1932-7455. doi: 10.1021/jp2032737. URL `http://dx.doi.org/10.1021/jp2032737`.

[156] Russell M Geisthardt and James R Sites. Nonuniformity characterization of cdte solar cells using lbic. *Photovoltaics, IEEE Journal of*, 4(4):1114–1118, 2014.

[157] Michael G Deceglie, Hal S Emmer, Zachary C Holman, Antoine Descoeudres, Stefaan De Wolf, Christophe Ballif, Harry Atwater, et al. Scanning laser-beam-induced current measurements of lateral transport near-junction defects in silicon heterojunction solar cells. *Photovoltaics, IEEE Journal of*, 4(1):154–159, 2014.

[158] FJ Navas, R Alcántara, C Fernández-Lorenzo, and J Martín-Calleja. High resolution laser beam induced current images under trichromatic laser radiation: Approximation to the solar irradiation. *Review of Scientific Instruments*, 81(3):035108, 2010.

[159] Paul Basore et al. Extended spectral analysis of internal quantum efficiency. In *Photovoltaic Specialists Conference, 1993., Conference Record of the Twenty Third IEEE*, pages 147–152. IEEE, 1993.

[160] Martin A Green. Self-consistent optical parameters of intrinsic silicon at 300k including temperature coefficients. *Solar Energy Materials and Solar Cells*, 92(11):1305–1310, 2008.

[161] Martin A Green, Keith Emery, Yoshihiro Hishikawa, Wilhelm Warta, and Ewan D Dunlop. Solar cell efficiency tables (version 45). *Progress in photovoltaics: research and applications*, 23(1):1–9, 2015.

[162] CH Huang, Sheng S Li, L Rieth, A Halani, ML Fisher, Jiyon Song, TJ Anderson, and PH Holloway. A comparative study of chemical-bath-deposited cds,(cd, zn) s, zns, and in (oh) x s y buffer layer for cigs-based solar cells. In *Photovoltaic Specialists Conference, 2000. Conference Record of the Twenty-Eighth IEEE*, pages 696–699. IEEE, 2000.

[163] T Nakada, M Mizutani, Y Hagiwara, and A Kunioka. High-efficiency cu (in, ga) se 2 thin-film solar cells with a cbd-zns buffer layer. *Solar energy materials and solar cells*, 67(1):255–260, 2001.

[164] RN Bhattacharya, MA Contreras, B Egaas, RN Noufi, A Kanevce, and JR Sites. High efficiency thin-film cuin1-xgaxse2 photovoltaic cells using a cd1-xznxs buffer layer. *Applied Physics Letters*, 89(25):3503, 2006.

[165] CD Lokhande, HM Pathan, M Giersig, and H Tributsch. Preparation of zn x (o, s) y thin films using modified chemical bath deposition method. *Applied surface science*, 187(1):101–107, 2002.

[166] MA Contreras, T Nakada, M Hongo, AO Pudov, and JR Sites. Zno/zns (o, oh)/cu (in, ga) se/sub 2//mo solar cell with 18.6% efficiency. In *Photovoltaic Energy Conversion, 2003. Proceedings of 3rd World Conference on*, volume 1, pages 570–573. IEEE, 2003.

[167] Ahmed Ennaoui. Chemical bath process for highly efficient cd-free chalcopyrite thin-film-based solar cells. *Canadian Journal of Physics*, 77(9): 723–729, 2000.

[168] AH Castro Neto, F Guinea, NMR Peres, Kostya S Novoselov, and Andre K Geim. The electronic properties of graphene. *Reviews of modern physics*, 81(1):109, 2009.

[169] Matthew J Allen, Vincent C Tung, and Richard B Kaner. Honeycomb carbon: a review of graphene. *Chemical reviews*, 110(1):132–145, 2009.

[170] S Tongay, M Lemaitre, X Miao, B Gila, BR Appleton, and AF Hebard. Rectification at graphene-semiconductor interfaces: zero-gap semiconductor-based diodes. *Physical Review X*, 2(1):011002, 2012.

[171] Kirill I Bolotin, KJ Sikes, Zd Jiang, M Klima, G Fudenberg, J Hone, Ph Kim, and HL Stormer. Ultrahigh electron mobility in suspended graphene. *Solid State Communications*, 146(9):351–355, 2008.

[172] Minhyeok Choe, Byoung Hoon Lee, Gunho Jo, June Park, Woojin Park, Sangchul Lee, Woong-Ki Hong, Maeng-Je Seong, Yung Ho Kahng,

Kwanghee Lee, et al. Efficient bulk-heterojunction photovoltaic cells with transparent multi-layer graphene electrodes. *Organic Electronics*, 11(11):1864–1869, 2010.

[173] Ling Yin, Kang Zhang, Hailin Luo, Guanming Cheng, Xuhang Ma, Zhiyu Xiong, and Xudong Xiao. Highly efficient graphene-based cu (in, ga) se 2 solar cells with large active area. *Nanoscale*, 6(18):10879–10886, 2014.

[174] Heejun Yang, Jinseong Heo, Seongjun Park, Hyun Jae Song, David H Seo, Kyung-Eun Byun, Philip Kim, InKyeong Yoo, Hyun-Jong Chung, and Kinam Kim. Graphene barristor, a triode device with a gate-controlled schottky barrier. *Science*, 336(6085):1140–1143, 2012.

[175] Xiaochang Miao, Sefaattin Tongay, Maureen K Petterson, Kara Berke, Andrew G Rinzler, Bill R Appleton, and Arthur F Hebard. High efficiency graphene solar cells by chemical doping. *Nano letters*, 12(6): 2745–2750, 2012.

[176] Xinming Li, Hongwei Zhu, Kunlin Wang, Anyuan Cao, Jinquan Wei, Chunyan Li, Yi Jia, Zhen Li, Xiao Li, and Dehai Wu. Graphene-on-silicon schottky junction solar cells. *Advanced Materials*, 22(25):2743–2748, 2010.

[177] Xiaochen Dong, Dongliang Fu, Wenjing Fang, Yumeng Shi, Peng Chen, and Lain-Jong Li. Doping single-layer graphene with aromatic molecules. *Small*, 5(12):1422–1426, 2009.

[178] B Uchoa, C-Y Lin, and AH Castro Neto. Tailoring graphene with metals on top. *Physical Review B*, 77(3):035420, 2008.

[179] Haibo Wang, Thandavarayan Maiyalagan, and Xin Wang. Review on recent progress in nitrogen-doped graphene: synthesis, characterization, and its potential applications. *Acs Catalysis*, 2(5):781–794, 2012.

[180] Su-Huai Wei, SB Zhang, and Alex Zunger. Effects of na on the electrical and structural properties of cuinse˜ 2. *Journal of Applied Physics*, 85 (10):7214–7218, 1999.

[181] Xiaojie Liu, CZ Wang, YX Yao, WC Lu, M Hupalo, MC Tringides, and KM Ho. Bonding and charge transfer by metal adatom adsorption on graphene. *Physical Review B*, 83(23):235411, 2011.

[182] Leif I Johansson, Chao Xia, Chariya Virojanadara, et al. Na induced changes in the electronic band structure of graphene grown on c-face sic. *Graphene*, 2(01):1, 2013.

[183] Xuesong Li, Yanwu Zhu, Weiwei Cai, Mark Borysiak, Boyang Han, David Chen, Richard D Piner, Luigi Colombo, and Rodney S Ruoff. Transfer of large-area graphene films for high-performance transparent conductive electrodes. *Nano letters*, 9(12):4359–4363, 2009.

[184] Seunghyun Lee, Kyunghoon Lee, Chang-Hua Liu, and Zhaohui Zhong. Homogeneous bilayer graphene film based flexible transparent conductor. *Nanoscale*, 4(2):639–644, 2012.

[185] Dhiraj Sinha and Ji Ung Lee. Ideal graphene/silicon schottky junction diodes. *Nano letters*, 14(8):4660–4664, 2014.

[186] Susanne Siebentritt and Uwe Rau. *Wide-gap chalcopyrites*, volume 1. Springer, 2006.

[187] Young-Jun Yu, Yue Zhao, Sunmin Ryu, Louis E Brus, Kwang S Kim, and Philip Kim. Tuning the graphene work function by electric field effect. *Nano letters*, 9(10):3430–3434, 2009.

[188] Yoyo Hinuma, Fumiyasu Oba, Yu Kumagai, and Isao Tanaka. Ionization potentials of (112) and (11 2^{-}) facet surfaces of cuinse 2 and cugase 2. *Physical Review B*, 86(24):245433, 2012.

[189] C Heske, R Fink, E Umbach, W Riedl, and F Karg. Na-induced effects on the electronic structure and composition of cu (in, ga) se2 thin-film surfaces. *Applied physics letters*, 68(24):3431–3433, 1996.

[190] S Chattopadhyay, YF Huang, Yi-Jun Jen, A Ganguly, KH Chen, and LC Chen. Anti-reflecting and photonic nanostructures. *Materials Science and Engineering: R: Reports*, 69(1):1–35, 2010.

[191] Kyoo-Chul Park, Hyungryul J Choi, Chih-Hao Chang, Robert E Cohen, Gareth H McKinley, and George Barbastathis. Nanotextured silica surfaces with robust superhydrophobicity and omnidirectional broadband supertransmissivity. *ACS nano*, 6(5):3789–3799, 2012.

[192] A Gombert, W Glaubitt, K Rose, J Dreibholz, B Bläsi, A Heinzel, D Sporn, W Döll, and V Wittwer. Subwavelength-structured antireflective surfaces on glass. *Thin Solid Films*, 351(1):73–78, 1999.

[193] Jeri'Ann Hiller, Jonas D Mendelsohn, and Michael F Rubner. Reversibly erasable nanoporous anti-reflection coatings from polyelectrolyte multilayers. *Nature materials*, 1(1):59–63, 2002.

[194] Stefan Walheim, Erik Schäffer, Jürgen Mlynek, and Ullrich Steiner. Nanophase-separated polymer films as high-performance antireflection coatings. *Science*, 283(5401):520–522, 1999.

[195] J-Q Xi, Martin F Schubert, Jong Kyu Kim, E Fred Schubert, Minfeng Chen, Shawn-Yu Lin, Wayne Liu, and Joe A Smart. Optical thin-film materials with low refractive index for broadband elimination of fresnel reflection. *Nature photonics*, 1(3):176–179, 2007.

[196] Bulent E Yoldas and Deborah P Partlow. Wide spectrum antireflective coating for fused silica and other glasses. *Applied optics*, 23(9):1418–1424, 1984.

[197] Xin-Tong Zhang, Osamu Sato, Minori Taguchi, Yasuaki Einaga, Taketoshi Murakami, and Akira Fujishima. Self-cleaning particle coating with antireflection properties. *Chemistry of Materials*, 17(3):696–700, 2005.

[198] Rahul Dewan, Stefan Fischer, V Benno Meyer-Rochow, Yasemin Özdemir, Saeed Hamraz, and Dietmar Knipp. Studying nanostructured nipple arrays of moth eye facets helps to design better thin film solar cells. *Bioinspiration & biomimetics*, 7(1):016003, 2011.

[199] Peichen Yu, Meng-Yih Chiu, Chia-Hua Chang, Chung-Yu Hong, Yu-Lin Tsai, Hau-Vei Han, and Yu-Rue Wu. Towards high-efficiency multi-junction solar cells with biologically inspired nanosurfaces. *Progress in Photovoltaics: Research and Applications*, 22(3):300–307, 2014.

[200] Svetoslav Koynov, Martin S Brandt, and Martin Stutzmann. Black nonreflecting silicon surfaces for solar cells. *Applied Physics Letters*, 88 (20):203107, 2006.

[201] Howard M Branz, Vernon E Yost, Scott Ward, Kim M Jones, Bobby To, and Paul Stradins. Nanostructured black silicon and the optical reflectance of graded-density surfaces. *Applied Physics Letters*, 94(23): 231121, 2009.

[202] Patrick Campbell and Martin A Green. Light trapping properties of pyramidally textured surfaces. *Journal of Applied Physics*, 62(1):243–249, 1987.

[203] Erik Garnett and Peidong Yang. Light trapping in silicon nanowire solar cells. *Nano letters*, 10(3):1082–1087, 2010.

[204] Yi-Fan Huang, Surojit Chattopadhyay, Yi-Jun Jen, Cheng-Yu Peng, Tze-An Liu, Yu-Kuei Hsu, Ci-Ling Pan, Hung-Chun Lo, Chih-Hsun Hsu, Yuan-Huei Chang, et al. Improved broadband and quasi-omnidirectional anti-reflection properties with biomimetic silicon nanostructures. *Nature nanotechnology*, 2(12):770–774, 2007.

[205] Otto L Muskens, Jaime Gómez Rivas, Rienk E Algra, Erik PAM Bakkers, and Ad Lagendijk. Design of light scattering in nanowire materials for photovoltaic applications. *Nano letters*, 8(9):2638–2642, 2008.

[206] Jihun Oh, Hao-Chih Yuan, and Howard M Branz. An 18.2%-efficient black-silicon solar cell achieved through control of carrier recombination in nanostructures. *Nature nanotechnology*, 7(11):743–748, 2012.

[207] Hitoshi Sai, Yoshiaki Kanamori, Koji Arafune, Yoshio Ohshita, and Masafumi Yamaguchi. Light trapping effect of submicron surface textures in crystalline si solar cells. *Progress in Photovoltaics: Research and Applications*, 15(5):415–423, 2007.

[208] Ken Xingze Wang, Zongfu Yu, Victor Liu, Yi Cui, and Shanhui Fan. Absorption enhancement in ultrathin crystalline silicon solar cells with antireflection and light-trapping nanocone gratings. *Nano letters*, 12(3):1616–1619, 2012.

[209] Wei Wang, Shaomin Wu, Kitt Reinhardt, Yalin Lu, and Shaochen Chen. Broadband light absorption enhancement in thin-film silicon solar cells. *Nano letters*, 10(6):2012–2018, 2010.

[210] Jia Zhu, Ching-Mei Hsu, Zongfu Yu, Shanhui Fan, and Yi Cui. Nanodome solar cells with efficient light management and self-cleaning. *Nano letters*, 10(6):1979–1984, 2009.

[211] I Schnitzer, E Yablonovitch, C Caneau, TJ Gmitter, and Axel Scherer. 30% external quantum efficiency from surface textured, thin-film light-emitting diodes. *Applied Physics Letters*, 63(16):2174–2176, 1993.

[212] Jong Kyu Kim, Sameer Chhajed, Martin F Schubert, E Fred Schubert, Arthur J Fischer, Mary H Crawford, Jaehee Cho, Hyunsoo Kim, and Cheolsoo Sone. Light-extraction enhancement of gainn light-emitting diodes by graded-refractive-index indium tin oxide anti-reflection contact. *Advanced materials*, 20(4):801–804, 2008.

[213] EF Schubert, NEJ Hunt, M Micovic, RJ Malik, DL Sivco, AY Cho, and GJ Zydzik. Highly efficient light-emitting diodes with microcavities. *Science*, 265(5174):943–945, 1994.

[214] Hao-Chih Yuan, Vernon E Yost, Matthew R Page, Paul Stradins, Daniel L Meier, and Howard M Branz. Efficient black silicon solar cell with a density-graded nanoporous surface: Optical properties, performance limitations, and design rules. *Applied Physics Letters*, 95(12): 123501, 2009.

[215] SJ Wilson and MC Hutley. The optical properties of'moth eye'antireflection surfaces. *Journal of Modern Optics*, 29(7):993–1009, 1982.

[216] PB Clapham and MC Hutley. Reduction of lens reflexion by the moth eye principle. 1973.

[217] Andrew R Parker and Helen E Townley. Biomimetics of photonic nanostructures. *Nature nanotechnology*, 2(6):347–353, 2007.

[218] OO Awadelkarim, T Gu, RA Ditizio, PI Mikulan, SJ Fonash, JF Rembetski, and YD Chan. Creation of deep gap states in si during cl2 or hbr plasma etch exposures. *Journal of Vacuum Science & Technology A*, 11 (4):1332–1336, 1993.

[219] N Blayo, I Tepermeister, JL Benton, GS Higashi, T Boone, A Onuoha, FP Klemens, DE Ibbotson, JTC Lee, and HH Sawin. Comparison of advanced plasma sources for etching applications. iv. plasma induced damage in a helicon and a multipole electron cyclotron resonance source. *Journal of Vacuum Science & Technology B*, 12(3):1340–1350, 1994.

[220] YJ Lee, SW Hwang, GY Yeom, JW Lee, and JY Lee. Etch-induced damage in single crystal si trench etching by planar inductively coupled cl 2/n 2 and cl 2/hbr plasmas. *Thin solid films*, 341(1):168–171, 1999.

[221] C Wu, CH Crouch, L Zhao, JE Carey, R Younkin, JA Levinson, E Mazur, RM Farrell, P Gothoskar, and A Karger. Near-unity below-band-gap absorption by microstructured silicon. *Applied Physics Letters*, 78(13):1850–1852, 2001.

[222] I Montero, L Galan, E De La Cal, JM Albella, and JC Pivin. Incorporation of oh radicals in anodic silicon oxide films studied by secondary-ion mass spectroscopy, x-ray photoelectron spectroscopy and ir analysis. *Thin Solid Films*, 193:325–332, 1990.

[223] Yanfa Yan and Mowafak M Al-Jassim. Transmission electron microscopy of chalcogenide thin-film photovoltaic materials. *Current Opinion in Solid State and Materials Science*, 16(1):39–44, 2012.